eXPRESS Polymer Letters Vol.2, No.10 (2008) 687
Available online at www.expresspolymlett.com
DOI: 10.3144/expresspolymlett.2008.81

Editorial corner – a personal view

Are hierarchical composite structures the way forward to improve the properties of truly green composites?

A. Bismarck[*]

Department of Chemical Engineering, Polymer & Composite Engineering (PaCE) Group, Imperial College London, South Kensington Campus, London, SW7 2AZ, UK

Rising oil prices, exhaustion of landfill sites emphasise end-of-life problems associated with traditional materials and have triggered fresh interest in polymer and composite end-of-life and recycling issues. Consumer demands for more environment-friendly goods and intensifying legislative pressure for greener, carbon neutral technologies are forcing materials manufacturers to consider the environmental impact of their products. Consequently, the composite industry is seeking greener materials that match the physical performance of traditional ones. Renewable polymers often have inferior properties to their synthetic counterparts. Developing composites is thus a vital strategy for enhancing the performance of these polymers. In order to create a new generation of environmentally superior polymer composites, it is necessary to replace synthetic fillers with renewable ones.

Natural fibres are used for various applications. However, simple fibre reinforcement of renewable polymers has failed to achieve the performance of conventional composites. New green reinforcing agents, such as bacterial cellulose fibrils produced by various bacteria may provide a breakthrough. Bacterial cellulose fibrils have diameters ranging from 10 to 100 nm and a measured Young's modulus of 78 GPa, which is comparable to that of glass fibres but at a lower density. In addition to its lightweight and attractive mechanical properties, bacterial cellulose is non toxic, renewable and biodegradable. These intrinsic properties can be used to influence and enhance the matrix performance.

Nature demonstrates the use of hierarchical structures when high mechanical resistance is needed, e.g. in plant cell walls, animal shells and bones, through the assembly of molecules of different sizes. The application of this concept is markedly improving our engineering of *truly green* composites. Nanocellulose coated natural fibres were created by cultivating cellulose-producing bacteria in the presence of fibres, resulting in significant coverage of the fibre surfaces by bacterial cellulose. We have created hierarchical structures in natural fibre composites by using these 'hairy' fibres to deliver the nanoreinforcement into polymer matrices, avoiding troublesome processing issues associated with anisotropic nanofillers. There are some outstanding issues in hierarchically structuring composites: the compatibility between all phases, the arrangement of the nanofiller within the composite, and biodegradability control. The separation of end-of-life waste of *truly green* composites from the waste streams and compositing is another thorny issue.

Dr. Alexander Bismarck
Member of the International Advisory Board

---

[*] Corresponding author, e-mail: a.bismarck@imperial.ac.uk

eXPRESS Polymer Letters Vol.2, No.10 (2008) 688–694
Available online at www.expresspolymlett.com
DOI: 10.3144/expresspolymlett.2008.82

Field strength dependence of the high-frequency viscoelastic relaxation process in polyaniline/silicone oil electrorheological suspensions

P. Hiamtup[1], *A. Sirivat*[1*], *A. M. Jamieson*[2]

[1]The Petroleum and Petrochemical College, Chulalongkorn University, Bangkok 10330, Thailand
[2]Department of Macromolecular Science, Case Western Reserve University, Cleveland, Ohio 44106, USA

Received 15 July 2008; accepted in revised form 26 August 2008

Abstract. Polyaniline (PANI) was synthesized via oxidative coupling polymerization in acid conditions and de-doped in ammonia solution. The electrorheological (ER) properties of the PANI/silicone oil suspensions were investigated in the oscillatory mode shear, with particular focus on the high frequency region, where a crossover in $G'(\omega)$ and $G''(\omega)$ signals the onset of a dissipative relaxation process, presumed to be associated with motion of PANI particles within the fibrillar structures generated by the electric field. The relationship between the crossover frequency, ω_c, and the electric field strength (E) was investigated as a function of matrix viscosity and shear strain. We find that ω_c increases with increasing electric field strength, and decreases with increases of matrix viscosity and strain amplitude. These observations are in qualitative agreement with a theoretical model, which relates the relaxation mechanism to the competition between hydrodynamic and electrostatic forces between PANI particles within thick fibrillar structures. At the crossover point, a critical scaling relation is found relating two dimensionless parameters, the Mason number (Mn), and the Peclet number (Pe), viz. $Mn \sim (Pe)^{0.09}$.

***Keywords:** rheology, electrorheological fluid, polyaniline, secondary crossover*

1. Introduction

Electrorheological (ER) suspensions, first studied extensively by Winslow (1949), display dramatic changes in rheological properties upon application of an electric field [1]. A typical ER fluid is composed of micron-sized polarizable particles dispersed in a non-conducting medium. Under the action of the field, the particles form three dimensional fibrillar structures, which are aligned along the direction of the electric field and generate additional resistance against fluid motion [2]. With their adjustable viscosity, fast response, and reversible rheological behavior, ER fluids are regarded as smart materials, with potential for applications in active devices, which transform electric energy to mechanical energy [3]. Possible examples include clutches, breaks, shock absorbers, engine mounts, valves, flow pumps, and other variable control and servo devices [4].

A dimensionless parameter, the Mason number (Mn), has been widely used to describe the relative importance of hydrodynamic to electrostatic polarization forces, and has been shown to be useful to predict the ER suspension behavior in steady shear [5]. In the case of oscillatory shear, relatively few studies have explored the influence of the forces acting on the polarizable particles [1, 6]. Of particular interest here are molecular dynamics simulation studies [1, 7] which found a frequency scaling of the dynamic shear moduli analogous to the

---

[*]Corresponding author, e-mail: anuvat_s@chula.ac.th

Mason number scaling of the steady shear response. Experimental measurements have reported the frequency scaling of the shear moduli of ER fluids based on conducting polymers consistent with the theoretical prediction [8, 9]. In this paper, we focus on a prediction of molecular dynamics simulations that the oscillatory shear moduli of an ER fluid exhibit a high-frequency relaxation process traced to motion of the polarizable spheres within thick fibrillar clusters [1].

In previous studies, the use of polyaniline (PANI), and other semiconducting polymers, as the dispersed phase in an ER fluid has been extensively explored [8, 10–12], since such polymers typically have a high intrinsic polarizability, even in the absence of any activator. PANI in particular has several advantages over other polymer particles such as low density, ease of synthesis and conductivity control, and thermal and environmental stability [4, 13]. In the linear viscoelastic regime, a PANI suspension typically shows a liquid to solid transition at a critical electric field strength, whose value depends on particle concentration and host fluid viscosity [12]. Such behavior is consistent with the idea that there are two opposing forces which influence the assembly of the polarizable particles into fibrillar structures spanning the electrodes, viz. the electrostatic interparticle driving force for assembly, and the opposing hydrodynamic force associated with fluid motion [14].

In this study, we focus particularly on the fact that, at higher frequencies, the storage and loss shear moduli of PANI ER suspensions exhibit another crossover which signals the onset of a high-frequency relaxation mechanism presumed to be that predicted by molecular dynamics simulations [1]. We explore the effects of the medium viscosity, the shearing amplitude as well as the electric field strength on the crossover frequency, ω_c, in the linear and nonlinear viscoelastic regimes. Dimensionless parameters, the Mason number (*Mn*) and Peclet number (*Pe*), associated with the onset of the transition, are correlated according to a scaling relation.

2. Experimental

2.1. Materials

Aniline, C_6H_7N (AR grade, Merck, Germany) was vacuum-distilled and used as the monomer. Ammonium peroxydisulphate, $(NH_4)_2S_2O_8$ (AR grade, Merck, Germany) was used as the oxidant. 38% Hydrochloric acid, HCl (AR grade, Labscan, Thailand); 25% solution of ammonia, NH_4OH (AR grade, Merck, Germany) and methanol, CH_3OH (AR grade, Labscan, Germany) were used as received. The base fluids, silicone oil (AR grade, Dow Corning, USA) with density 0.96 g/cm^3 and kinematic viscosities of 10^{-4} m^2/s (100 cSt), $5\cdot10^{-4}$ m^2/s, and 10^{-3} m^2/s were vacuum-dried and stored in a desiccator prior to use.

2.2. Polymerization procedure

PANI was synthesized via the oxidative coupling polymerization according to the method of Cao *et al.* (1989) [15]. After the course of polymerization, the precipitate was then dedoped by immersion in 3% NH_4OH in order to adjust its conductivity, before being vacuum dried and passed through a 38 μm sieve shaker to control the particle size and its distribution.

To determine the electrical conductivity, PANI powder was pressed into disk pellets by a hydraulic press (diameter of 25 mm and ~0.2 mm thick). Electrical conductivity was measured using a custom-built four-point probe at 30°C. The measurements were performed in the linear Ohmic regime where the specific conductivity values are independent of the applied DC voltage.

2.3. Preparation of ER fluids

Prior to dispersion in silicone oil, PANI powder was dried for 2 days at room temperature to remove moisture in a vacuum oven at room temperature. The particles were then dispersed in the silicone oil with an ultrasonicator (Transonic 570/H, Elma, Singen, Germany) for 30 minutes at 25°C. The PANI suspensions were then prepared at a volume fraction of 0.05. The suspensions were stored in a dessiccator and redispersed by ultrasonication for a period of 10 minutes at 25°C before each experiment.

2.4. Rheological measurements

Dynamic rheological properties of the suspensions were investigated using a modified melt rheometer (ARES, Rheometric Scientific Inc., Piscataway, USA) with parallel plates (diameter of 50 mm) attached via insulating spacers to the transducer and motor, with the gap size fixed at 0.2 mm throughout the experiment to avoid sloshing of samples at high frequency. A DC electric field was applied across the gap between the plates by a function generator (GFG-8216A, Instek, Melrose, USA) and a high voltage amplifier (Model 609E-6, Trek, USA). The electric field was applied for 10 minutes to obtain an equilibrium fibrillar or columnar structure before each measurement was taken. The experiments were carried out in the frequency sweep mode with frequency (ω) ranging from 0.1 to 100 rad/s at a temperature of 27±1°C to investigate the effect of electric field strength on G' and G''. Of particular interest was to correlate the applied field strength, E, with the G'-G'' crossover frequency, ω_c, as a function of medium viscosity and shear strain.

3. Results and discussion

3.1. Electrorheological properties and G′-G″ crossover of PANI/silicone oil suspensions

The effect of the silicone oil viscosity and the strain amplitude, on the relationship between ω_c and E was investigated for PANI suspensions prepared at the volume fraction of 0.05 in silicone oils of three different viscosities; 100, 500, 1000 cSt; the systems are coded as PANI/100, PANI/500, and PANI/1000, respectively. The PANI particle mean diameter, as determined by a particle size analyzer, is 23.5±2.37 µm; the gap/particle ratio is 8.5. PANI particle electrical conductivity is $2.93 \cdot 10^{-9}$ S/cm. A PANI of low conductivity was chosen in order to be able to investigate ER behavior at high electric field strength without current leakage in the system [12].

The dynamic moduli, G' and G'', were measured in the frequency range 1–100 rad/s. In an ER system, in the absence of a field, the particles are randomly dispersed in suspension and the dynamic moduli generally exhibit liquid-like behavior such that G'' is significantly larger than G' over the entire frequency range. On application of a field, the particles form strings or columns spanning the gap between the electrodes, as a result of interfacial polarization due to migration of charge carriers in the PANI particle [16]. As the electric field strength increases to a critical value, the ER fluid passes through a series of transformations [12]. Two characteristic transition points can be identified rheologically: the first is the sol-gel transition, characterized by the appearance of identical power law frequency scaling of the storage and loss moduli [17], and, subsequently, the liquid-to-solid transition associated with the crossover where G' becomes larger than G'', the latter coinciding with the visible appearance of fibrillar structures [12, 17].

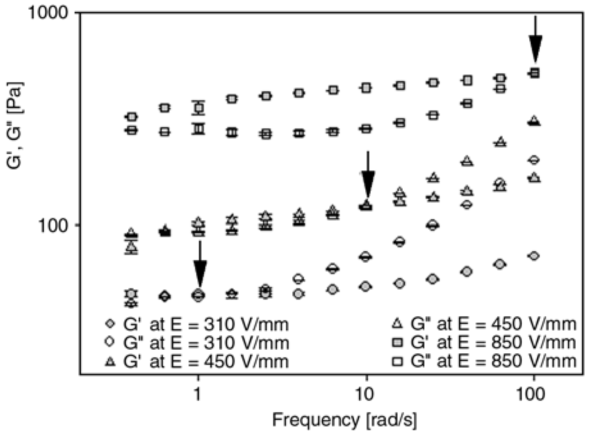

Figure 1. Frequency dependence of the shear moduli of the PANI/500 suspension at various electric field strengths, measured at a strain amplitude of 2%, a temperature of 27±1°C, and gap width = 0.2 mm.

Figure 1 shows the change in $G'(\omega)$ and $G''(\omega)$ of the PANI/500 suspension as the applied field strength is increased. Evidently at the lowest deformation frequencies, G' is greater than G'', indicative that the polarization-induced fibrillar structures have formed, i.e. we are beyond the liquid-to-solid transition in this frequency range. Of more interest in this study is the fact that, at higher frequencies, indicated by arrows, we observe a second G'-G'' crossover, where G'' becomes larger than G', characteristic of the onset of the high frequency relaxation process believed to be that identified in the molecular dynamics simulations [1]. It can be seen in Figure 1 that the crossover frequency, ω_c, increases with electric field field strength, e.g. E = 850 V/mm for ω_c = 100 rad/s as compared with E = 310 V/mm for ω_c = 1 rad/s.

3.2. Effect of the host fluid viscosity and the strain amplitude

Figure 2a shows the correlation between electric field strength and crossover frequency for various PANI/silicone oil suspensions having different host

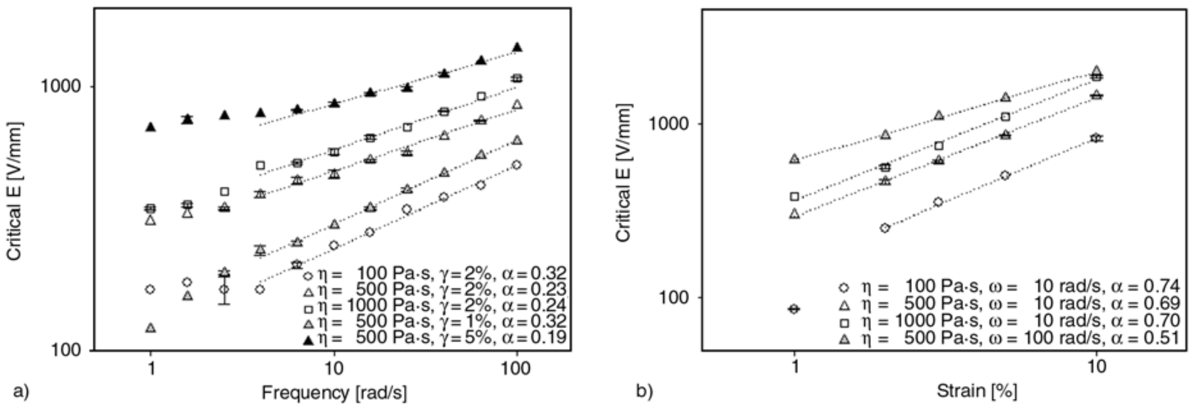

Figure 2. The dependence of critical electric field strength on: (a) frequency; and (b) strain amplitude for various PANI suspensions having different silicone oil viscosities, measured at temperature of 27±1°C, gap = 0.2 mm

viscosities. Included are data for PANI/100, PANI/500, and PANI/1000, all measured at a strain $\gamma = 2\%$, as well as PANI/500 measured at $\gamma = 1\%$ and $\gamma = 5\%$. Figure 2 further illustrates that a higher electric field strength, E, correlates with a higher crossover frequency, ω_c, and, in addition indicates that increased matrix viscosity leads to a higher electric field strength at a specified ω_c. Figure 2b indicates that increased strain amplitude leads to a higher electric field strength when ω_c is held constant. The correlation between $\log E$ and $\log\gamma$ at fixed crossover frequency is linear as shown in Figure 2b, which indicates a power law relationship. Figure 2b further indicates that, at a fixed strain amplitude E increases with increasing matrix viscosity at a fixed ω_c.

These results are qualitatively consistent with the theoretical model that assumes the relaxation mechanism depends on the competition between hydrodynamic and polarization forces between particles within thick fibrillar columns [1]. Thus we may deduce that the onset of the relaxation process correlates with the condition where the two opposing forces, i.e. the shear force, F_{shear}, and the electrostatic force, F_{elec}, are in balance. In such a case we may use an argument proposed by Sakurai *et al.* [14] to relate the field strength to the crossover frequency, strain amplitude, matrix viscosity, and particle conductivity. Specifically, since, according to Equation (1):

$$F_{shear} = 6\pi\eta_m\omega\gamma\left(\frac{d}{2}\right)^2 \tag{1}$$

where d is the (assumed spherical) particle diameter, η_m is the matrix viscosity and, according to Equation (2):

$$F_{elec} = \frac{3\pi p^2}{8\varepsilon_m d^4} \tag{2}$$

where ε_m is the matrix dielectric constant and p is the induced dipole moment, which, in the presence of a d_c field may be written as Equation (3):

$$p = \frac{\pi}{2}\varepsilon_m\left(\frac{d}{2}\right)^3\left(\frac{\sigma_p - \sigma_m}{\sigma_p + 2\sigma_m}\right)E = \frac{\pi}{2}\varepsilon_m\left(\frac{d}{2}\right)^3\beta E \tag{3}$$

where σ_p and σ_m are the electrical conductivities of PANI particles and matrix, respectively. Equating Equations (1) and (2) we obtained Equation (4) [14]:

$$E_{crit} = \frac{32}{\pi}\sqrt{\frac{\omega_c\gamma\eta_m}{\varepsilon_m\beta^2}} \tag{4}$$

where ω_c is the crossover frequency, γ is the strain amplitude, η_m is the matrix viscosity, and ε_m is the dielectric constant of the matrix. Thus, Equation (4) predicts that $E_{crit}\,\alpha\,\omega_c^{1/2}$ at fixed γ and η_m, and $E_c\,\alpha\,\gamma^{1/2}$ at fixed ω_c and η_m. In comparison, the experimental data in Figures 2a and 2b indicate that indeed $E_c\,\alpha\,\omega_c^{\alpha}$ and $E_c\,\alpha\,\gamma^{\beta}$, but α varies between 0.19–0.32, and β varies between 0.51–0.74 amongst various host fluid viscosities tested. The origin of the discrepancies is not clear. One possibility relates to the fact that Equation (4) pertains to a suspension of monodisperse spheres, whereas the PANI suspension has particles of irregular shapes and a broad particle size distribution. Also, Equation (4) considers only pairwise interactions between particles, and ignores multi-particle interactions [12]. A potential complication in the case of the dependence on shear strain is that the experiments extend from the linear to the nonlinear viscoelastic regime. Another factor is that the theoretical model, based on an order of magnitude analysis, assumes that the two primary forces are proportional to each other; in experiments such ideal condition rarely exists due to other secondary forces that may become involved as *Pe* number is varied [7].

3.3. Dimensionless group analysis

Under action of the electric field, an ER suspension experiences several inter-particle forces; the electrostatic force, the Brownian force, the short-range repulsion, the hydrodynamic interaction, as well as other colloidal forces. Dimensionless groups arising from such forces are commonly used to describe and interpret suspension behavior in terms of the relative importance of competing contributions [7].

For steady shear flow, the relative importance of the viscous to the electrostatic polarization forces is described by the Mason number [5], defined by Equation (5):

$$Mn = \frac{\eta_m \gamma}{2\varepsilon_0 \varepsilon_m \beta^2 E^2} \tag{5}$$

The relative importance of viscous to thermal forces is described by the Peclet number [18], defined by Equation (6):

$$Pe = \frac{3\pi \left(\frac{d}{2}\right)^2 \eta_m \gamma}{k_B T} \tag{6}$$

where η_m is the matrix viscosity, γ is the shear rate, ε_0 is the electric permittivity of vacuum, ε_m is the matrix dielectric constant, T is the absolute temperature, and k_B is the Boltzmann constant.

In order to make Equations (5) and (6) applicable for an oscillatory shear flow of PANI suspensions, we replace η_m the steady shear matrix viscosity by η_s the steady shear suspension viscosity ($\eta_s \geq \eta_m$), and finally the steady shear suspension viscosity is replaced by the dynamic suspension viscosity, viz. $\eta'_s(\omega) = G''_s(\omega)/\omega$ and $\gamma = \omega\gamma$. Thus, Equation (5) becomes Equation (7):

$$Mn = \frac{G''_s(\omega)\gamma}{2\varepsilon_0 \varepsilon_m \beta^2 E^2} \tag{7}$$

and Equation (6) becomes Equation (8):

$$Pe = \frac{3\pi \left(\frac{d}{2}\right)^3 G''_s(\omega)\gamma}{k_B T} \tag{8}$$

To calculate *Mn* and *Pe*, we used $\varepsilon_0 = 8.85$ pF/m and $\varepsilon_m = 2.4$ as the electric permittivity of vacuum and the matrix dielectric constant, respectively. The relative conductivity, β, is approximately equal to 1 as $\sigma_m = 7.7\cdot10^{-15}$ S/cm [19] and $\sigma_p = 2.93\cdot10^{-9}$ S/cm are the conductivity values of matrix and particle, respectively. $k_B = 1.38\cdot10^{-23}$ J·K^{-1} is the Boltzmann constant, and $T = 300$ K is the absolute temperature. $d = 23.5$ µm is the average particle diameter.

Figure 3 shows a plot of the dimensionless parameter *Mn* versus *Pe*, at the crossover frequency for the PANI/silicone oil suspensions at various viscosities, shear frequencies and strain amplitudes. It is evident that the data points for all systems approximately collapse into a single function of the dimensionless parameter *Pe*, which corresponds to a least squares scaling relation of the form $Mn = 0.0605(Pe)^{0.09}$.

Several different definitions of the Mason number can also be used, and we also tested the scaling relation between *Mn* and *Pe* using the Sakurai definition of *Mn*, based on Equations (1) and (2) for F_{elec} and F_{shear}, respectively, viz. Equation (9):

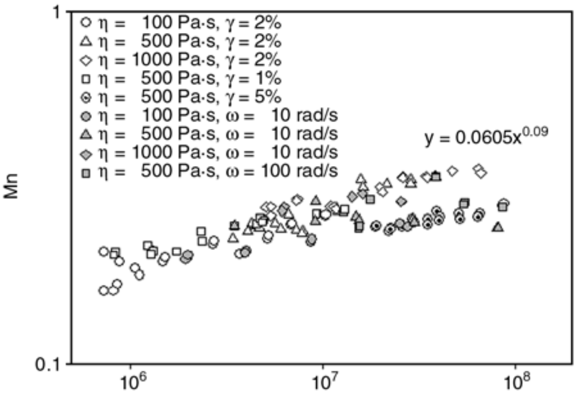

Figure 3. The dimensionless parameter *Mn* versus *Pe* for PANI suspensions having different silicone oil viscosities.

$$Mn_{Sakurai} = \frac{4d^6 \varepsilon_m G_s''(\omega)\gamma_0}{p^2} \qquad (9)$$

where p is the dipole moment induced by Maxwell-Wagner type-polarization, given by Equation (3). Combining Equation (2) for F_{shear} with an expression for the thermal force $F_{thermal} = k_B T/(d/2)$ [5], one obtains Equation (10), an expression for the Peclet number slightly different from Equations (8):

$$Pe_{Sakurai} = \frac{3\pi d^3 G_s''(\omega)\gamma}{4k_B T} \qquad (10)$$

The corresponding plot of $Mn_{Sakurai}$ versus $Pe_{Sakurai}$ is shown in Figure 4, and leads to a scaling relation of $Mn = 6{,}79(Pe)^{0{,}09}$.

In discussing the results in Figures 3 and 4, we note, first, that, since Pe is of the order 10^6–10^9, and Mn of the order 0.1–1.0 or 10–10^2, depending on which definition is used, it is clear that the magnitude of the Brownian force is relatively small in comparison to the shear and electrostatic forces. Also, the scaling exponent 0.09 indicates that the Mason number, as defined in either Equation (7) or Equation (9), is not quite a universal constant at the crossover frequency. Specifically, bearing in mind that only isothermal data were obtained in these experiments, Figures 3 and 4, indicate, over the range of conditions studied, Mn increases by about 30% whereas the shear force increases by over two decades. The dependence of Mason number on Pe number can be interpreted as follows: as the viscous shear force is increased, or Pe number is increased, the electrostatic force required to keep the fibrillar structures from rupture becomes proportionally less. The argument can be also cast in terms of the Brownian force which becomes relatively smaller as Pe number is increased; thus a smaller magnitude of the electrostatic force is required to keep the structure intact.

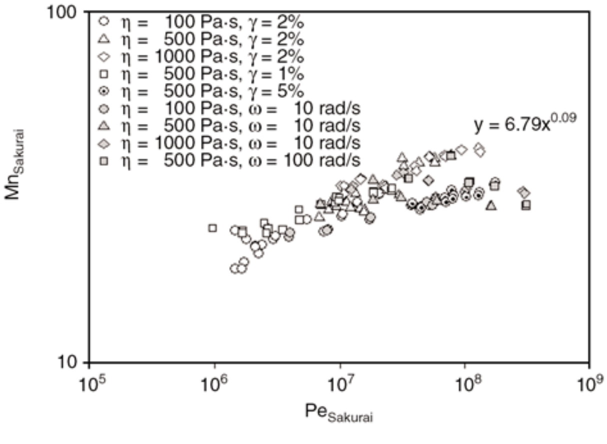

Figure 4. The dimensionless parameter $Mn_{Sakurai}$ versus $Pe_{Sakurai}$ for PANI suspensions having different silicone oil viscosities.

4. Conclusions

Polyaniline (PANI) was synthesized via the oxidative coupling polymerization in acid conditions and de-doped in 3% NH_4OH. The ER properties of PANI/silicone oil suspensions were investigated with a particular focus on the crossover in the storage and loss shear moduli which signals the onset of a high frequency relaxation process associated with the motion of PANI particles within the fibrillar columns produced by the applied field. The relationship between the electric field strength (E) and the deformation frequency (ω_c) at the crossover point was investigated as a function of medium viscosity and shearing amplitude. Qualitatively consistent with a theoretical model, which relates the relaxation process to competition of hydrodynamic and electrostatic forces between polarizable particles within the fibrillar columns, the value of E_c increases with increase in each of these three system variables. Quantitative deviations from the theory are found however, manifested as deviations in the scaling exponent of the dependences of E_c on shearing frequency and strain amplitude from the predicted values of 0.5. The dimensionless parameters, Mason number (Mn) and Peclet number (Pe), of the suspension at the critical point were also studied. Data plotted as Mn versus Pe, for all systems approximately collapse into a single function of the form $Mn = 0.0605(Pe)^{0.09}$. This indicates the Mason number is not a universal constant at the crossover point, but that there is an approximate universal scaling between the viscous stress and the electrostatic polarization stress.

Acknowledgements

The authors would like to acknowledge the financial supports provided by The Thailand Research Fund (TRF), RGJ grant no. PHD/0234/2544 and BRG; the Conductive & Electroactive Polymers Research Unit of Chulalongkorn University; the Royal Thai Government (Budget of Fiscal Year 2551); and the Petroleum Petrochemical and

Advanced Materials Consortium. AMJ would like to acknowledge the support from the US National Science Foundation.

References

[1] Klingenberg D. J.: Simulation of the dynamic oscillatory response of electrorheological suspensions: Demonstration of a relaxation mechanism. Journal of Rheology, **37**, 199–214 (1993).

[2] Tao R., Sun J. M.: Three-dimensional structure of induced electrorheological solid. Physical Review Letters, **67**, 398–401 (1991).

[3] Choi H. J., Cho M. S., To K.: Electrorheological characterization of polyaniline dispersions. Physica A, **254**, 272–279 (1998).

[4] Jang W. H., Kim J. W., Choi H. J., Jhon M. S.: Synthesis and electrorheology of camphorsulfonic acid doped polyaniline suspensions. Colloid and Polymer Science, **279**, 823–827 (2001).

[5] Marshall L., Zukoski IV C. F., Goodwin J. W.: Effects of electric fields on the rheology of nonaqueous concentrated suspensions. Journal of the Chemical Society, Faraday Transactions 1: Physical Chemistry in Condensed Phases, **85**, 2785–2795 (1989).

[6] Toor W.: Structure formation in electrorheological fluids. Journal of Colloid and Interface Science, **156**, 335–339 (1993).

[7] Parthasarathy M., Klingenberg D. J.: Electrorheology: Mechanisms and models. Materials Science and Engineering: R: Reports, **17**, 57–103 (1996).

[8] Cho M. S., Lee J. H., Choi H. J., Ahn K. H., Lee S. J., Jeon D.: Linear viscoelasticity of semiconducting polyaniline based electrorheological suspensions. Journal of Materials Science, **39**, 1377–1382 (2004).

[9] Chotpattananont D., Sirivat A., Jamieson A. M.: Electrorheological properties of perchloric acid-doped polythiophene suspensions. Colloid and Polymer Science, **282**, 357–365 (2004).

[10] Kim J. W., Choi H. J., Lee H. G.: Damping characteristics of polyaniline-based electrorheological fluid. Journal of Industrial and Engineering Chemistry, **7**, 218–222 (2001).

[11] Lin D. D., Zhang Z. J., Zhao B. Y., Chen L. S., Hu K.: Rapid synthesis of porous polyaniline and its application in electrorheological fluid. Smart Materials and Structures, **15**, 1641–1645 (2006).

[12] Hiamtup P. A., Sirivat A., Jamieson A. M.: Electrorheological properties of polyaniline suspensions: Field-induced liquid to solid transition and residual gel structure. Journal of Colloid and Interface Science, **295**, 270–278 (2006).

[13] Pinto N. J., Acosta A. A., Sinha G. P., Aliev F. M.: Dielectric permittivity study on weakly doped conducting polymers based on polyaniline and its derivatives. Synthetic Metals, **113**, 77–81 (2000).

[14] Sakurai R., See H., Saito T., Sumita M.: Effect of matrix viscoelasticity on the electrorheological properties of particle suspensions. Journal of Non-Newtonian Fluid Mechanics, **81**, 235–250 (1999).

[15] Cao Y., Andreatta A., Heeger A. J., Smith P.: Influence of chemical polymerization conditions on the properties of polyaniline. Polymer, **30**, 2305–2311 (1989).

[16] Block H., Kelly J. P., Qin A., Watson T.: Materials and mechanisms in electrorheology. Langmuir, **6**, 6–14 (1990).

[17] Chin B. D., Winter H. H.: Field-induced gelation, yield stress, and fragility of an electro-rheological suspension. Rheologica Acta, **41**, 265–275 (2002).

[18] Melrose J. R.: Brownian dynamics simulation of dipole suspensions under shear: The phase diagram. Molecular Physics, **76**, 635–660 (1992).

[19] Rejon L., Manero O., Lira-Galeana C.: Rheological, dielectric and structural characterization of asphaltene suspensions under DC electric fields. Fuel, **83**, 471–476 (2004).

eXPRESS Polymer Letters Vol.2, No.10 (2008) 695–704
Available online at www.expresspolymlett.com
DOI: 10.3144/expresspolymlett.2008.83

Effects of carbon blacks with various structures on vulcanization and reinforcement of filled ethylene-propylene-diene rubber

Z. H. Li, J. Zhang, S. J. Chen*

College of Materials Science and Engineering, Nanjing University of Technology, Nanjing 210009, P. R. China

Received 10 June 2008; accepted in revised form 27 August 2008

Abstract. The effects of carbon blacks on vulcanization and mechanical properties of filled ethylene-propylene-diene rubber (EPDM) are investigated, by comparing with five types of rubber-grade carbon blacks. Curing kinetics is studied by rheometer and the results indicate that the curing characteristics are influenced by combination of surface area of carbon black and sulphur content on the filler surface, because the former one enhances the physical cross-linking and the latter one introduces the additional chemical cross-linking. Both the degree of cross-linking and cure rate increase with increasing surface area and sulphur content, whereas the optimum cure time and scorch time decrease. The reinforcing nature of the carbon black is assessed from mechanical measurements. It is suggested that the surface area of carbon blacks strongly affects the physical properties of EPDM/carbon black composites. Conductive carbon black (N472) can be used as desirable reinforcing filler due to the higher degree of cross-linking of EPDM with N472 than other EPDM/carbon black composites. The morphology and distribution of particles are studied by using scanning electron microscope. The sound reinforcing ability of N472 is also supported by scanning electron microscope due to the notable dispersibility of N472 within EPDM matrix. N472 ensures the EPDM/N472 composite the most conductive sample among the five composites.

Keywords: *polymer composites, ethylene-propylene-diene rubber, carbon black, cure kinetics, mechanical properties*

1. Introduction

Elastomers are presently used in wide areas of application, such as wires, cables and automobiles, due to their light weight, hydrophobicity, easy maintenance and processing. Nevertheless, they have been usually applied in the filled state since Mote and others discovered the reinforcement of rubber by carbon black a century ago [1]. Reinforcing fillers include carbon blacks, silica and resins, which increase the strength of vulcanized rubber more than tenfold [2, 3]. Filling carbon blacks in elastomers and plastics also reduces the cost of the end product and modifies the electrical and optical properties of the polymer matrix [4, 5].

Reinforcement of rubber by carbon blacks has been intensively studied [6–9]. It is generally accepted that the reinforcement of elastomers and the improvement of other properties, to a large extent, are associated with the chemical and physical interactions between the polymer matrix and carbon blacks [10–14]. Thus, researchers try to explain the improved performance of rubber from the microscopic view, relating the observation of cure kinetics and mechanical properties with the interactions between elastomers and carbon blacks [15, 16]. The entanglement of rubber molecules on the carbon black surface is supposed to play an important role for rubber attachment on carbon blacks [9]. The aggregate anisometry is associated with the

---

*Corresponding author, e-mail: zhangjun@njut.edu.cn

Table 1. Surface and structure parameters for the carbon blacks under study

Samples	SCB	N770	N550	N330	N472
Surface parameters					
S_{BET} [m^2/g]	8.20	15.80	37.80	81.10	1039.50
S_{ex} [m^2/g]	4.87	13.55	33.38	68.36	981.62
Elements on the surface (at.%)					
Carbon	92.80	88.50	92.74	89.85	90.52
Oxygen	6.76	11.50	6.97	9.35	8.50
Sulphur	0.44	*	0.29	0.70	0.97

Note: S_{BET} – standard BET specific surface areas; S_{ex} – external surface area; *not detected

DBP absorption capacity, which is proportional to the entangled rubber chains [6]. Also, the adsorption of ethylene-propylene-diene rubber (EPDM) upon the surface of carbon blacks was studied by Litvinov and coworkers via nuclear magnetic resonance (NMR) [8]. They found the rubber molecule physically adsorbed on the carbon black surface and the reinforcement increases as the EPDM-carbon black interfacial area enhances. Park and coworkers did a lot of work about the relationship between the surface energy of carbon blacks and the resulting mechanical properties of carbon black/rubber composites [16-18]. They concluded that an increase of nonpolar characteristics (London dispersive component of the surface energy of carbon blacks), which is affected by the specific surface area, results in increasing vulcanization reactions and improvements of the mechanical properties of the composites [17]. Besides the specific area, the surface chemistry of carbon black has a significant effect on the properties of carbon black filled elastomers. It is reported that the mechanical properties of composites correspondingly changed with the modification of carbon blacks dispersed in the rubbers. Léopoldès's group found that higher 100% and 300% moduli were observed for the natural rubber filled with a modified carbon black, which was treated by oxidative gas [19]. Scanning electron microscope (SEM) is a technique used to probe the filled rubber [20, 21]. The carbon black mainly exists as the primary aggregation in rubber [2, 22].

The priority of preparing favorable rubber is to obtain the tailor-made cure and mechanical properties. Thus, in this work we compare the cure kinetic characteristics and mechanical properties of EPDM filled with conductive carbon black and other rubber-grade carbon blacks, in order to arrive at a comprehensive understanding of the influences of the structure of the carbon black on the EPDM/carbon black composites.

2. Experimental

2.1. Materials

The samples of EPDM (J-4045) are supplied by Jilin Chemical Industrial Company limited, China. The content of ethylidene norbornene (ENB), the third monomer of EPDM, is 8.0 wt%. According to the standard ASTM D1765-06, the carbon black used in this work includes high abrasion furnace (N330), and fast extruding furnace black (N550) (both N330 and N550 are from Suzhou Carbon Black Plant, China), semi-reinforcing furnace black (N770, Luzhou Carbon Black Plant, China), spraying carbon black (SCB, Fushun Carbon Black Company Ltd., China) and conductive carbon black (N472, HG-1B, Huaguang Chemical Company, China). The main structural parameters of carbon blacks are listed in Table 1.

2.2. Compounding of EPDM

The compounding formulations (in weight per hundred weight of rubber (phr)) used in this work are listed in Table 2. The mixing or compounding of EPDM with dicumyl peroxide (DCP) and other additives was carried out in a two roll mixer (Shanghai rubber machinery works, China) at 30~40°C, following the conventional technique [23]. An overall mixing time of 15 min was

Table 2. Formulation of mixes

Ingredients	Loading [phr]
EPDM gum stock	100
Zinc oxide	5
Stearic acid	1
DCP	4
Antioxidant 4010NA	1
Carbon Black	30

allowed in each case to ensure uniform and efficient dispersion of the carbon black filler particles in the elastomer matrix.

2.3. Vulcanization of EPDM

The vulcanization characteristics of the EPDM/carbon black composites were determined in an oscillating disk cure meter (Wuxi Liyuan Electronically Chemical Equipment Co. Ltd., China), based on ASTM D 2084-01, at 160°C. The optimum cure time was obtained from torque-time curves given by the rheometer. The compounded elastomers described earlier were prepared into vulcanizates in a platen vulcanizing press under a pressure of 10 MPa and at a temperature of 160°C for 20 minutes.

2.4. Hardness and tensile test

The hardness of the carbon black filled EPDM vulcanizates was measured by a Shore A durometer following the ASTM D 2240-03 standard. Dogbone shaped specimens (~25 mm long in the middles by ~6 mm wide by ~2 mm thick) for tensile test were cut from plates. Tensile tests (25 mm initial jaw separation, 500 mm/min displacement speed) were performed on a universal mechanical testing machine (China) according to standard ASTM D412-98a.

2.5. SEM

The EPDM/carbon black composite samples were fractured in liquid nitrogen. Then, the cross sections of samples were sputtered with Au in vacuum. The morphology of the cross section of carbon black filled EPDM at the magnification of 5000× and 20 000× was studied by SEM using a JEOL JSM-5900 instrument (Japan) with an accelerating voltage of 15 kV.

2.6. Volume resistivity measurements

The volume resistivity of composites with a high resistivity was measured by a high resistance meter (Shanghai Precision & Scientific Instrument Co., Ltd, China). The resistivity of EPDM filled with N472 was measured by a conventional four-point probe technique in which the electrodes were separated by 1 mm as reported [24]. The four probes were slightly pressed on the EPDM samples to ensure a good contact. The electrical property measurements were all performed at room temperature. The volume resistivity measured by the four point method is calculated as Equation (1):

$$R_v = \frac{Rbh}{l} \tag{1}$$

where R_v is the volume resistivity [Ω·m], R is the electrical resistance [Ω], b and h are the width and height of the sample, respectively (the section area is the value that b multiple by h), and l is the distance between the two probes (1 mm in this work).

3. Results and discussion

3.1. Cure kinetics

The rheometer, a convenient instrument to evaluate the effects of carbon black-rubber interactions on rate of cure and cross-linking, was employed for the purpose of characterizing critical parameters related to the vulcanization process. Figure 1 shows the separate vulcanization curves of EPDM/carbon black composites at 160°C, associated with the various natures of carbon blacks. As illustrated in

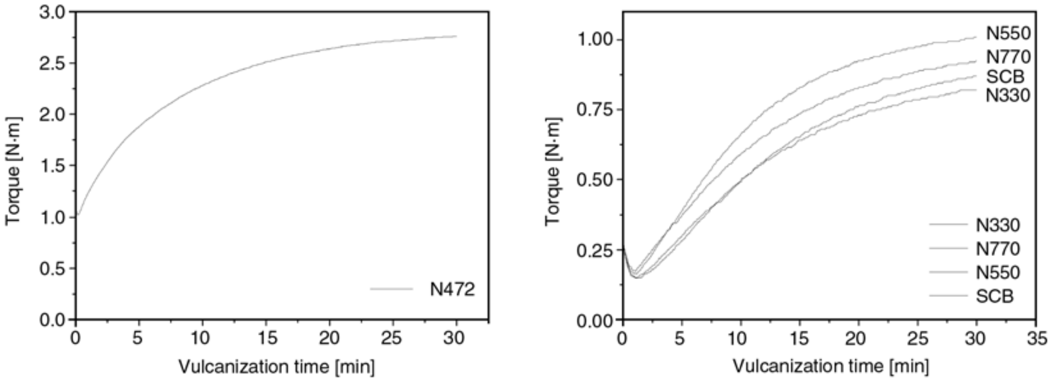

Figure 1. Rheocurves of the EPDM/carbon black composites at 160°C filled with: (a) conductive carbon black; (b) other 4 types of carbon blacks

Table 3, the minimum torque, M_L (1.03 N·m), the maximum torque, M_H (2.76 N·m), and the difference between them, $\Delta M = (M_H - M_L)$ (1.73 N·m), of N472 are much higher than those of other carbon blacks. This is not surprising if physical and chemical interactions of EPDM and carbon black are fully studied.

While the uncured EPDM is being blended well with carbon black for a period of time, EPDM chains have a certain probability to contact with carbon black, and entangle or trap in the voids of carbon black aggregates. As displayed in Figure 2, the rubber chains become highly immobilized and localized, and form a rubber shell, with an estimated thickness of 0.7 nm, surrounding the carbon black particles [9]. Figure 3 demonstrated that those carbon black particles whose surfaces were covered by entangled EPDM chains can be considered as physical cross-links [8]. The physical cross-linking hinders the mobility of rubber chains and restrains the deformation of rubber; thus the M_L of filled EPDM enhances even it is at the uncured state.

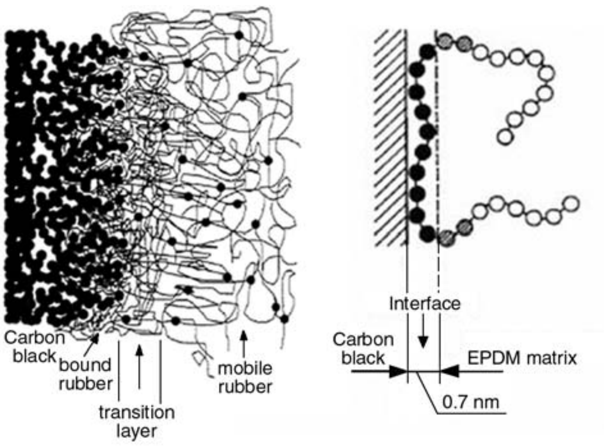

Figure 2. Sketch of the entanglement of rubber chains with carbon black: (a) The entanglement of EPDM chains on carbon black; (b) The thickness of the interface between carbon black and EPDM matrix [8, 9]

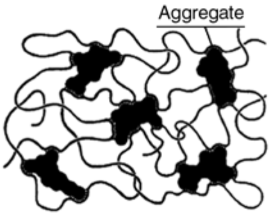

Figure 3. Scheme of the physical network structure in a carbon black filled elastomers [8]

Hence, it is understandable that development of a large polymer-filler interface is the most important factor for the degree of reinforcement provided by filler. Therefore, the surface area of carbon black is of great importance for the density of the physical cross-linking. As the surface area of carbon black increases, the number of rubber chains entangling with carbon black aggregates as well as that of the cross-links climbs up [8]. The entanglement of polymer chains with carbon black increases the torque; thereby the carbon black serves as physical cross-links in rubbers. M_L, the torque of melting uncured rubbers at 160°C, is an indicator of the degree of physical cross-linking.

Most properties, such as Mooney viscosity and 300% modulus, of filled rubber depend on the specific surface area of carbon black, and M_L is the one of them [6]. M_L increases correspondingly with the increasing surface area of carbon black, as the number of rubber chains immobilized on the carbon black surfaces grows up. It can be seen in Table 1 that both the BET specific surface area (1039.50 m^2/g) and external surface area (981.62 m^2/g) of N472 are remarkably higher than those of other carbon blacks, even over 100 times larger than the lowest value. Moreover, not only N472 but also other 4 types of carbon blacks confirm the surface area of particle has a great impact on the M_L. The M_L of all 5 types of carbon blacks exhibit the strikingly similar order with that of carbon black surface area. The physical EPDM-filler interaction explains that the surface area of carbon

Table 3. Vulcanization properties of the carbon black/EPDM composites

	SCB	N770	N550	N330	N472
M_L [N·m]	0.15	0.15	0.16	0.17	1.03
M_H [N·m]	0.87	0.82	1.01	0.93	2.76
ΔM [N·m]	0.72	0.67	0.85	0.76	1.73
T_{S1} [min]	4.23	3.80	2.93	2.97	0.52
T_{90} [min]	22.40	21.95	20.40	21.67	17.77
V_{C1}	5.50	5.51	5.72	5.35	5.80

Note: M_H – the maximum torque; M_L – the minimum torque; $\Delta M = M_H - M_L$; T_{S1} is equal to the time for 0.1 N·m that rise above M_L; T_{90} – optimum cure time, the time for the torque that is equal to the 90% of ΔM; V_{C1} is Cure Rate Index black plays a major role for influencing the M_L of EPDM/carbon black composite.

M_L is cure property measured in the uncured state; nevertheless, ΔM is the characteristic of the cured rubbers. During the vulcanization process, the chemical cross-linking forms based on the reaction of rubbers with vulcanization reagent [25]. ΔM, the difference between M_H and M_L, is thereby considered as the parameter to demonstrate the degree of chemical cross-linking. The ΔM of all EPDM filled with five types of carbon blacks are supposed to be comparable, because the same type of vulcanization reagent (DCP in this work) is equally loaded. The fact, however, is that M_H and ΔM of the filled EPDM vary with the type of the carbon black.

Hence, it is evident that the reaction of rubbers with vulcanization reagent is merely one factor influencing the cross-linking process. The other one is the chemical bonding of rubbers with the functional groups on carbon blacks [2, 6, 7]. The chemical bonding of rubbers with carbon blacks increases the degree of chemical cross-linking. Sulphur on the surface of carbon blacks most probably improved the vulcanization. It is noted in Table 1 that sulphur is observed on the surfaces of four types of carbon blacks. It is accepted that sulphur vulcanization takes place at an appropriate temperature as long as the recipe includes a sulphur donor, zinc oxide, fatty acid [26]. Therefore, according to the report, sulphur cross-links form during vulcanization since the carbon blacks with sulphur on the surface can be considered as the sulphur donors and the ingredients of the recipe mentioned can be found in formulation of EPDM composites. Further investigation shows that the ΔM is in the same order as the amount of sulphur (elemental composition multiple with external surface area of carbon black) when N330 is excluded. The ΔM of EPDM filled with N770 is merely 0.67 N·m, less than other composites, due to the absence of sulphur on the surface of N770. Thus, EPDM filled with N770 is the only rubber which vulcanizes without the influence of sulphur on the surface of carbon black. On the other hand, N472 has not only the largest external surface area but also higher value of surface sulphur content than other carbon blacks; therefore, EPDM filled with N472 inevitably has larger ΔM than those filled with other blacks. N330 is the exception because the phenolic group, which is reported to reduce the cross-linking efficiency, is only found on N330 surface; as a result, the value of ΔM (0.76) of N330 is lower than N550 (0.85).

As displayed in Table 3, T_{s1}, T_{90} and V_{C1} are the parameters associated with the vulcanization rate. In this study, despite the peroxide vulcanization, the sulphur on the surface of carbon blacks, as XPS results show, possibly plays an important role in the cross-linking process. The incorporation of sulphur into peroxide vulcanization dramatically reduces the cure time, because sulphur also can react with the ENB in EPDM to form cross-linking [26]. Nevertheless, the content of sulphur is highly associated with the surface area of carbon black. N472 has the largest surface area amongst the carbon blacks under study, and thereby the content of sulphur on N472 is higher than other carbon blacks. This explains that EPDM filled with N472 has the shortest scorch time (T_{s1} = 0.52 min) and optimum cure time (T_{90} = 17.77 min).

According to ASTM standard mentioned earlier, Cure Rate Index (V_{C1}) is a measurement of vulcanization rate based on the difference between optimum vulcanization and incipient scorch time, at which vulcanization begins. V_{C1} = 100/(cure time – scorch time). Therefore, the shortest optimum cure time of EPDM with N472 inevitably results in the highest value of V_{C1} (5.80) among the EPDM/carbon black composites under study. The highest V_{C1} of EPDM with N472 indicates the fastest cure rate in all those 5 types of EPDM/carbon black composites. It is interesting to note that N330 has the lowest cure rate owing to the quinolic group, which slows down the speed of cross-linking process, observed on the surface of N330 [27–29].

The conversion ratio, χ_t, at a given time t is defined as Equation (2) based on the rheocurves, as shown in Figure 4, to compare the rate of vulcanization in details [17].

$$\chi_t = \frac{M_t - M_L}{M_H - M_L} \tag{2}$$

where M_t represents the torque at a given time t, M_H and M_L are the maximum and minimum torques, respectively.

Figure 4 displays the conversion of EPDM/carbon black composites for carbon blacks with different external surface areas as a function of cure time. The rate of conversion of vulcanization reaction under a given condition is observed in the order

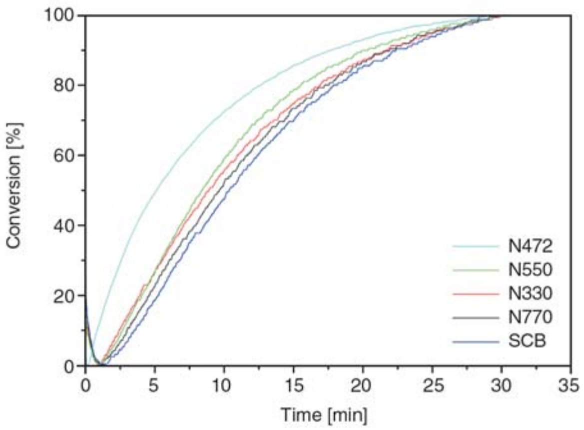

Figure 4. Conversion ratio of the carbon black/EPDM composites

N472 > N550 > N330 > N770 > SCB. For instance, the 50% conversion demands about 5.13 min for N472, 8.41 min for N550, 8.88 min for N330, 9.63 min for N770, and 10.35 min for SCB. The reactivity in vulcanization reaction is raised with increasing surface functional groups of carbon blacks, while the reaction is inhibited by increasing acidity, supported by the appearance of quinolic structure, in the rubber composites [10, 27–29].

Almost all cure characteristics vary proportionately with external surface area, due to more opportunities for formation of the increasing chemical and physical interactions on larger surface. There are also some exceptions. It should be noted that for N330, although with strikingly larger external surface area than N550, the degree of cross-linking and vulcanization rate are lower than those of N550. This is due to the cure retarding effect of quinine and carboxylic acid functionalities attached on the surface of N330 determined in FT-IR [10]. Carbon blacks inhibit free radical reactions through quinonic surface groups; these reactions also result in formation of polymer grafts [2].

3.2. Mechanical properties and reinforcement

During tests of mechanical properties, remarkable modifications of rubbers which are termed as 'reinforcement', both physical and chemical interactions involved. Table 4 indicates five parameters of mechanical properties of EPDM/carbon black composites used to reflect the different reinforcing abilities among those composites.

Hardness, which is one of the most obvious mechanical parameters, varies in a considerable range from 52 to 79 Shore A. The former one corresponds to SCB, while the latter one matches with N472, the carbon black with largest external surface area. The degree of cross-linking has a great effect on the hardness of the elastomer [2]. The highest surface sulphur content of N472 possibly contributes to the hardness of EPDM filled with N472. The higher degree of chemical cross-linking induced by peroxide and sulphur vulcanization and physical cross-linking by entanglement ensure the EPDM vulcanizate the larger ability to resist deformation. Also, it is reported that the rubber chains are entangled with or permanently locked in carbon black aggregates and form a rigid shell. The amount of shell increases with the increasing surface area of carbon black; thus, the largest area of rigid rubber shell is obtained on the N472 surface since it has the largest external surface area, which is accessible for rubber molecules. The rigid shell causes the enhancement of hardness of total EPDM composite. Thus, EPDM filled with N472 is the example that larger particle surface area induces harder composite (79 Shore A).

Plotting the hardness against the surface area, it can be seen from Figure 5 that the hardness jumps up with the external surface area. In addition, the correlation factor (R^2) for the linear regression in this diagram is strikingly high ($R^2 = 0.92$, hardness vs. external surface area of carbon black). This suggests that the external surface area of carbon blacks is indeed a major factor determining the hardness of EPDM/carbon black composites. In fact, this generally agrees with the reports in the literature [6]. According to Litvinov's report, it is not surprising that the surface area of a carbon black contributes markedly to the hardness, because of the external

Table 4. Mechanical properties of EPDM/carbon black composites

	SCB	**N770**	**N550**	**N330**	**N472**
Hardness [Shore A]	57	52	60	59	79
300% modulus [MPa]	4.67	2.91	5.17	5.23	15.12
Tensile strength [MPa]	8.44	12.12	15.04	18.38	17.76
Elongation at break [%]	510	640	526	571	345
Permanent set [%]	12	17	15	15	17

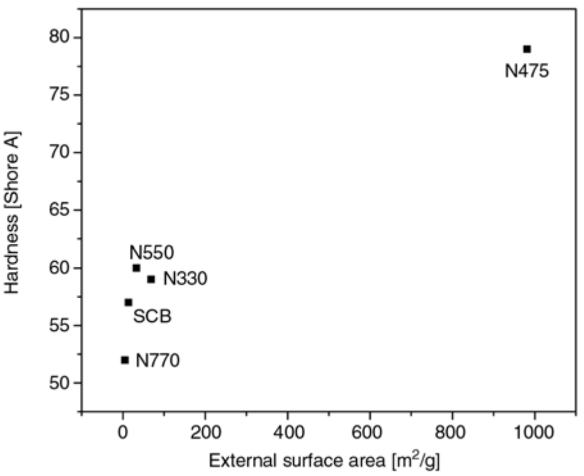

Figure 5. Hardness as a function of the external surface area of carbon blacks

surface which is accessible to polymer chains and provides a place for them to immobilize [8]. And it is reported that the amount of bound rubber increases with the increasing irregularity of filler surface [30]. This is probably due to that, when the filler loading is the same, the larger surface has more irregularity and hence more bound rubber. Thus, it actually can be expected that larger surface area inevitably rises dramatically the possibility of immobilization of rubber molecules on surface of blacks. Therefore, the whole composite transforms from soft to stiff, owing to the loss of segmental mobility of polymer chains and consequently decreased flexibility of the rubber matrix. Similarly, it is reported that high-structure, that is high external surface area, carbon blacks tend to shorten the elongation at break due to its higher strain amplification degree. Therefore, elongation at break of composites, as Table 4 demonstrated, dropped from 640% (N770) to 345% (N472), inversely proportional to the external surface area, and their correlation factor ($R^2 = 0.79$) is reasonably high, indicating the significant effect of surface area [6].

300% modulus, a parameter widely used to characterize the stiffness of rubber vulcanizates, is the stress at 300% extension. The structure of carbon black is one factor to influence the 300% modulus by strain amplification and occluded rubber. In addition, the cross-linking density is another parameter to affect the 300% modulus [2]. As mentioned earlier, the ΔM of EPDM filled with N472 is 1.73, much larger than other composites, suggesting the higher value of density of cross-linking. Hence, it is reasonable that 300% modulus of EPDM filled N472 (15.12 MPa) ranks as the first in all composites. What is more, the correlation factor R_2 of tensile modulus at 300% vs. external surface area is 0.97, also indicating the notable influence of surface area. It is noted that tensile strength of filled EPDM passes through a maximum peak then reduces, as the ΔM, the typical parameter representative cross-linking density, of composite increases. N472 with the shockingly huge surface area has lower tensile strength at break (17.76 MPa) than that of N330 (18.38 MPa). This confirms the literature that the tensile strength experiences the bell curve with increasing density of cross-linking. Thus, it is no surprise that the correlation factor R^2 of tensile strength at break vs. external surface area is only 0.26, but it climbs up to 0.92 when the N472 is excluded.

As far as the elongation at break of filled EPDM is concerned, when plotting it vs. external surface area R^2 is reduced to 0.77. In order to fully understand the influencing factors for elongation of break, it is necessary to thoroughly investigate the breaking process of dumb bell composite samples. During the uniaxial tensile test, the sample was stretched to a large strain, and when the stress exceeds the stress-relieving capacity of the occluded rubber, it begins to rupture [6]. Mechanisms include stress relief and de-wetting. The difference between those two processes is that the former one is detachment of chains in a given area, whereas the latter one is the slippage of weakly bonded chains during large deformation [2]. The number of weak bonds, which are formed by physical adsorption to anchor polymer chains on filler surfaces, is affected by the surface area. Thus, according to above correlation factors R^2, the surface area is one the most important, probably the most important factor which affects mechanical properties. Another factor is the elemental concentration probed by XPS. As the XPS spectra shown, the highest amount of sulphur exists on N472 surface but is not detected on the surface of N770. The cross-linking density, thus, varies with the surface sulphur content. The increasing degree of cross-linking is responsible for the improved mechanical properties of filled rubber, because the action of large number of rubber chains was locked or cross-linked by entanglement and vulcanization. Therefore, the largest degree of cross-linking EPDM filled with N472 leads to the lowest elongation at break (345%) in all composite, acting more like a plastic.

Permanent set is the parameter often applied in the rubber industry to characterize the resilience of the rubber. SCB-containing sample has the lowest permanent set (12%) whereas those of samples filled with N472 and N770 are in the middle position (both are 15%). Samples with N770 and N472 have the highest permanent set (17%).

3.3. SEM

SEM is commonly applied method to observe the morphology of rubber/carbon black composites [22, 31, 32]. The morphologies of the carbon black filled EPDM are shown in Figure 6. The carbon black mainly exits as the aggregates in the rubber matrix [2]. Almost all types of carbon black aggregates distribute uniformly in EPDM. Nevertheless, the size of the carbon black aggregates varies with the type of the carbon black. The carbon black aggregates for N472 and N330 have the smaller sizes than other aggregates. In the SEM of EPDM/N472 and EPDM/N330 composites, the carbon black can be hardly distinguished. Generally, the filler with large surface has a small size. As Table 1 demonstrated, N472 and N330 have the higher BET specific surface areas (1039.50 and 81.10 m^2/g, respectively) than others. Therefore, N472 and N330 have the lower values of the aggregate sizes. The unclear interface between N472 and EPDM indicates the miscibility of N472 with EPDM, which brings to the filled EPDM sound mechanical properties. In addition, in our other research, carbon blacks with small size induce the high value of conductivity into rubber. In the SEM of N770, SCB and N550, the interfaces between carbon black aggregates and the EPDM matrix are evident. Hence, the reinforcing ability of N770, SCB and N550 are less significant than N472. Although N550 has the larger size than N770 in SEM, N550 have higher value of BET specific surface. This is ascribed to the porosity of N550. The rubber molecules are able to access into the particle of N550 but not to that of N770. Thus, N550 has the better reinforcing performance than N770.

3.4. Electrical resistivity

Electrons usually transport easily on the carbon black surfaces. Hence, the addition of carbon blacks not only reinforces the composites but also introduces electrical conductivity into filled rubber. Electrical conduction of filled EPDM has been extensively researched for a period of long time [23, 33]. There are mainly three mechanisms, including conduction path theory, electron tunneling theory and electric field radiation theory, of the

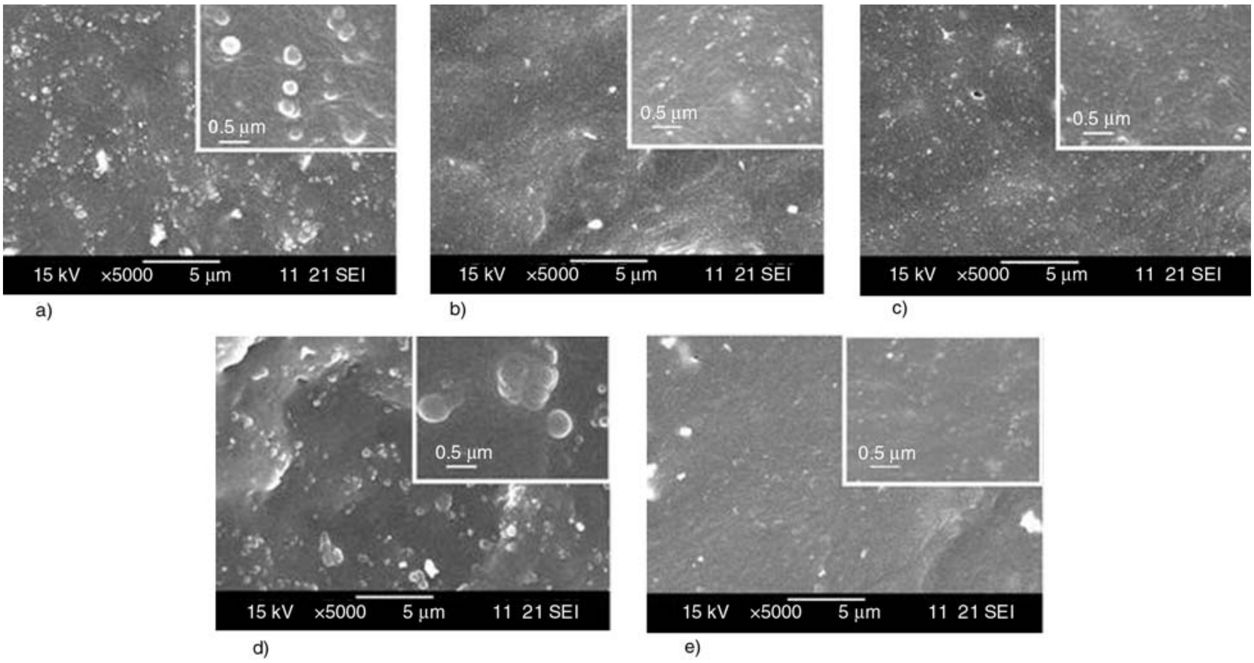

Figure 6. The SEM of EPDM/carbon black composites with different carbon blacks: (a) N770; (b) N330; (c) SCB; (d) N550; (e) N472

Table 5. Volume resistivity of EPDM/carbon black composites

N770[a]	SCB[a]	N550[a]	N330[a]	N472[b]
2.3×10^{14} Ω·m	2.0×10^{14} Ω·m	1.8×10^{11} Ω·m	1.2×10^{10} Ω·m	0.18 Ω·m

Note: a – the sample was characterized by the high resistance meter;
b – the sample was characterized by the conventional four-point technique

electrical conduction in the polymer filled with carbon blacks [30].

The significant factor influencing the electrical conduction mechanisms is the percolation limit. The percolation limit is the loading where the conduction paths start to form. The percolation limit of carbon blacks varies with the surface area. The carbon black with large surface area has low percolation limit. It is noted in Table 5 that the volume resistivity (0.18 Ω·m) of EPDM filled with N472 is considerably lower than other EPDM/carbon black composites. The low resistivity indicates that EPDM with N472 is suitable to be used in conductive applications. The content of N472 (30 phr) effortlessly exceeds the percolation limit. Thereby, the carbon black aggregates of N472 form a few continuous networks by contacting with each other. Consequently, those networks act as the conductive paths in EPDM/N472 composites; thus the volume resistivity is smaller than the lower limit of high resistance meter [34]. The volume resistivity of EPDM filled with N550 and N330 are $1.8\cdot10^{11}$ and $1.2\cdot10^{10}$ Ω·m, respectively. And SCB and N770 have the lower surface areas than other carbon blacks, hence the volume resistivity of EPDM filled with the two carbon blacks are $2.0\cdot10^{14}$ and $2.3\cdot10^{14}$ Ω·m, separately. Accordingly, the EPDM filled with those four types of rubber-grade carbon blacks are the insulators. Their loadings of carbon black are lower than the percolation limit. Therefore, the electron transmission in those carbon black is mainly electron tunneling theory and electric field radiation theory [34]. Additionally, it is reported that the heteroatoms such as oxygen and sulphur on the surface of carbon blacks have effects on the resistivity because some functional groups including OH group traps electrons which transport on the filler surface [30].

4. Conclusions

In this research, the cure kinetics of EPDM filled with conductive carbon black and other rubber grade black were investigated. The vulcanization and mechanical properties of the cured EPDM/carbon black composites were measured. The experimental results show surface area of carbon black as well the sulphur content on the surface of carbon black has influences on the cure kinetics of EPDM/carbon black composites. As the surface area of carbon blacks increases, the physical cross-linking is enhanced. In addition, the sulphur on the surface of carbon black also plays an important role in the vulcanization of EPDM/carbon black composites, since it introduce the additional chemical cross-linking into the system. Mechanical experimental results demonstrate that the composite with conductive carbon black, comparing with other blacks, has the highest hardness, tensile strength at break, tensile modulus at 300% and permanent set. This is due to the high degree of cross-linking of the EPDM filled with N472. The elongation at break of this composite with conductive carbon black is lower than those with other blacks due to the EPDM molecule firmly absorbed on the N472 surface. The SEM results also indicate the sound reinforcing ability of N472 owing to the notable miscibility of N472 with EPDM matrix. The EPDM/N472 composite has the significantly higher volume resistivity than other samples.

References

[1] Blow C. M., Hepburn C.: Rubber technology and manufacture. Butterworth Scientific, London (1982).
[2] Eirich F. R.: Science and technology of rubber. Academic Press, New York (1978).
[3] Khan M. S., Lehmann D., Heinrich G.: Modification of PTFE nanopowder by controlled electron beam irradiation: A useful approach for the development of PTFE coupled EPDM compounds. Express Polymer Letters, **2**, 284–293 (2008).
[4] Pantea D., Darmstadt H., Kaliaguine S., Roy C.: Electrical conductivity of conductive carbon blacks: Influence of surface chemistry and topology. Applied Surface Science, **217**, 181–193 (2003).
[5] Pantea D., Darmstadt H., Kaliaguine S., Roy C.: Heat-treatment of carbon blacks obtained by pyrolysis of used tires. Effect on the surface chemistry, porosity and electrical conductivity. Journal of Analytical and Applied Pyrolysis, **67**, 55–76 (2003).

[6] Donnet J., Vidal A.: Carbon black: Surface properties and interactions with elastomers. in 'Advances in Polymer Science' (eds.: Abe A., Albertsson A-C., Duncan R., Dusek K., de Jeu W. H., Kausch H-H., Kobayashi S., Lee K-S., Leibler L., Long T. E., Manners I., Möller M., Nuyken O., Terentjev E. M., Voit B., Wegner G., Wiesner U.) Springer Berlin, Heidelberg, 103–127 (1986).

[7] Edwards D. C.: Polymer-filler interactions in rubber reinforcement. Journal of Materials Science, **25**, 4175–4185 (1990).

[8] Litvinov V. M., Steeman P. A. M.: EPDM-carbon black interactions and the reinforcement mechanisms, as studied by low-resolution ^{1}H NMR. Macromolecules, **32**, 8476–8490 (1999).

[9] Heinrich G., Vilgis T. A.: Contribution of entanglements to the mechanical properties of carbon black-filled polymer networks. Macromolecules, **26**, 1109–1119 (1993).

[10] Barlow F. W.: Rubber compounding: Principles, materials, and techniques. Marcel Dekker, New York, (1988).

[11] Wolff S., Wang M. J.: Filler-elastomer interactions. Part III: Carbon-black-surface energies and interactions with elastomer analogs. Rubber Chemistry and Technology, **64**, 714–735 (1991).

[12] Wolff S., Wang M. J.: Filler-elastomer interactions. Part IV: The effect of the surface energies of fillers on elastomer reinforcement. Rubber Chemistry and Technology, **65**, 329–342 (1992).

[13] Wolff S.: Chemical aspects of rubber reinforcement by fillers. Rubber Chemistry and Technology, **69**, 325–346 (1996).

[14] Fröhlich J., Niedermeier W., Luginsland H. D.: The effect of filler-filler and filler-elastomer interaction on rubber reinforcement. Composites Part A: Applied Science and Manufacturing, **36**, 449–460 (2005).

[15] Leblanc J. L.: Rubber-filler interactions and rheological properties in filled compounds. Progress in Polymer Science, **27**, 627–687 (2002).

[16] Park S-J., Kim J-S.: Role of chemically modified carbon black surfaces in enhancing interfacial adhesion between carbon black and rubber in a composite system. Journal of Colloid and Interface Science, **232**, 311–316 (2000).

[17] Park S-J., Seo M-K., Nah C.: Influence of surface characteristics of carbon blacks on cure and mechanical behaviors of rubber matrix compoundings. Journal of Colloid and Interface Science, **291**, 229–235 (2005).

[18] Park S-J., Cho K-S., Ryu S-K.: Filler-elastomer interactions: Influence of oxygen plasma treatment on surface and mechanical properties of carbon black/rubber composites. Carbon, **41**, 1437–1442 (2003).

[19] Léopoldes J., Barres C., Leblanc J. L., Georget P.: Influence of filler-rubber interactions on the viscoelastic properties of carbon-black-filled rubber compounds. Journal of Applied Polymer Science, **91**, 577–588 (2004).

[20] Wang J. H., Liang G. Z., Yan H. X., He S. B.: Mechanical and dielectric properties of epoxy/dicyclopentadiene bisphenol cyanate ester/glass fabric composites. Express Polymer Letters, **2**, 118–125 (2008).

[21] Das A., Jurk R., Stöckelhuber K. W., Heinrich G.: Rubber curing chemistry governing the orientation of layered silicate. Express Polymer Letters, **1**, 717–723 (2007).

[22] Zhang A., Wang L., Lin Y., Mi X.: Carbon black filled powdered natural rubber: Preparation, particle size distribution, mechanical properties, and structures. Journal of Applied Polymer Science, **101**, 1763–1774 (2006).

[23] Ghosh P., Chakrabarti A.: Conducting carbon black filled EPDM vulcanizates: Assessment of dependence of physical and mechanical properties and conducting character on variation of filler loading. European Polymer Journal, **36**, 1043–1054 (2000).

[24] Chen S., Chen W., Si Z., Zhou D., Xue G.: Preparation of size controllable polypyrrole sub-Microcapsules using SEBS copolymer as the building block. Macromolecular Rapid Communications, **27**, 328–332 (2006).

[25] Habeeb Rahiman K., Unnikrishman G., Sujith A., Radhakrishnan C. K.: Cure characteristics and mechanical properties of styrene-butadiene rubber/acrylonitrile butadiene rubber. Materials Letters, **59**, 633–639 (2005).

[26] Akiba M., Hashim A. S.: Vulcanization and crosslinking in elastomers. Progress in Polymer Science, **22**, 475–521 (1997).

[27] Zaper A. M., Koenig J. L.: Solid state carbon-^{13}NMR studies on vulcanized elastomers. III: Accelerated sulfur vulcanization of natural rubber. Rubber Chemistry and Technology, **60**, 278–297 (1987).

[28] Morita E.: Correlation analysis of curing agents. Rubber Chemistry and Technology, **57**, 744–754 (1984).

[29] Cotten G.: The effect of carbon black surface properties and structure on rheometer cure behavior. Rubber Chemistry and Technology, **45**, 129–144 (1972).

[30] Medalia A. I.: Electrical conduction in carbon black composites. Rubber Chemistry and Technology, **59**, 432–454 (1986).

[31] Guriya K. C., Tripathy D. K.: Morphology and physical properties of closed-cell microcellular ethylene-propylene-diene terpolymer (EPDM) rubber vulcanizates: Effect of blowing agent and carbon black loading. Journal of Applied Polymer Science, **62**, 117–127 (1996).

[32] Akovali G., Ulkem I.: Some performance characteristics of plasma surface modified carbon black in the (SBR) matrix. Polymer, **40**, 7417–7422 (1999).

[33] Sau K. P., Chaki T. K., Khastgir D.: The change in conductivity of a rubber-carbon black composite subjected to different modes of pre-strain. Composites Part A: Applied Science and Manufacturing, **29**, 363–370 (1998).

[34] Sau K. P., Chaki T. K., Khastgir D.: Conductive rubber composites from different blends of ethylene-propylene-diene rubber and nitrile rubber. Journal of Materials Science, **32**, 5717–5724 (1997).

eXPRESS Polymer Letters Vol.2, No.10 (2008) 705–717
Available online at www.expresspolymlett.com
DOI: 10.3144/expresspolymlett.2008.84

FE simulation of the indentation deformation of SiC modified vinylester composites in respect to their abrasive wear performance

D. Felhős[1], *R. Prehn*[1], *K. Váradi*[2], *A. K. Schlarb*[1]

[1]Institut für Verbundwerkstoffe GmbH (Institute for Composite Materials), Kaiserslautern University of Technology, D-67663 Kaiserslautern, Erwin-Schrödinger-Straße, Germany
[2]Department of Machine and Product Design, Budapest University of Technology and Economics, H-1111 Budapest, Műegyetem rkp. 3., Hungary

Received 10 June 2008; accepted in revised form 1 September 2008

Abstract. The abrasive sliding friction and wear behaviours of silicon carbide (SiC) filled vinylester (VE) composites were investigated. The average grain size of the incorporated SiC particles was varied, holding the volume content of them in every case at 16 vol%. Mechanical properties (hardness, compression modulus, yield stress) of the filled and neat VE were determined. The tribological properties were investigated in block (composite) – on – ring (steel) test configuration. The steel counter bodies were covered with abrasive papers of different graining. Coefficient of friction (COF) and specific wear rate of the VE + SiC composites were determined. It was observed that the wear resistance increases with increasing average filler grain size and with decreasing abrasiveness of the counter surface. The COF of the VE + SiC composites is independent of the size of the incorporated particles, but it is strongly influenced by the abrasiveness of the counter body. The worn surfaces of the VE + SiC systems were analysed in scanning electron microscope (SEM) to deduce the typical wear mechanisms. The size effect of the SiC filler particles onto the abrasive wear characteristics was investigated by assuming that the roughness peaks of the abrasive paper and the indenter of the microhardness test cause similar micro scaled contact deformations in the composites. Therefore FE method was used to simulate the micro scaled deformation process in the VE + SiC systems during microindentation tests. The FE results provided valuable information on how to explain the size effect of the incorporated SiC filler.

Keywords: *polymer composites, reinforcements, thermosetting resins, modelling and simulation, abrasive wear*

1. Introduction

For metallic materials a suitable correlation exists between the wear behaviour and the hardness. For polymeric materials such a general usable dependence wasn't found yet. Though some correlations between the wear performance and material properties were already prepared, they are valid always only for special materials and circumstances [1–3]. Especially under abrasive conditions the micro scaled deformation behaviour plays an important role in the wear process, because of the occurring mechanisms like 'micro ploughing' and 'micro cutting'.

Tribotechnical systems are characterised by an interplay between contacting surfaces which are in relative motion to one other. If the surfaces are not separated by a lubricating film (for example sufficient lubricant is not available or its viscosity is too low to produce an appropriate lubricating film thickness) the surfaces are in direct contact. The

---

*Corresponding author, e-mail: david.felhoes@ivw.uni-kl.de

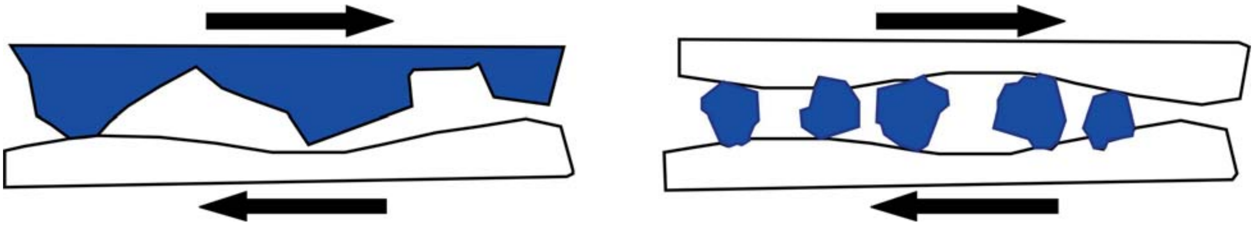

Figure 1. Two body contact (left) and three body contact (right) by abrasive wear process [7]

consequence is the onset of wear. If the counter body is harder and rougher than the base material abrasive wear occurs. The presence of hard particles in the contact area between two surfaces also leads to abrasive wear. Accordingly, the abrasive wear processes can be grouped into two-body and three-body contact ones (see Figure 1) [4, 5].

Abrasive wear events cover different material separation processes listed below. In ductile materials furrows result in chip formation, the related process is called micro cutting. The rising edges of the furrow, caused by surface deformation, are formed by micro plowing (see Figure 2). The relationship between the two processes – micro cutting and micro plowing – is affected also by the inclination angle of the abrasive counter part. In brittle materials beside the edges of the furrow additional cracking and crack growth take place (micro cutting). With multiple furrowing it comes to micro fatigue phenomena [4, 6].

In the case of single path sliding under abrasive conditions the wear rate of pure polymer materials is usually smaller than that of filled composites. However, this behaviour changes with increasing repetitions (multipath sliding), and the composite materials are often better than the neat ones concerning the wear after an initial phase. On the one hand this can be attributed to the formation of a protecting boundary layer between the sliding pairs. The polymer-based boundary layer triggers an adhesion dominated tribological process. On the other hand filler and reinforcement materials are added to improve the wear characteristics, for example internal lubricants such as poly(tetrafluoroethylene) (PTFE) or graphite. Note that filler and reinforcement materials may lower the cohesive forces (binding forces) within the composite. This supports furrowing, tearing and cutting processes. Furthermore, the fillers may act as stress concentrators and the consequence may be prominent cracking and fatigue in the corresponding composite material [8–11].

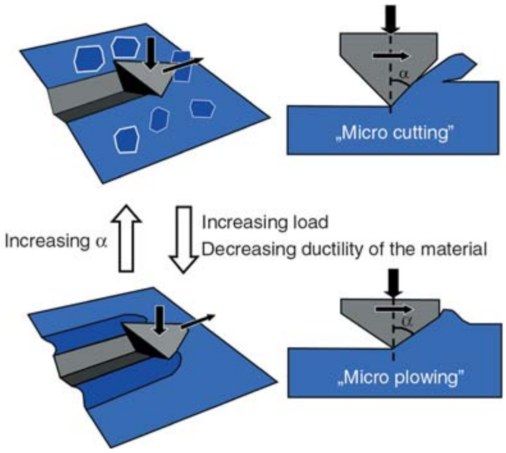

Figure 2. Presentation of both material detachment processes 'micro cutting' and 'micro plowing' [7]

The question arises, how the incorporation of fillers and reinforcements influence the abrasive wear? With the addition of reinforcement materials, like ceramic particles, the wear characteristics under abrasive conditions can be improved, whereby the particle size seems to play an important role [12–14]. To sum up, it can be concluded that the micro scaled deformation behaviour of reinforced composites plays a crucial role in respect to abrasive wear. Penetration conditions of the abrasive particles and/or roughness peaks of the counter bodies (contact angle and load type) are likewise crucial.

The working hypothesis of this study was that there is a correlation between the micro scaled deformation of polymer composites, accessed by micro hardness (Martens hardness) and their abrasive wear behaviour. It was also supposed, that finite element (FE) simulation is the right tool to understand the penetration process of the indenter during Martens tests [15]. The simulation of a dynamic microhardness test for vinylester based composite materials, reinforced with silicon carbide particles, offers the possibility to determine the influence of the particle reinforcement on the micro scaled deformation behaviour of the matrix material. With the results of the FE simulation the opportunity is given to draw conclusions about the wear behaviour under abrasive conditions.

2. Materials and material production

For the modification of the base vinylester (VE) resin silicon-carbide (SiC) was selected as reinforcement material. With the help of the SiC particles both the material stiffness, especially the compression strength, and wear characteristics under abrasive conditions were to be improved. In order to consider the influence of the particle size, SiC particles with a middle grain size of 3 and 9 µm, respectively, were used. Moreover a composite material was produced, which contained SiC particles in both sizes (3 and 9 µm). In each case 16 vol% SiC were incorporated into the VE matrix. Further on these materials will be referred as material A (pure VE resin), material B (VE + 16 vol% SiC (3 µm)), material C (VE + 8 vol% SiC (3 µm) + 8 vol% SiC (9 µm)) and material D (VE + 16 vol% SiC (9 µm)). The exact material compositions are summarized in Table 1.

For the production of the VE composites a laboratory dissolver was used (Dispermat AE3-M, VMA Getzmann GmbH). The used VE (Synthopan UPM, Synthopol Chemistry) contained styrene as crosslinking agent. The styrene content of the VE was 25 vol%. Methyl ethyl ketone based peroxide served as initiator. To crosslink the resin already at ambient temperature, Oldopal 64 (Büfa Reaktionsmittel) accelerator was used, which is based on cobalt and dimethyl aniline. The so called cold crosslinking has the advantage that the sedimentation of relatively large and heavy filler materials can be prevented because the resin begins to gel promptly.

After the mixing process, the materials were poured in forms (dimensions: 100×100×10 mm^3) and hardened at ambient temperature. In order to harden the samples completely, they were transferred into a furnace and kept for 60 minutes at 120°C. Specimens for material characterisation were prepared from these plates.

Table 1. Material compositions of the vinylester-based composites

Material name	Basis-polymer	SiC content (middle grain size)
A	VE	0 vol% (pure resin)
B	VE	16 vol% SiC (3 µm)
C	VE	8 vol% SiC (3 µm) + 8 vol% SiC (9 µm)
D	VE	16 vol% SiC (9 µm)

3. Experimental

3.1. Mechanical properties

In order to be able to simulate the deformation behaviour of the materials, it is necessary to know the elastic modulus (material stiffness) and the yield stress (load where that the plastic deformation begins) of the matrix material under compression. The related tests were accomplished on the pure VE resin (matrix) in accordance with the DIN 604 standard, using an universal test equipment (1474 Zwick, Ulm, Germany). The results are summarized in Table 2.

3.2. Density measurement

The density of the composites was measured using the Archimedes principle (buoyancy method with water) according to the ISO 1183 standard. The density measurements were done at a Mettler AT261 (Giessen, Germany) micro balance.

3.3. Microhardness tests

Microhardness tests were carried out on all materials using a dynamic ultra microhardness testing set (Shimadzu – type DUH 202) following the DIN 50359-1 norm. The measurements were performed at two different maximum loads, 100 and 1500 mN respectively. On each material 10 measurements were made with a test speed of 70 mN/sec. The universal hardness values (*HU*) were derived from the measured penetration force *F* [N] and penetration depth h [mm] values in accordance with Equation (1):

$$HU = \frac{F}{26.43 \cdot h^2} \quad [\text{MPa}] \qquad (1)$$

3.4. Abrasive wear tests

The tribological behaviour of the composites was determined in block-on-ring abrasion tests. This set-up was selected because there is a good analogy between it and the sliding bearings contact situation

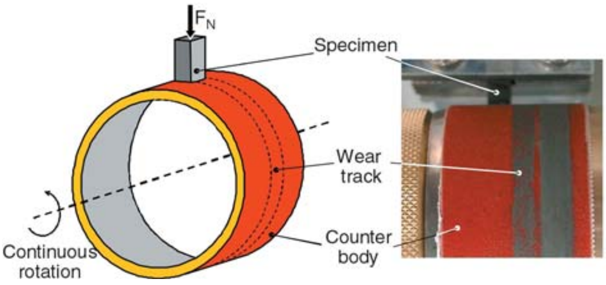

Figure 3. Sketch of the block on ring testing method (left) and a photograph of the set-up (right)

(geometry and movement type). In order to study effects of the abrasive contact conditions, tribotests were run against different abrasive counter bodies. For this, the steel counter bodies were covered with abrasive paper of different graining. The designations of the three applied abrasive papers were: 240 (middle grain size approx. 42–46 µm), 320 (middle grain size approx. 27–30 µm) and 400 (middle grain size approx. 16–18 µm). These abrasive papers will be referred further as abrasive paper 240, 320 and 400, respectively. In Figure 3 both the test principle and the set-up are displayed.

In all tribotests the following parameters were used: surface pressure *p*: 0.5 MPa, running speed *v*: 0.32 m/s, testing period *t*: 60 s.

The experimentally determined results of the abrasion tests are based on the determination of the mass loss over the time. Therefore each sample was weighed before and after the test and from the weight difference the specific wear rate (w_S) was calculated in accordance with Equation (2):

$$w_S = \frac{\Delta m}{L \cdot \rho \cdot F_N} \quad [\mathrm{mm^3/N \cdot m}] \qquad (2)$$

where Δm [g] denotes the mass loss of the test specimen, L [m] is the glide path of the sample on the counter body, ρ [g/mm^3] is the density of the test specimen and F_N [N] is the normal force.

3.5. Wear mechanisms

For examination and qualitative description of the wear mechanisms the surfaces of the tested samples were investigated in scanning electron microscope, (SEM; JSM5400 of Jeol, Tokyo, Japan). Prior to SEM inspections the samples were coated with Au/Pd layer with a sputter machine of Balzers (Lichtenstein).

4. Results of the mechanical and wear tests

4.1. Compression properties

The compression modulus of the vinylester (VE) was determined as the tangent of the initial linear range of the compression stress-strain curve. The yield point is defined as that compression stress where the plastic deformation begins. The compression modulus of the SiC particles was given by the manufacturer.

Table 2. Material parameters, which are used for the simulation

Property/ material	E-modulus [GPa]	Yield stress [MPa]	Grain size [µm]
VE	3.2	132	–
SiC	455	–	3 and 9

4.2. Universal (Martens) hardness values

The computed universal hardness values are depicted in Figure 4. The pure VE resin exhibits a lower universal hardness compared to the SiC modified composite materials, as expected. Furthermore, it can be seen that the universal hardness values with lower test load (100 mN) are higher than with higher ones (1500 mN). It can be traced to the fact that with decreasing test load the relationship between elastic and plastic deformation changes [16]. This means that with the lower test load, the Vickers indenter does not penetrate so deeply into the material, and the rather elastic deformations are strongly influenced by the SiC particles. Therefore the measured values at lower loading exhibit also a higher scatter compared to those measured at high loading. With a higher test load the Vickers indenter penetrates more deeply

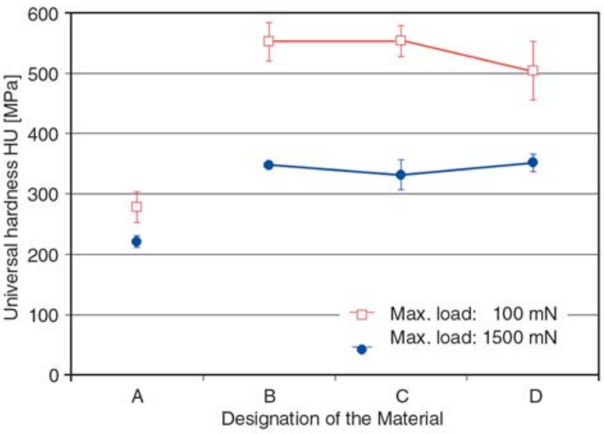

Figure 4. Universal hardness values of the materials

into the material and an integral value for the hardness is determined, which is less influenced by local differences in the material. When higher test load was applied the scatter range was reduced and the measured universal hardness values were very similar to one another for the three different composites. It is recognizable that the two composite materials – B and C – exhibit the same universal hardness (at 100 mN test load). However a lower average universal hardness value was determined for the composite material D.

4.3. Specific wear rates

In Figure 5 the specific wear rates are represented as a function of the SiC particle size for the three abrasive papers of different graining. As expected, the pure VE resin under these test conditions exhibits very high wear rates hence these were not considered in the representation. The wear rate of the pure VE resin was at about 0.5 mm^3/Nm against abrasive paper 320.

Figure 5 shows that the specific wear rate decreases when the grain size of the used abrasive paper decreases. It means that the wear also decreases with sinking abrasiveness of the counter body. The composite material, which contains only 3 µm SiC particles shows under all three conditions the highest wear rates. Interestingly the same specific wear rate was found in the tests run against the two abrasive papers 320 and 400. So it can be concluded that the reduction of abrasiveness between these two graining does not affect any more positively the wear characteristics.

On the other hand the two materials C and D show permanently decreasing wear rates with decreasing abrasiveness of the counter body. Against the roughest abrasive paper 240 the material C shows higher wear values than material D. In case of materials C and D the wear rate values practically coincide with decreasing abrasiveness of the counter body (cf. results against the abrasive paper 400 in Figure 5). The reason of this phenomenon is that the smaller particles (3 µm) can be more easily broken out if the abrasiveness of the counter body is high enough.

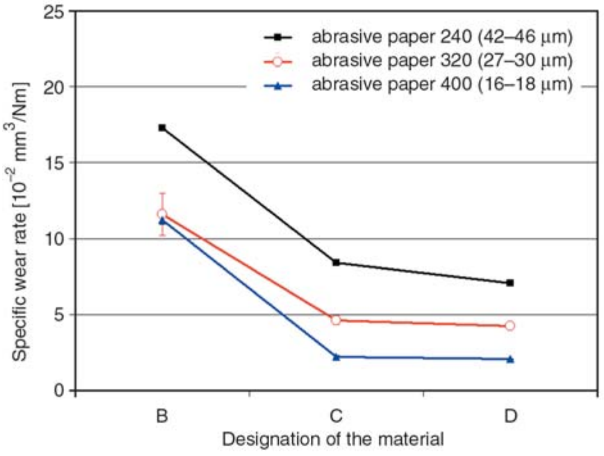

Figure 5. Specific wear rates of the different composites

4.4. Coefficient of friction

During the wear tests the arising friction forces were detected. From this the coefficients of friction (referred further as COF) can be determined as a quotient of the measured friction forces and the applied normal force. The duration of tests was 60 seconds. During the tests first an initial transient tribological process was observed. Due to this the average COF values were determined from the values of the second half of the tests (from $t = 30$ to $t = 60$ seconds), see Figure 6. The COF values of material A aren't considered in the representation. The COF value of material A against abrasive paper 320 was about 0.7.

Figure 6 shows that the three materials (B, C and D) have almost the same COF values independently from the contained grain size of the SiC (at the same abrasiveness of the counter body). Moreover it can be clearly seen that the COF values increase versus the decreasing abrasiveness of the counter body. The rough abrasive paper and the composite glide more easily on each other because the large abrasive particles have small real contact

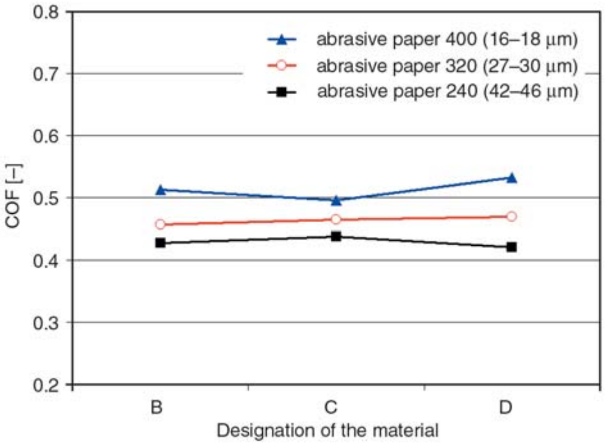

Figure 6. Detected coefficients of friction (COF) values (average values of the last 30 seconds of the tests)

area in the process zone. The real contact area increases with decreasing grain size of the abrasive paper. This causes a more intensive contact between the counter body and the composite material and thus the COF increases. Fact is that the size ratio of the particles in the abrasive paper and in the composites becomes even smaller with decreasing abrasiveness. Due to this the probability of collisions of filler and abrasive particles increases, causing higher COF. This phenomenon is especially dominant for material D.

4.5. Wear mechanisms

The worn surfaces of the samples were analysed with a scanning electron microscope. In Figure 7 one can see the surfaces of the samples, tested against the abrasive paper 240. The wear track caused by the most abrasive paper was analysed, as this yielded to the most prominent wear. The arrow in Figure 7 indicates the sliding direction of the counter body.

The abrasive wear (furrowing and scratching) can be well resolved even at low magnifications (pictures on the left side) in all materials. Material B exhibits strongly fractured surface (cf. Figure 7a). One can observe heavy damages with many small, but relatively broad cracks in the wear track (cf. Figures 7b and 7c). Note that not only the surface, but also the base material under the contact surface was damaged. Due to the severe wear, the surface is covered with wear particles.

At the lowest magnification one can see that material C exhibits a less destructed surface than material B (cf. Figure 7e). Also the other two magnifications of the wear path show fewer damages and cracks (cf. Figures 7f and 7g). The cracking is moderate with some subsurface damage in the material.

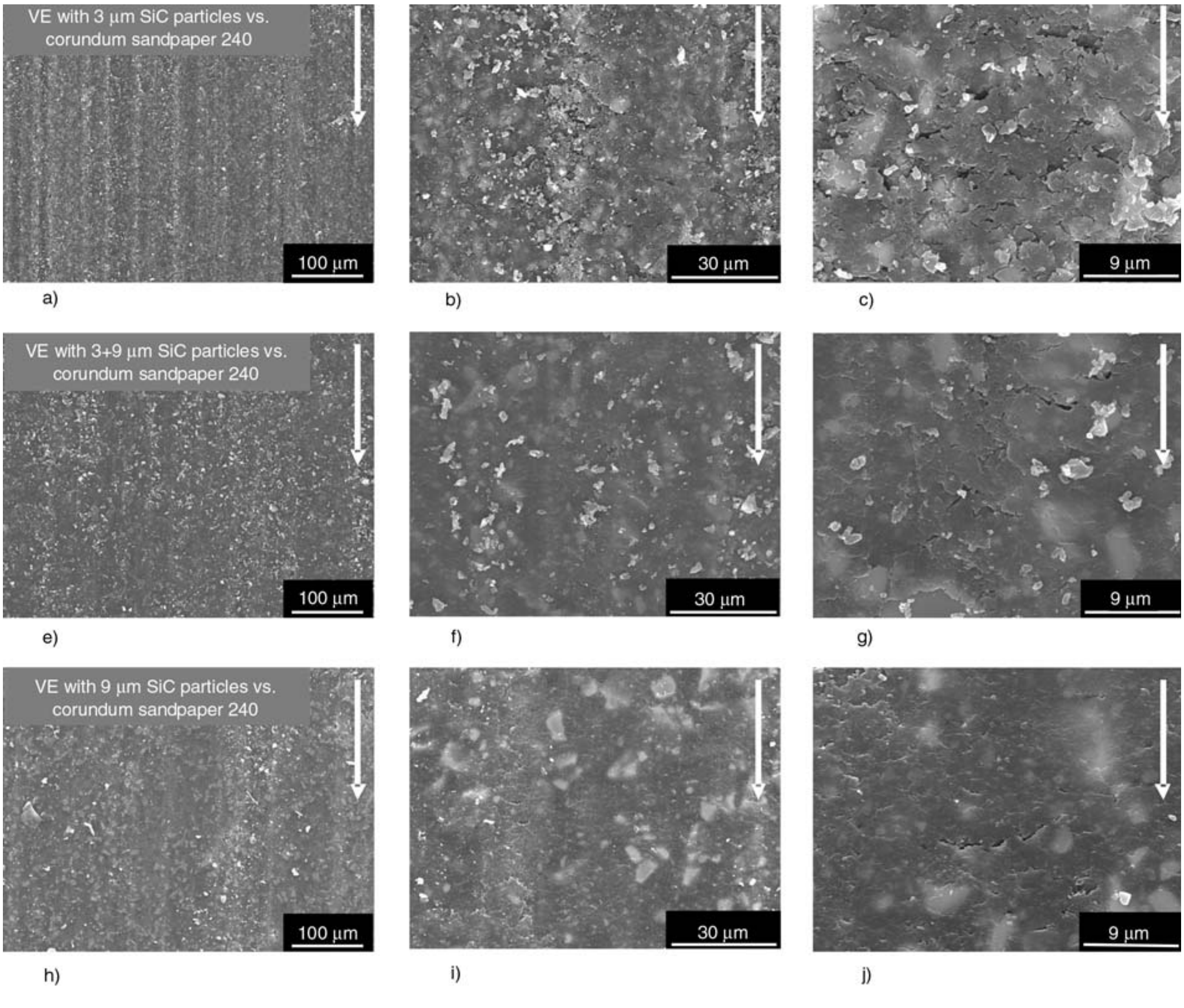

Figure 7. Scanning electron microscopy pictures about the wear tracks of the different composites, material B (a, b and c), material C (e, f and g) and material D (h, i and j). Note: The counter body was in all cases abrasive paper 240 with an average grain size of 42–46 µm.

Wear debris are less on the surface of C than of material B.

The last composite, material D (cf. Figure 7h) suffered obviously the lowest damage and wear during the tribotests. The smallest enlargement shows a raw surface without deep scratching or furrowing. The two other SEM pictures (cf. Figures 7i and 7j) confirm a moderately damaged surface structure. The cracks on the surface seem to be relatively short which are likely not deeply penetrating below the surface.

The universal hardness values of the investigated materials provide no interpretation related to the effect of the filler particle size on the wear characteristics. Therefore we need to find another way to elucidate the mentioned size effect of the filler particles.

We assume that the abrasive roughness peaks and the microindenter should cause similar deformations in the composites, in spite of that the average penetration depth of the abrasive particles and the penetration depth during the microhardness tests are probably different. Therefore to shed light on the size effect of the SiC particles the FE method will be adopted to simulate the stress and strain behaviour of the different composites during microindentation tests.

The micro scaled strain and stress distributions calculated by FE should be in correlation with the observed wear performance of the different composites.

5. Simulation of the micro scaled stress and strain behavior

The Cosmos/M Geostar FE software was used to simulate the micro scaled deformation process during microindentation tests. Microhardness tests with a maximum load of 100 mN were FE modelled. The microhardness tests were carried out using a Vickers diamond indenter. The Vickers indenter is pyramid shaped with a plane angle of 136°. Due to the symmetrical shape of the indenter, one can assume that the loads are distributed equally at all four sides the diamond pyramid during the tests. This assumption makes it possible to reduce the simulation to a quarter model (see Figure 8). Thus the available nodes (approx. 60 000) can be placed denser below the indenter.

The quarter models of the simulations correspond in all three cases to a volume of 200×200×200 μm^3. The models contain in each case 50907 nodes and 59357 elements (Solid elements with 8 nodes). The models are micro models, where the reinforcement particles (SiC) are embedded in the matrix (VE). Both the VE matrix and the SiC particles exhibit their own specific material properties. The material law of the VE matrix is nonlinear. The characteristic values of the materials are summarized in Table 2.

Because the models are built up from cubes of an edge length of 2 μm, the 3 μm SiC particles were implemented as cubes with an edge length of 4μm. The 9 μm SiC particles were modelled as cubes of an edge length of 10 μm. The implementation of the fillers as cubes is probably right, because the SiC particles are of irregular form with sharp edges. A further assumption is that the SiC particles are present homogeneously in the matrix in macro scale, but nevertheless statistically distributed in micro scale. This statistical distribution of the different sized particles is to see in Figure 8, where the FE meshes of the three different materials (B, C and D) are displayed. The SiC particles do not exhibit strictly given structure, but an irregular statistic distribution. Further on we assumed that the SiC particles have perfect adhesion with the matrix.

The penetration of the Vickers indenter into the material will be simulated using the considerations listed above. The influence of the SiC particles being present regarding the resulting stresses (von Mises stress) and strains (equivalent strains) will be calculated and demonstrated. The goal is to clarify the influence of the reinforcement particle size onto the micro scaled deformation behaviour of the matrix. Furthermore to find correlation between the FE calculated stress and strain distributions and between the wear characteristics of the different composites.

By the FE simulations the surface points of the perfectly rigid Vickers indenter were fixed. These fixed points were linked to the surface of the composite materials by contact elements. The non-linear FE calculations were force controlled. The driver force was introduced at the bottom of the quarter models, where a rigid plate was glued to the quarter model (see Figure 8). In the symmetry planes of the quarter models the proper boundary

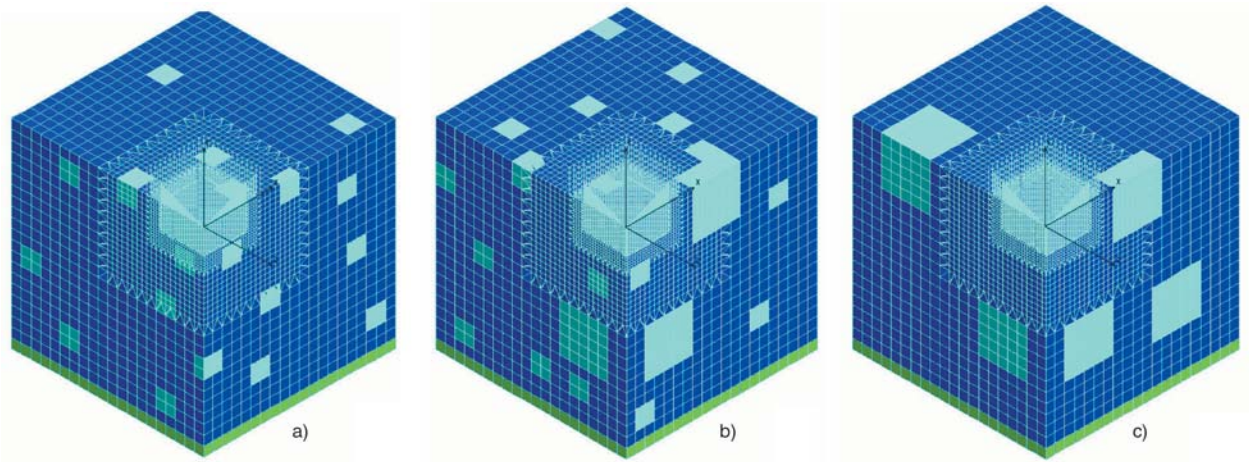

Figure 8. FE meshes for the simulations (VE matrix always with 16 vol% SiC particles): material B (a), material C (b), material D (c)

conditions were applied and the modified Newton-Raphson method was used for the calculations [17].

6. Results of the simulations

The FE-calculated stress and strain distributions are displayed in the Figures 9 to 13. For the better overview in the following figures the embedded SiC particles were not presented. This makes possible to visualize strain peaks and large strains (caused by the particles) in the VE matrix at the indentation zone.

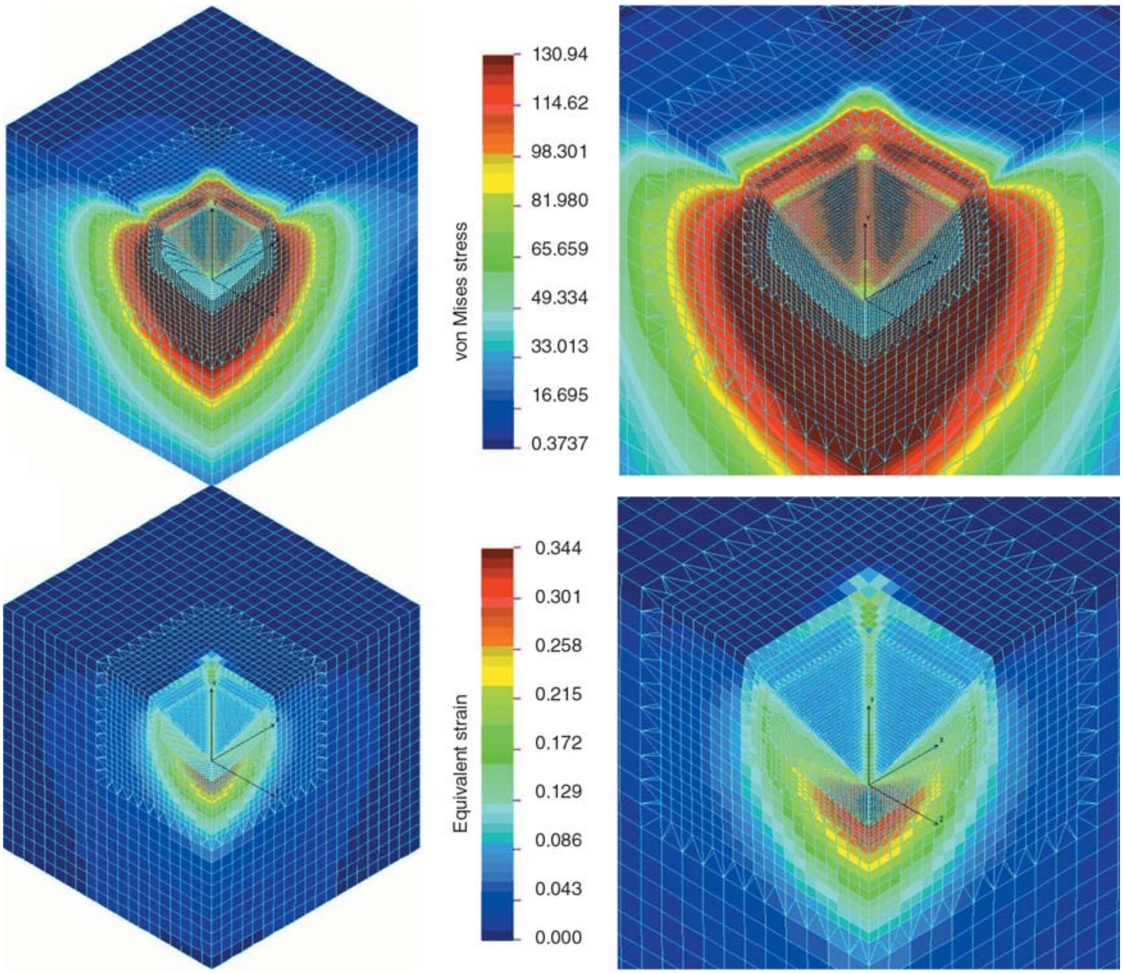

Figure 9. FE-simulation results for the material A (pure VE resin)

6.1. Material A (pure VE resin)

In Figure 9 the von Mises stress and the equivalent strain distribution is displayed in the case of pure VE resin when the maximum normal load of 100 mN is applied. It can be seen that both the arising stresses and the strains concentrate immediately below the indenter. With increasing distance to the contact area, the value of the stress and strain permanently decreases. Altogether a regular stress and strain distribution can be observed in the matrix, similar to a regular Hertzian contact.

6.2. Material B (VE + 16 vol% SiC (3 µm))

Compared to the results of material A, material B shows completely different stress and strain distributions. In Figure 10 one can see that both the von Mises stress- and the equivalent strain-distributions are very strongly affected by the SiC particles in the indentation zone below the indenter. These distributions are not regular any more; they are strongly disturbed by the incorporated particles. Local stress peaks and large strains arise in the indentation zone between the individual particles and the matrix. The location with the highest equivalent strain of 79.5% is hidden in Figure 10 therefore it is displayed in Figure 12 (left) separately. It can be concluded that the small SiC particles change their starting position due to the applied load. Because of it a strongly distorted zone with large strains will be developed at their edges in the VE matrix. The arising maximum equivalent strain is twice as high as it was in the case of the pure VE resin.

6.3.Material C(VE + 8 vol% SiC (3 µm) + 8 vol% SiC (9 µm))

In Figure 11 the simulation results of material C are represented. It can be clearly seen that both the arising stresses and strains are affected considerably by the incorporated particles. Because in Figure 11 the position of the maximum equivalent strain value is not visible, since this is at the corner of a small particle below the surface, this position is separately

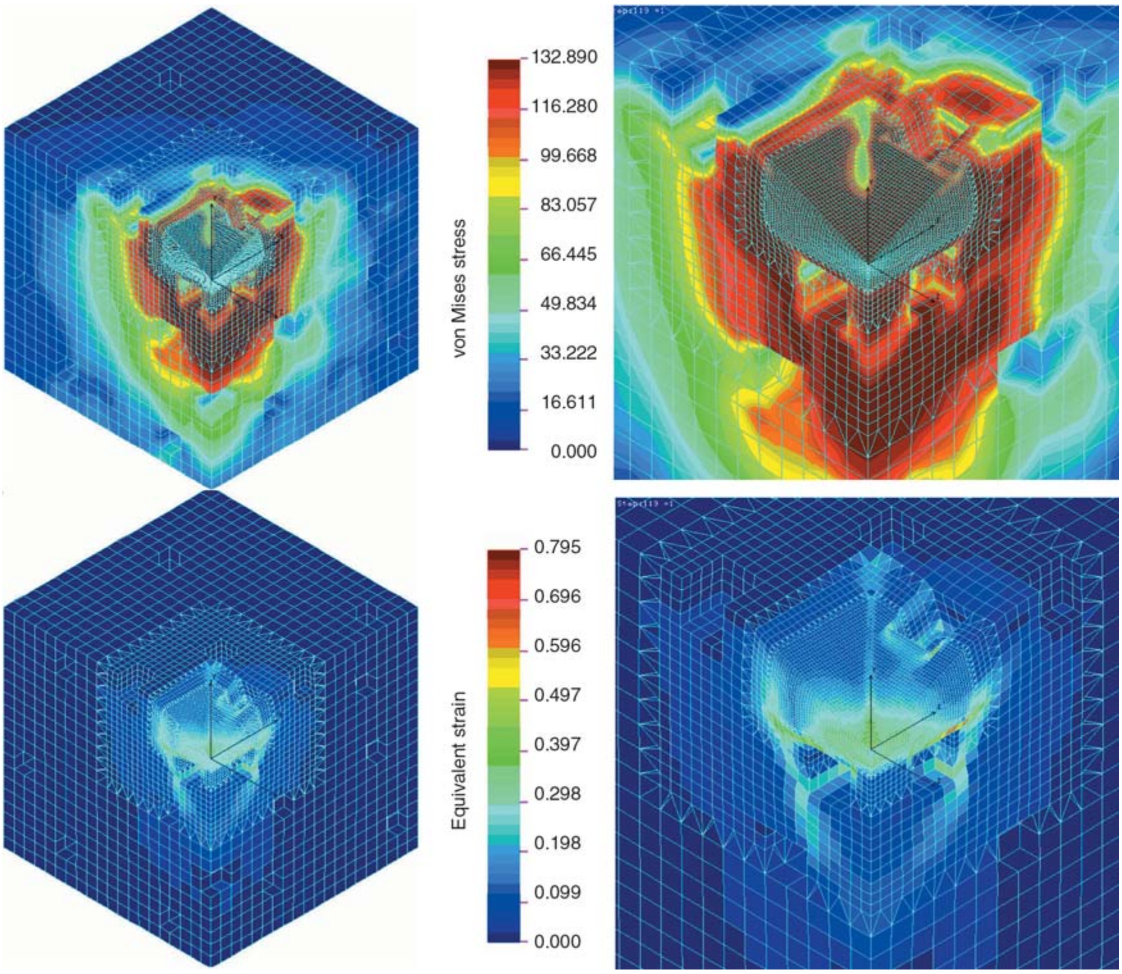

Figure 10. FE-simulation results for the material B (3 µm SiC particles)

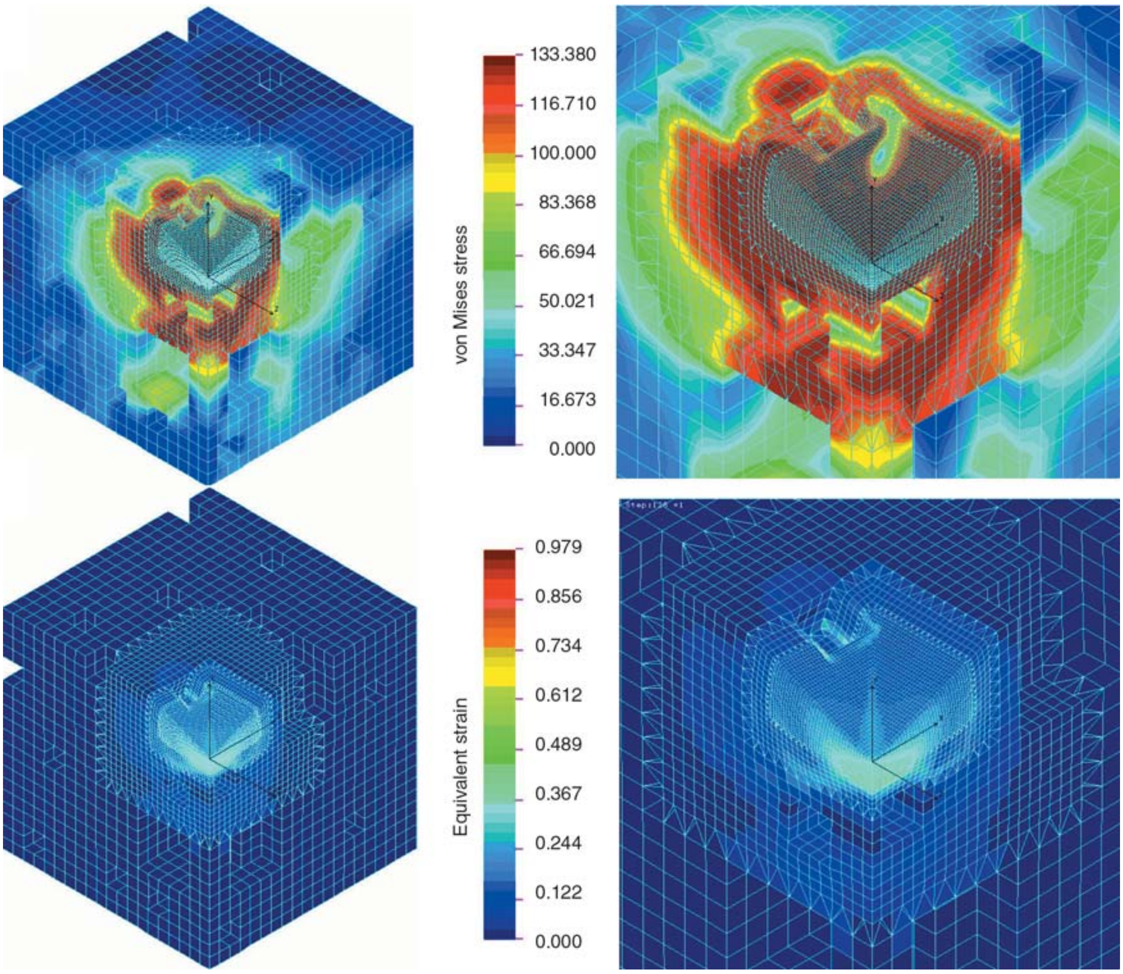

Figure 11. FE-simulation results for the material C with 3 + 9 µm SiC particles

displayed in Figure 12 (right). Observing these results, one can conclude that the matrix can be damaged quickly at the corner of the small (3 µm) particles due to the arising high stresses and strains. In this case the maximum value of the equivalent strain is 97.9%. The general impression refers to an intensely disturbed stress and strain distribution. However thanks to the larger particles (9 µm) the stresses and strains do not extend so deeply into the material, as it was in the case of material B. The reason for it is that larger particles are embedded with a larger surface into the matrix, so their starting position can be hardly changed. Thereby the deeper regions in the matrix are protected. On the other hand in the indentation zone the small (3 µm) SiC particles cause large stresses in the matrix.

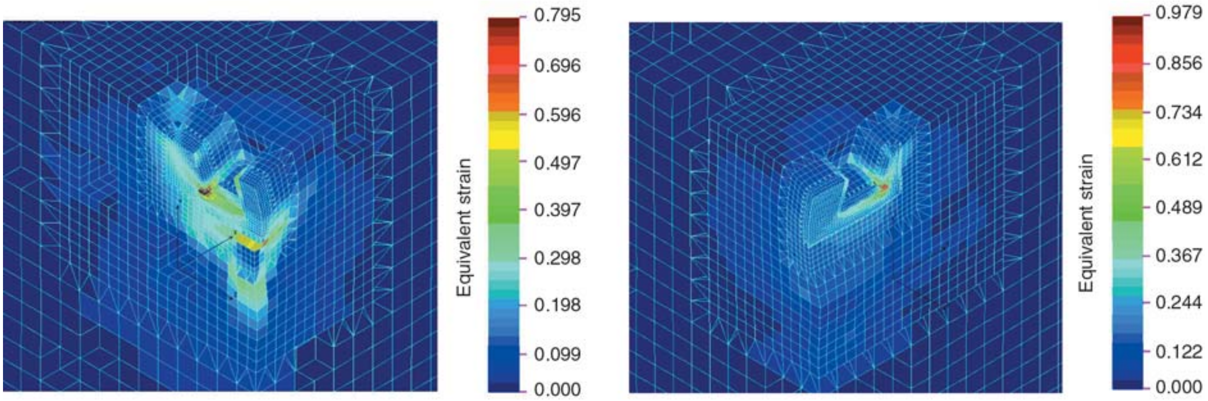

Figure 12. Sectional details of the FE-simulation results of the material B (left) and material C (right)

6.4. Material D (VE + 16 vol% SiC (9 µm))

The von Mises stress- and the equivalent strain-distributions of the material D are displayed in Figure 13. One can see that the maximum von Mises stress reaches its maximum directly underneath the indenter (see Figure 13 right above). The large SiC particles (9 µm) near to the contact zone affect considerably the distribution of the von Mises stress. However it is noticeable in this case that the stress distribution essentially concentrates below the indenter and less interaction takes place with the boundary region of the particles. The maximum equivalent strain arises likewise directly below the indenter. The SiC particles affect the strain distribution only slightly. It means that the deeper regions in the matrix are thereby protected exactly like before by the material C. From these results it can be concluded that the material failure (cracking) arises also only within a relatively small region near to the surface. One can conclude, that the large SiC particles (9 µm) affect the stress and strain distribution positively, constraining the spread of high stresses into a relatively small volume near to the surface. One can see also that the arising maximum value of the equivalent strain is only approximately 20% higher than it was by the material A (pure VE resin).

7. Discussion of the results

The results of the wear experiments show that the difference in the SiC grain size has a relevant influence on the specific wear rates. According to this observation the FE simulations have show that the small SiC particles (3 µm) generate locally larger stresses and strains in the matrix, than the larger ones (9 µm). This can be attributed to the size ratio of the arising contact area below the indenter and the particle size within the matrix. If the size of the contact zone is comparable with the size of the reinforcement particles, then smaller stresses and strains will be developed in the matrix. The reason is that the large particles can localize the stress and strain distribution into a small volume near to the

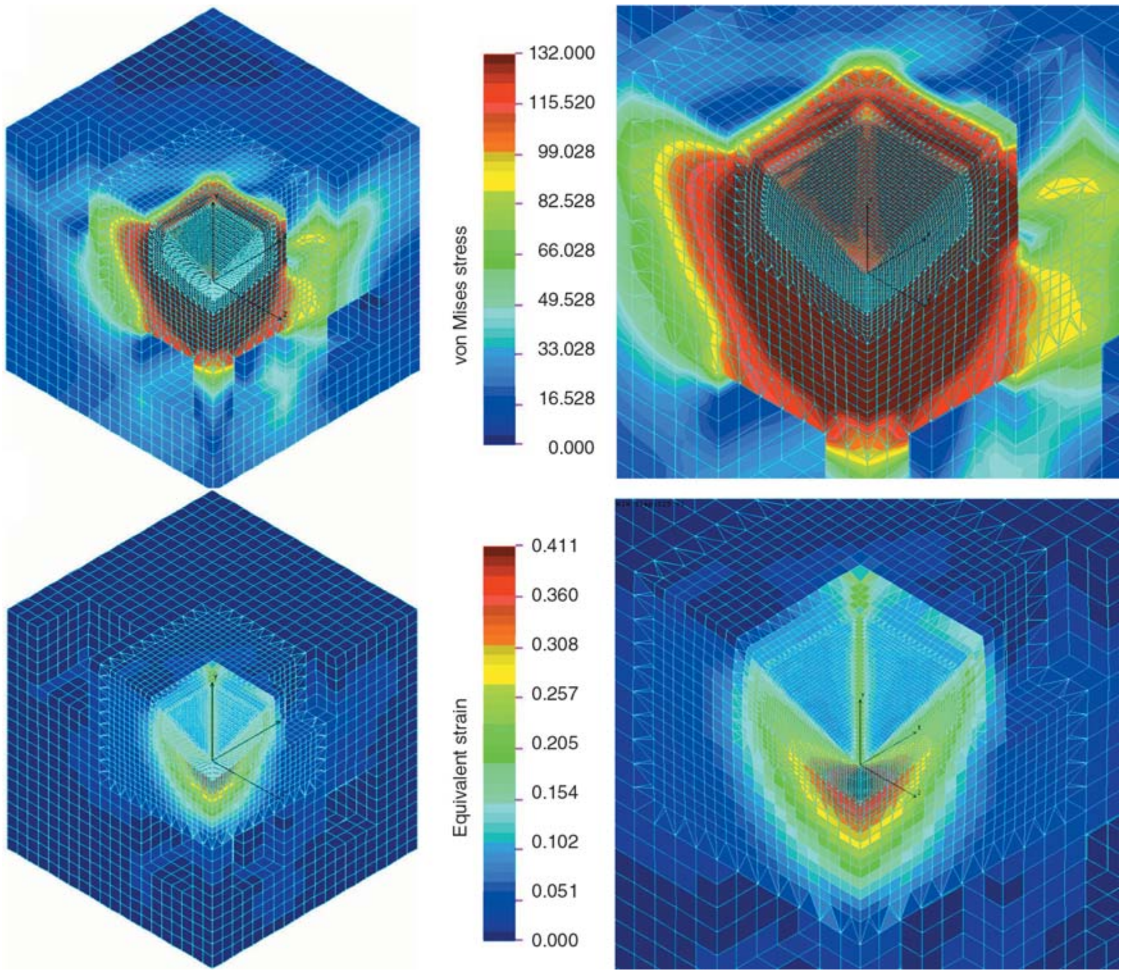

Figure 13. FE-simulation results for the composite D material with 9 µm SiC particles

surface. In contrast to it the small SiC particles in the indentation zone will change strongly their geometrical position in the matrix due to the load of the indenter. Because of it the matrix in the environment of the small particles is strongly stressed and distorted which causes material damage. Therefore the ideal composite material for abrasive wear conditions needs to contain an appropriate size distribution of the reinforcement materials.

Further on based on the simulation results it can be explained why the specific wear values of material C and D will be nearly identical with decreasing abrasiveness. By the presence of large SiC particles the strain distribution is obstructed and the damage of the matrix below the indentation zone is moderated. Because proportionately less large particles are present in the material C, the effect of these particles comes only with decreasing abrasiveness to the fore. Finally against abrasive paper 400 the abrasiveness of the counter body becomes so small (see chapter 3.4), that the tests provide nearly identical wear values by both composite materials (C and D).

It can be noted that the experimentally determined specific wear rates and the FE simulation results show the same tendencies. The FE results were correlated also with the observed wear mechanisms of the composites, related to the density and depth of the surface cracking.

As it was mentioned before the average depth of the penetrations due to the abrasion and the penetration depth during the microhardness tests are not identical. Even so the results and the tendencies show that the above mentioned phenomenon (i.e. the size proportion of the reinforcement particles and the abrasive roughness peaks) is of basic importance.

8. Conclusions

This work has shown that there is no trivial connection between the experimentally determined universal hardness of the investigated materials and their wear performance. On the other hand the FE simulations have highlighted that the arising stress and strain distributions in the VE matrix during the microindentation process can be correlated with the abrasive wear characteristics.

FE results indicated that the size of the reinforcement particles should be comparable with that of the roughness peaks of the abrasive paper to achieve low wear.

We can assume that the interfacial bonding strength between the matrix and the SiC particles is similar, independently from the particle size. Accordingly the resistance to change their geometrical position increases with increasing particle size. Thus larger reinforcement particles can withstand larger deformations, i.e. stronger roughness peaks, thereby protecting the base material.

Otherwise the wear resistance of a particle filled composite could be enhanced also by the improvement of the interfacial bonding strength between the particles and the matrix [18]. Further on it is necessary to note that the shape of the reinforcement particles is also extremely important in the view point of the material strength, which is influencing also the wear performance [19].

Finally we think that the following observations could refer to a connection between the universal hardness and measured COF values. It was found that the microindentation tests provide smaller universal hardness values when higher loads are applied as well as lower COF is to measure against strongly abrasive surfaces. However, this assumed correlation was not checked within this study.

References

[1] Tewari U. S., Bijwe J., Mathur J. N., Sharma I.: Studies on abrasive wear of carbon fibre (short) reinforced polyamide composites. Tribology International, **25**, 53–60 (1992).

[2] Harsha A. P., Tewari U. S.: The effect of fibre reinforcement and solid lubricants on abrasive wear behaviour of polyetherketone composites. Journal of Reinforced Plastics and Composites, **22**, 751–767 (2003).

[3] Briscoe B. J., Evanst P. D., Lancaster J. K.: Single point deformation and abrasion of γ-irradiated poly(tetrafluoroethylene). Journal of Physics D: Applied Physics, **20**, 346–353 (1987).

[4] Czichos H., Habig K-H.: Tribologie Handbuch- Reibung und Verschleiß. Vieweg, Braunschweig (1992).

[5] Friedrich K.: Friction and wear of polymer composites. Elsevier, Amsterdam (1986).

[6] Fischer A.: Warmverschleiß durch körnige Medien. in 'Reibung und Verschleiß von Werkstoffen, Bauteilen und Konstruktionen; Tribologische Optimierung und Schadensbekämpfung. Kontakt und Studium' (eds: Mettner M., Wippler E.) Expert Verlag, Renningen, 141–153 (2004).

[7] Roberts S.: Surface engineering- Foliensammlung, http://www.surface-engineering.com (24.06.2006).

[8] Uetz H., Wiedemeyer J.: Tribologie der Polymere. Hanser Verlag, München (1984).

[9] Oster F., Schlarb A. K.: Hochtemperaturbeständige Polymer-Beschichtungen für tribologische Anwendungen. IVW GmbH, Kaiserslautern (2005).

[10] Váradi K., Felhős D., Friedrich K., Tsotra P.: Experimental and FE analysis of the failure behaviour of SIC/epoxy functionally graded rings under compression load. in '1st Vienna International Conference of Micro- and Nano-Technology, Vienna, Austria' 431–440 (2005).

[11] Tsotra P., Friedrich K., Felhős D., Váradi K.: Compression of homogeneous and graded sic/ep rings experimental results and FE modelling. Journal of Materials Science, **41**, 3349–3355 (2006).

[12] Prehn R., Haupert F., Friedrich K.: Polymere Verbundwerkstoff-Gleitlager für aggressive und abrasive Medien. Tribologie und Schmierungstechnik, **53**, 10–15 (2006).

[13] Felhős D., Váradi K., Friedrich K.: FE modeling of a roller with functionally graded material structure(in Hungarian). Műanyagipari Szemle, **4**, 81–89 (2005).

[14] Felhős D., Váradi K., Friedrich K.: Wear analysis of functionally gradient composite materials by FE modeling of microhardness measurements and wear tests. Materials Science Forum, **537–538**, 519–525 (2006).

[15] Felhős D., Váradi K., Tsotra P., Friedrich K.: Microhardness test of graded SiC/EP rings: Experimental results and FE modelling. Journal of Computational and Applied Mechanics, **6**, 207–218 (2005).

[16] Domke W.: Werkstoffkunde und Werkstoffprüfung 10. Cornelsen-Velhagen und Klasing, Bielefeld (1986).

[17] Lyness J. F., Owen D. R. J., Zienkiewicz O. C.: The finite element analysis of engineering systems governed by a non-linear quasi-harmonic equation. Computers and Structures, **5**, 65–79 (1975).

[18] Zhang X. R., Zhao P., Pei X. Q., Wang Q. H., Jia Q.: Flexural strength and tribological properties of rare earth treated short carbon fiber/polyimide composites. Express Polymer Letters, **1**, 667–672 (2007).

[19] Vas L. M., Pölöskei K., Felhős D., Deák T., Czigány T.: Theoretical and experimental study of the effect of fiber heads on the mechanical properties of non-continuous basalt fiber reinforced composites. Express Polymer Letters, **1**, 109–121 (2007).

eXPRESS Polymer Letters Vol.2, No.10 (2008) 718–726
Available online at www.expresspolymlett.com
DOI: 10.3144/expresspolymlett.2008.85

Dielectric behaviour and functionality of polymer matrix – ceramic $BaTiO_3$ composites

A. Patsidis, G. C. Psarras*

Department of Materials Science, School of Natural Sciences, University of Patras, Patras 26504, Greece

Received 17 July 2008; accepted in revised form 4 September 2008

Abstract. Dielectric properties of polymer matrix – ceramic $BaTiO_3$ composites were examined by means of Broadband Dielectric Spectroscopy (BDS) in the frequency range of 10^{-1}–10^7 Hz and over the temperature range of 30–160°C, varying the content of ferroelectric particles. Experimental results provide evidence that the recorded relaxation phenomena include contributions from both the polymeric matrix and the presence of the reinforcing phase. Obtained results are analysed via the electric modulus formalism. Polymer matrix exhibits two distinct relaxation processes attributed, with ascending relaxation rate, to glass/rubber transition, and local motions of polar side groups. Interfacial polarization or Maxwell-Wagner-Sillars process is present in the low frequency range and at high temperatures. Finally, in the vicinity of the characteristic Curie temperature (T_C) an abrupt variation of the real part of dielectric permittivity with temperature is recorded. This peak is probably related to the ferroelectric to paraelectric phase transition of the employed ceramic inclusions.

Keywords: *polymer composites, dielectric spectroscopy, smart materials, ceramic $BaTiO_3$, ferroelectrics*

1. Introduction

Ceramic-polymer composites consisting of ferroelectric crystal particles, homogeneously distributed, in an amorphous host represent a novel class of materials, with several interesting properties [1–4]. High tech electronic devices require new high dielectric permittivity materials (known as high-K materials), which combine at the same time, suitable dielectric properties, mechanical strength and ease processing. Recently, ceramic-polymer composites have been studied in various applications including integrated capacitors, acoustic emission sensors and for the reduction of leakage currents [5–10].

Many polymers have been proved suitable matrices in the development of composite structures due to their ease production and processing, good adhesion with reinforcing elements, resistance to corrosive environment, light weight and in some cases ductile mechanical performance. Further, polymers are basically electrical insulators with low dielectric permittivity and often high dielectric strength. On the other hand, ceramic particles are brittle materials, with high dielectric permittivity and thermal strength. Combining two materials with deviating properties in a new composite structure, could lead in a materials system with superior performance. Furthermore, if the embedded ceramic particles are ferroeletric, functional or self-tunable properties can be disclosed to the composite structure. Ferroelectric materials exhibit spontaneous polarization and are characterized by a temperature dependent disorder to order transition. The electrical response of polymer matrix particulate composites depends on various factors such as the permittivity and conductivity of the constituent

---

*Corresponding author, e-mail: G.C.Psarras@upatras.gr phases, the size, shape and volume fraction of the filler and the type of distribution of the inclusions.

In the present study composite systems of epoxy resin and ceramic $BaTiO_3$ particles have been prepared, varying the volume fraction of the inclusions. The dielectric response of the composites was studied in a wide frequency and temperature range by means of Broadband Dielectric Spectroscopy (BDS). Experimental data were analyzed by means of dielectric permittivity and electric modulus formalisms [11–13]. From the conducted analysis arises, that the recorded dielectric relaxations are related to both the polymer matrix and the presence of the reinforcing phase. Finally, the electrical response of ferroelectric particles – polymer matrix composites is influenced by the ferroeletric to paraelectric transition of the inclusions.

2. Experimental

2.1. Samples preparation

Commercially available low viscosity epoxy resin (Epoxol 2004A, Neotex S.A., Athens, Greece) was used as a prepolymer. The employed curing agent (Epoxol 2004B) operating at a slow rate was supplied by the same company also. Barium titanate was purchased from Sigma-Aldrich. The mean particle diameter was less than 2 μm. The followed procedure includes mixing of the resin with the curing agent in a 2:1 (w/w) ratio. While the above systems were still in the liquid state, various amounts of the ceramic powder were added for the production of the composite samples. Stirring at a low rate and degassing the mixture in vacuum-oven were also included in the preparation process. The initial curing took place at ambient for a week, followed by post-curing at 100°C for 4 hours. Finally, specimens' morphology was checked for voids and extensive clusters by means of Scanning Electron Microscopy (Leo Supra 35VP). In all samples the distribution of the filler is characterized as satisfactorily and more or less homogeneous, Figure 1.

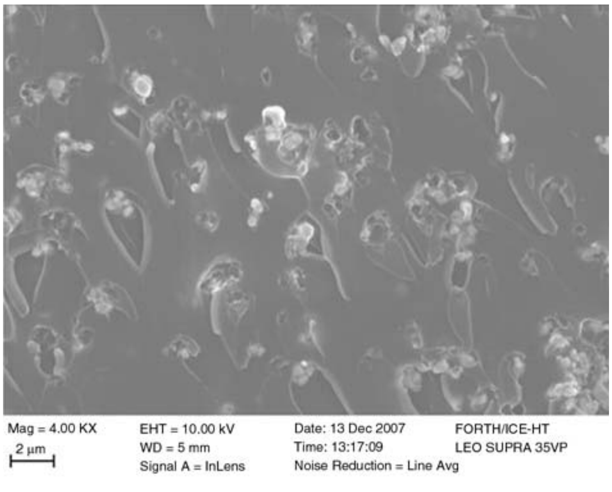

Figure 1. Scanning Electron Microscopy image of fractured surface of the specimen with 20 phr in $BaTiO_3$ content

2.2. Thermal characterisation

A Diamond (Perkin Elmer, Shelton, USA) differential scanning calorimeter operating at a scan rate of 10°C/min was used to characterise thermal transitions of the employed epoxy resin and the produced composites. Samples were placed in an aluminum crucible and an empty aluminum crucible was serving as reference. Temperature was varied from ambient to 200°C.

2.3. Dielectric measurements

The electrical characterization of the composites was conducted by means of Broadband Dielectric Spectroscopy (BDS) in the frequency range of 0.1 Hz to 10 MHz, using Alpha-N Frequency Response Analyser, supplied by Novocontrol Technologies (Hundsagen, Germany). The dielectric cell was a three terminal guarded system constructed according to the ASTM D150 specifications. Samples were placed between metal electrodes and problems arising from possible electrode polarisation were excluded by employing the electric modulus formalism [11–13]. Isothermal frequency scans were conducted, for each of examined specimens, from ambient to 160°C with a temperature step of 10°C. The amplitude of the applied voltage was 1000 mV.

3. Results and discussion

The DSC thermographs for all the tested specimens were analyzed by employing suitable software supplied by Perkin Elmer. Glass transition temperature (T_g) was determined via the point of inflection of the transition. The determined values are listed in Table 1. Electrical relaxation effects in polymer matrix composites arise from interfacial effects, phase transitions and polarization or conductivity mechanisms. The recorded dielectric data, of all the

Table 1. Concentration of $BaTiO_3$ particles in all the examined systems and the corresponding glass transition temperatures

Sample	Volume fraction of $BaTiO_3$ [%]	Glass transition temperature, T_g [°C]
Epoxy	0	56.6
Epoxy + 10 phr $BaTiO_3$	2.71	58.9
Epoxy + 20 phr $BaTiO_3$	4.81	59.3
Epoxy + 40 phr $BaTiO_3$	11.46	62.3
Epoxy + 50 phr $BaTiO_3$	13.62	64.0

examined specimens, were first expressed in terms of real and imaginary part of permittivity and then transformed, via Equation (1), to the electric modulus formalism. Arguments for the resulting benefits of the electric modulus presentation have been exhibited and discussed elsewhere [11–13]. Electric modulus is defined as the inverse quantity of complex permittivity by the Equation (1):

$$M^* = \frac{1}{\varepsilon^*} = \frac{1}{\varepsilon' - j\varepsilon''} = \frac{\varepsilon'}{\varepsilon'^2 + \varepsilon''^2} + j\frac{\varepsilon''}{\varepsilon'^2 + \varepsilon''^2} = M' + jM'' \qquad (1)$$

where ε', M' are the real and ε'', M'' the imaginary parts of dielectric permittivity and electric modulus respectively. The frequency dependence of the real part of electric modulus (M') for the composites with 10, 20 and 50 phr in $BaTiO_3$ particles, at temperatures varying from 30 to 160°C, is shown in Figures 2a, 3a and 4a. The existence of a step-like transition from low to high values of (M') is evident in all specimens, at temperatures higher than 50°C. The recorded transitions imply the presence of a relaxation process, which should be accompanied by a loss peak in the diagrams of the imaginary part of electric modulus (M'') versus frequency. As it can be seen in Figures 2b, 3b and 4b loss peaks are clearly formed in the frequency range where transitions occur. Relaxation peaks shift to higher frequencies with the increase of temperature. The shape and magnitude of the formed peaks remain more or less constant in the range of 50 to 100°C. At temperatures higher than 100°C a reduction of the peak shift rate is observed, which is accompanied with an increment of the (M'') maxima. Above 120°C and in the low frequency region an additional peak is recorded. Finally, in the high frequency edge a tendency for the formation of a third relaxation peak is present. In order of increasing frequency, at constant temperature, the recorded loss peaks can be assigned to Interfacial Polarization (IP) known also as Maxwell-Wagner-Sillars (MWS) effect, glass/rubber transition (α-mode) and to local rearrangement of polar side groups of the polymer chain (β-mode). Attributing dielectric peaks to specific relaxation mechanisms is not an easy procedure, which cannot be carried out by simple observing the isothermal plots of Figures 2–4. In Figure 5 comparative plots of the real and imaginary part of electric modulus versus frequency, for all the examined composites, at constant temperature (T = 150°C) are shown. Two relaxation processes, located in the low and inter-

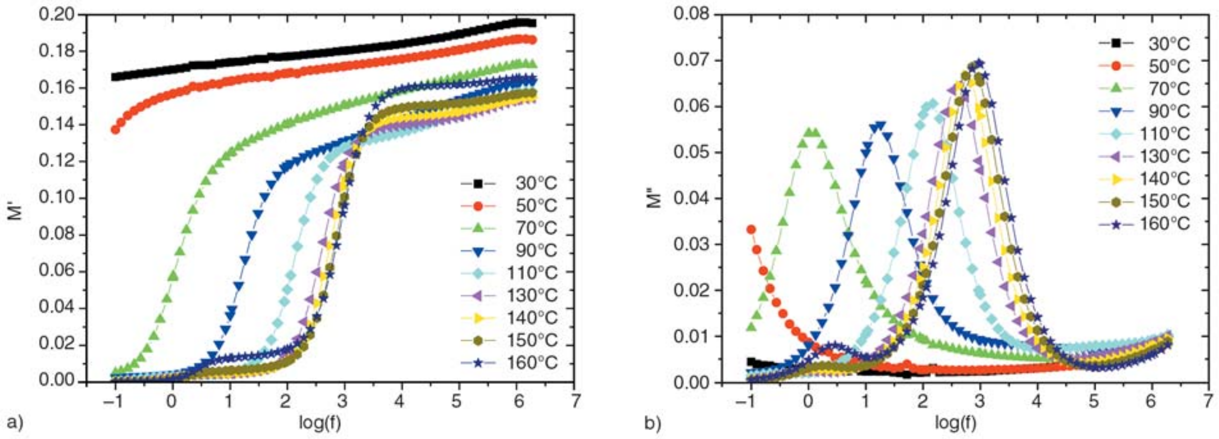

Figure 2. Real (a) and imaginary (b) part of electric modulus vs. frequency for the specimen with 10 phr in $BaTiO_3$ content

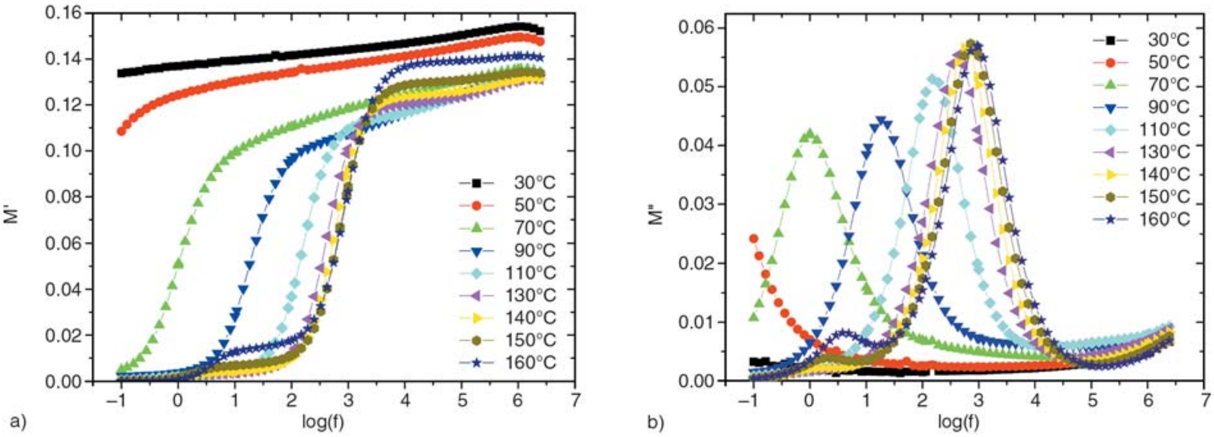

Figure 3. Real (a) and imaginary (b) part of electric modulus vs. frequency for the specimen with 20 phr in $BaTiO_3$ content

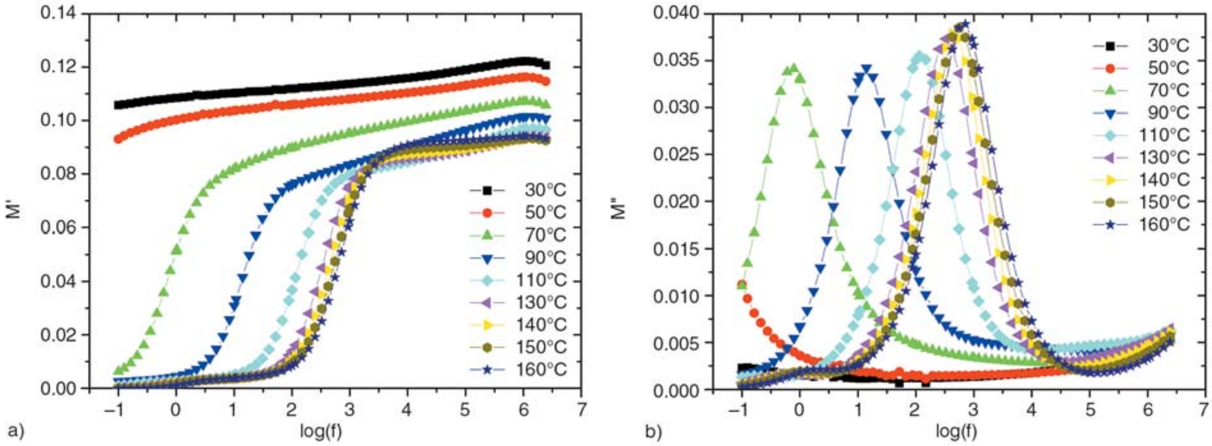

Figure 4. Real (a) and imaginary (b) part of electric modulus vs. frequency for the specimen with 50 phr in $BaTiO_3$ content

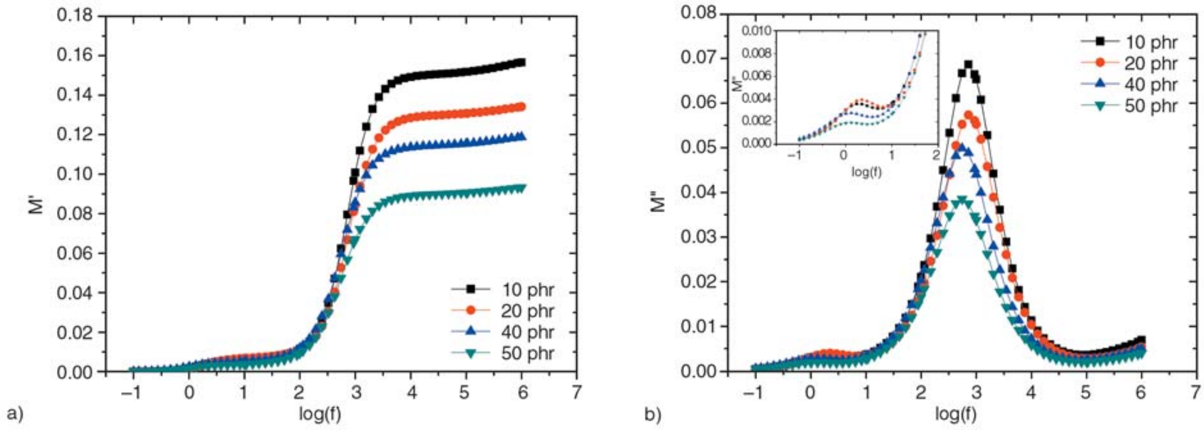

Figure 5. Real (a) and imaginary (b) part of electric modulus vs. frequency for all tested specimens at 150°C

mediate frequency range, are clearly recorded. Increase of the $BaTiO_3$ content results in lower values of M', implying that the real part of dielectric permittivity increases with ceramic filler. It is interesting to note that the more intense relaxation peak, occurring in the intermediate frequency region, appears to be dependent on the $BaTiO_3$ content. Its loss maxima diminish monotonically with filler concentration. In Figure 6, Cole-Cole plots of all composite specimens, at $T = 150°C$, are depicted. In the Cole-Cole presentation relaxation mechanisms become evident via the formation of com-

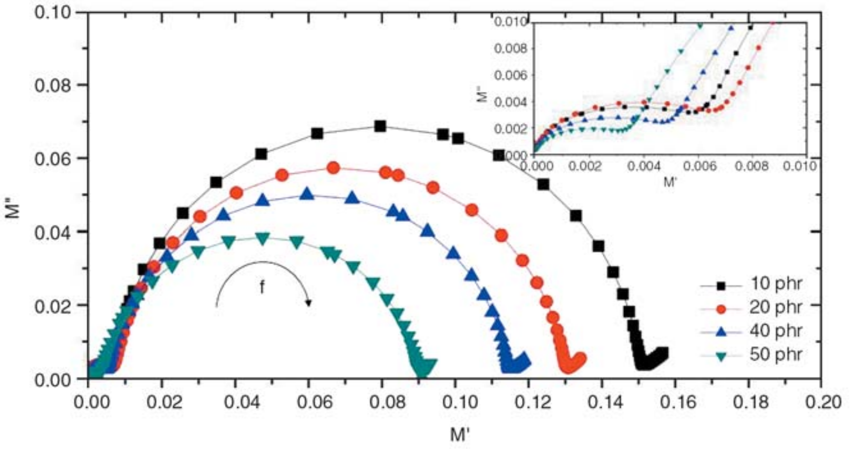

Figure 6. Cole-Cole plots for all tested specimens at 150°C

pleted or even uncompleted semicircles. In our case two distinct semicircles are clearly formed, while in the high frequency edge a tendency for the formation of a third semicircle is present. In the low frequency range the trace of dielectric data forms a small semicircle, the beginning of which coincides with the origin of the graph. So, it can be concluded that no other process, slower than this, is present in the examined composite systems.

It is well known [14–16] that MWS effect appears in complex systems exhibiting electrical heterogeneity, due to the accumulation of charges at the interfaces of the system. Dielectric permittivity of $BaTiO_3$ is remarkably higher than that of epoxy resin. Thus unbounded charges, arising from the stage of specimens' preparation, form large dipoles at the polymer matrix – ceramic inclusions interface. The induced dipoles encounter difficulties to follow the alternation of the electric field and thus the resulting relaxation process occurs in the low frequency region and at high temperatures, being the slowest from all the recorded processes.

α-relaxation process is associated with glass to rubber transition. If sufficient thermal energy is provided to the polymer, then large parts of amorphous macromolecular chains can relax simultaneously in a cooperative motion. The whole process is characterized by glass transition temperature (T_g), which is considered as the temperature where transition occurs. In polymer matrix composite systems, glass transition is related to the chemical structure of the polymer chains and in many cases to the type of the employed filler. As a rule of thumb, glass transition temperature is taken as the temperature at which the α-relaxation loss peak is recorded in the dielectric spectrum at constant frequency equal to 0.1 Hz [15, 17–19]. In Figure 7 loss modulus index (M'') as a function of temperature, at constant frequency, for all the examined systems is presented. It is interesting to note that the intensive peak which is present

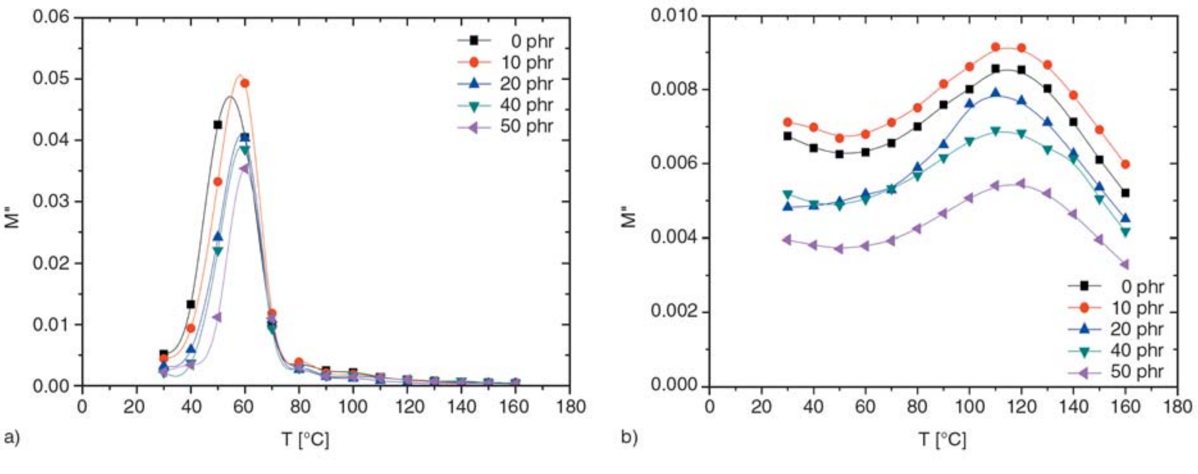

Figure 7. Imaginary part of electric modulus as a function of temperature, for all the tested specimens, at (a) $f = 0.1$ Hz and (b) $f = 1$ MHz

in all specimens and is recorded in the intermediate frequency range (Figures 2–4) is now located at 60°C, when $f = 0.1$ Hz, Figure 7a. This value is very close to the glass transition temperature of the polymer matrix, as determined via DSC measurements, Table 1. Thus it is reasonable to suggest that the relatively slow dielectric relaxation process recorded in the medium frequency range of dielectric spectra corresponds to glass/rubber transition. The evolution of the α-mode peak with temperature becomes evident with the shift of loss maxima to higher frequencies, Figures 2–4. Recalling Figure 5b, the concentration of $BaTiO_3$ particles influences a systematic variation of the α-mode loss maximum. The intensity of the peak diminishes with the increase of $BaTiO_3$ particles and at the same time slightly shifts to lower frequencies at the higher concentrations. From the definition of electric modulus, Equation (1), decreasing values of (M'') correspond to enhanced values of dielectric loss index (ε'') and thus, to more pronounced relaxation phenomena. Increased values of dielectric loss signify that the relative effect consumes more energy. In addition the peak shift rate of the same process, in the loss modulus vs. frequency graphs (Figures 2–4), reduces at temperatures higher than 100°C. The above remarks indicate that the kinetics of α-relaxation process is modified by the amount of ceramic particles and in particular the whole process becomes slower as the amount of ceramic filler increases. Glass transition temperature is expected to increase slightly with $BaTiO_3$ content. Variations between glass transition temperature (T_g) of bulk polymer and thin polymer films on a ceramic substrate or polymer nanocomposites with ceramic inclusions have already been observed and reported [20–22]. These variations have been attributed to interactions occurring between the polymer and the nanoinclusions or substrate. The length scale of the ceramic constituent (from substrate to nanoinclusions) is highly diverging, starting from nanometers and reaching millimeters or even centimeters. If polymer/ceramic interactions are able to appear in these two diverging edges of length scale, then it is reasonable to suggest that the same type interactions could occur at the intermediate level of micrometers. However, these initial indications should be further confirmed by additional experimental work, which should be carried out in the near future.

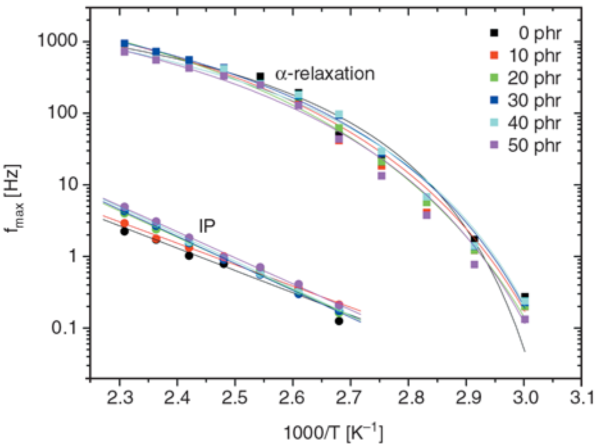

Figure 8. Loss peak position as a function of the reciprocal temperature for the MWS and α-relaxation processes, for all the examined systems

In the high frequency edge all specimens exhibit a tendency for the formation of an extra loss peak, Figures 2–6. This process, which is the faster from all the recorded mechanisms, can be seen only at high frequencies. In Figure 7b, at constant frequency of 1 MHz, a broad peak can be observed, which is attributed to local motions of polymer's polar side groups (β-mode).

The temperature dependence of the loss peaks positions, for both IP and α process is depicted in Figure 8. As it can be seen interfacial polarization follows the Arrhenious type temperature dependence, which is described by Equation (2):

$$f_{\max} = f_0 \exp\left(-\frac{E_A}{k_B T}\right) \tag{2}$$

where E_A is the activation energy, f_0 pre-exponential factor and k_B the Boltzmann constant.

On the other hand α-mode can be described by means of Vogel-Fulcher-Tamann equation, which considers that relaxation rate increases rapidly at lower temperatures because of the reduction of free volume, as expressed by Equation (3):

$$f_{\max} = f_0 \exp\left(-\frac{AT_0}{T - T_0}\right) \tag{3}$$

where f_0 is a pre-exponential factor, A a constant (being a measure of the activation energy), and T_0 Vogel temperature or ideal glass transition temperature. Activation energy calculated via linear regression of Equation (2), as well as all fitted parameters of Equation (3), for each of the tested

Table 2. Values of activation energy, calculated via Equation (2), for the IP process, and fitting parameters of Equation (3) for α-mode

Sample	α-mode		IP/E_A [eV]
	T_0 [K]	A [K^{-1}]	
Epoxy	284	293	0.612
Epoxy + 10 phr $BaTiO_3$	285	518	0.592
Epoxy + 20 phr $BaTiO_3$	287	600	0.727
Epoxy + 40 phr $BaTiO_3$	298	390	0.750
Epoxy + 50 phr $BaTiO_3$	302	478	0.753

samples are listed in Table 2. Activation energy of the IP (MWS) process increases with the content of $BaTiO_3$ denoting the increase of heterogeneity. The parameter T_0 increases also with the filler content, being in accordance with the experimentally determined values of glass transition temperature.

The real part of dielectric permittivity (ε′) vs. temperature, at constant frequency $f = 10$ Hz, is depicted in Figure 9. The variation of permittivity with temperature becomes significant in the range of 110–140°C. At lower temperatures (ε′) attains rather constant values, while at temperatures higher than 100°C increases rapidly (up to 18 times) with temperature and composition showing a maximum at ~140°C and then vanishes. Pure epoxy and the composite system with the maximum employed content in $BaTiO_3$ (50 phr) do not exhibit a peak. The relatively high values of pure epoxy sample in the high temperature region could be attributed to a weak MWS effect (since Interfacial Polarization is almost always present in polymers due to additives, plasticizers etc) and to the possible occurrence of electrode polarization. It is well known [23] from dielectric theory that polarization is proportional to the real part of dielectric permittivity (ε′). Thus any variations occurring in (ε′) spectrum, reflects changes in the polarization of the composite system. At this temperature range the increase of (ε′) is attributed to the enhanced mobility of large parts of the polymer chains and to the co-operating contribution of IP effect in the composite systems. However, the superposition of these two effects cannot explain the formation of the peaks.

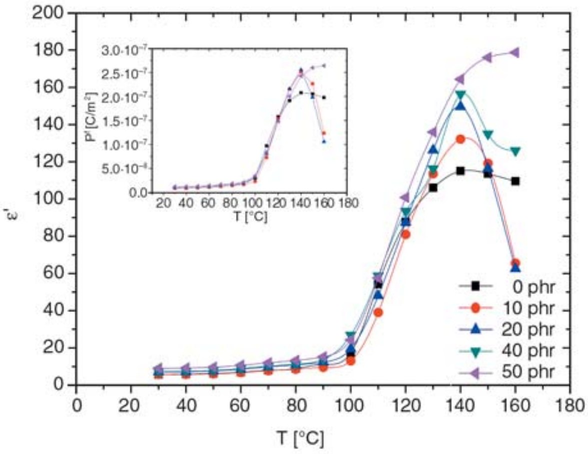

Figure 9. The real part of dielectric permittivity as a function of temperature, for all the tested specimens, at $f = 10$Hz. Inset depicts the corresponding variation of polarization.

On the other hand $BaTiO_3$ is a typical ferroelectric material, exhibiting a ferroelectric to paraelectric phase transition at the characteristic temperature of ~140°C [24], which is known as Curie temperature (T_C). Below T_C, $BaTiO_3$ is consisted by domains showing spontaneous polarization, due to the lower symmetry of the crystal unit cell (tetragonal) in comparison to the unit cell in the paraelectric phase (cubic). In the present study the employed filler is polycrystalline $BaTiO_3$ and is composed by a large number of grains and domains with different orientation. Under the influence of the electric field the dipole moment, at least of a part, of these domains will be able to follow the applied field contributing to the overall polarization of the system. However, as the temperature is approaching T_C a disorder to order transition takes place in the crystal structure of ceramic filler, which becomes evident through the formed peaks in Figure 9. In the paraelectric phase $BaTiO_3$ does not exhibit spontaneous polarization and thus a decrease in the real part of dielectric permittivity occurs. This transition is referred as first order phase transition [24, 25] and characterized by the appearance of local maxima in some physical properties, as a function of temperature, in ferroelectric materials.

Since the applied electric field is low, it is reasonable to expect [26] a linear relation between the achieved polarization (P) and the intensity of the field (E), which under the assumption of quasistatic conditions takes the form [27] given by Equation (4):

$$P^f = \varepsilon_0(\varepsilon' - 1)E \tag{4}$$

where P^f is polarization at constant frequency and ε_0 is the permittivity of free space. The inset of Figure 9 depicts the variation of polarization with temperature for all the tested systems, at constant frequency.

The 'switch' type performance of the, embedded in the polymer matrix, ceramic particles of $BaTiO_3$ lend functional behaviour to the whole composite structure. Optimum functional behaviour is achieved for the 20 phr in $BaTiO_3$ composite, since at higher $BaTiO_3$ concentrations IP (MWS) effect dominates in the dielectric spectra of the composites, diminishing thus their functionality. The latter becomes evident by the absence of the relative peak in the spectrum of the composite with 50 phr in $BaTiO_3$. As adaptive or smart materials are considered composite systems, which are able to vary some of their properties (such as shape, natural vibration frequency, damping coefficient, polarization etc.) in a controllable fashion, under the influence of an external stimulus [27–30]. In accordance with the previous definition, polymer matrix composites incorporating ferroelectric elements can be considered as a suitable base for the development of smart systems, conditioning that critical temperature (T_C) lies within the operational temperature range of the composites.

4. Conclusions

The dielectric response of polymer matrix – ceramic $BaTiO_3$ composites, in a wide frequency and temperature range, was investigated in the present study. Relaxation phenomena were found to be present in all the examined systems. From the slower to the faster one, the recorded processes were attributed to interfacial polarization or MWS effect, glass to rubber transition of the amorphous polymer matrix and local motions of polar side groups of the macromolecular chains. Finally, the functionality of the filler, arising from the thermally activated disorder to order transition, offers a 'switch' type polarization response to the composites with low or moderate $BaTiO_3$ content in the vicinity of the critical temperature (T_C).

Acknowledgements

This work was supported by the General Secretariat for Research and Technology (GSRT) of Greece, in the framework of Joint Research and Technology Programmes between Greece and Tunisia (project code 121-e).

References

[1] Hamami H., Arous M., Lagache M., Kallel A.: Experimental study of relaxations in unidirectional piezoelectric composites. Composites Part A: Applied Science and Manufacturing, **37**, 1–8 (2006).

[2] Ramajo L., Reboredo M., Castro M.: Dielectric response and relaxation phenomena in composites of epoxy resin with $BaTiO_3$ particles. Composites Part A: Applied Science and Manufacturing, **36**, 1267–1274 (2005).

[3] Dang Z-M., Shen Y., Nan C-W.: Dielectric behavior of three-phase percolative Ni-$BaTiO_3$/polyvinylidene fluoride composites. Applied Physics Letters, **81**, 4814–4816 (2002).

[4] Dang Z-M., Lin Y-H., Nan C-W.: Novel ferroeletric polymer composites with high dielectric constant. Advanced Materials, **15**, 1625–1629 (2003).

[5] Popielarz R., Chiang C. K., Nozaki R., Obrzut J.: Dielectric properties of polymer/ferroelectric ceramic composites from 100 Hz to 10 GHz. Macromolecules, **34**, 5910–5915 (2001).

[6] Korotkov N., Gridnev S. A., Konstantinov S. A., Klimentova T. I., Barmin Y. V., Babkina I. V.: Dielectric permittivity and conductivity of amorphous $PbTiO_3$. Ferroelectrics, **299**, 171–177 (2004).

[7] Jylhä L., Honkamo J., Jantunen H., Sihvola A.: Microstructure-based numerical modeling method for effective permittivity of ceramic/polymer composites. Journal of Applied Physics, **97**, 104104/1–104104/7 (2005).

[8] Ramajo L., Castro M. S., Reboredo M. M.: Effect of silane as coupling agent on the dielectric properties of $BaTiO_3$-epoxy composites. Composites Part A: Applied Science and Manufacturing, **38**, 1852–1859 (2007).

[9] Dang Z-M., Yu Y-F., Xu H-P., Bai J.: Study on microstructure and dielectric property of the $BaTiO_3$/epoxy resin composites. Composites Science and Technology, **68**, 171–177 (2008).

[10] Chanmal C. V., Jog J. P.: Dielectric relaxations in PVDF/$BaTiO_3$ nanocomposites. Express Polymer Letters, **2**, 294–301 (2008).

[11] Tsangaris G. M., Psarras G. C., Kouloumbi N.: Electric modulus and interfacial polarization in composite polymeric systems. Journal of Materials Science, **33**, 2027–2037 (1998).

[12] Psarras G. C., Manolakaki E., Tsangaris G. M. Electrical relaxations in polymeric particulate composites of epoxy resin and metal particles. Composites Part A: Applied Science and Manufacturing, **33**, 375–384 (2002).

[13] Kontos G. A., Soulintzis A. L., Karahaliou P. K., Psarras G. C., Georga S. N., Krontiras C. A., Pisanias M. N.: Electrical relaxation dynamics in TiO_2-polymer matrix composites. Express Polymer Letters, **1**, 781–789 (2007).

[14] Van Beek L. K. H.: Dielectric behaviour of heterogeneous systems. in 'Progress in Dielectrics' (ed.: Birks J. B.) Heywood Books, London, 69–117 (1967).

[15] Hedvig P.: Dielectric spectroscopy of polymers. Adam Hilger, Bristol (1977).

[16] Tsangaris G. M., Psarras G. C.: The dielectric response of a polymeric three-component composite. Journal of Materials Science, **34**, 2151–2157 (1999).

[17] McCrum N. G., Read B. E., Williams G.: Inelastic and dielectric effects in polymer solids. Wiley, London (1967).

[18] Ngai K. L.: Test of expected correlation of polymer segmental chain dynamics with temperature-dependent time-scale shifts in concentrated solutions. Macromolecules, **24**, 4865–4870 (1991).

[19] Korzhenko A., Tabellout M., Emery J. R.: Influence of a metal-polymer interfacial interaction on dielectric relaxation properties of polyurethane. Polymer, **40**, 7187–7195 (1999).

[20] Grohens Y., Brogly M., Labbe C., David M-O., Schultz J.: Glass transition of stereoregular poly(methyl methacrylate) at interfaces. Langmuir, **14**, 2929–2932 (1998).

[21] Grohens Y., Hamon L., Reiter G., Soldera A., Holl Y.: Some relevant parameters affecting the glass transition of supported ultra-thin polymer films. The European Physical Journal E -Soft Matter, **8**, 217–224 (2002).

[22] Hartmann L., Gorbatschow W., Hauwede J., Kremer F.: Molecular dynamics in thin films of isotactic poly(methyl methacrylate). The European Physical Journal E -Soft Matter, **8**, 145–154 (2002).

[23] von Hippel A. R.: Dielectrics and waves. Artech, Boston (1995).

[24] Gersten J. I., Smith F. W.: The physics and chemistry of materials. Wiley, New York (2001).

[25] Waser R., Böttger U., Tiedke S.: Polar oxides. Wiley-VCH, Weinheim (2005).

[26] Chelkowski A.: Dielectric physics. Elsevier, Amsterdam (1980).

[27] Böttcher C. J. F., Bordewijk P.: Theory of electric polarization: Dielectrics in time-dependent fields. vol. 2, Elsevier, Amsterdam (1996).

[28] Gandhi M. V., Thompson B. S.: Smart materials and structures. Chapman and Hall, New York (1992).

[29] Petalis P., Makris N., Psarras G. C.: Investigation of the phase transformation behaviour of constrained shape memory alloy wires. Journal of Thermal Analysis and Calorimetry, **84**, 219–224 (2006).

[30] Psarras G. C.: Nanodielectrics: An emerging sector of polymer nanocomposites. Express Polymer Letters, **2**, 460 (2008).

eXPRESS Polymer Letters Vol.2, No.10 (2008) 727–734
Available online at www.expresspolymlett.com
DOI: 10.3144/expresspolymlett.2008.86

Synthesis, characterization and antimicrobial activity of important heterocyclic acrylic copolymers

*H. J. Patel, M. G. Patel, A. K. Patel, K. H. Patel, R. M. Patel**

Department of Chemistry, Sardar Patel University, Vallabh Vidyanagar, Gujarat, India

Received 15 July 2008; accepted in revised form 14 September 2008

Abstract. The acrylate monomer, 7-acryloyloxy-4-methyl coumarin (AMC) has been synthesized by reacting 7-hydroxy-4-methyl coumarin, with acryloyl chloride in the presence of NaOH at 0–5°C. Copolymers of 7-acryloyloxy-4-methyl coumarin (AMC) with vinyl acetate (VAc) were synthesized in DMF (dimethyl formamide) solution at 70±1°C using 2,2′-azobisisobutyronitrile (AIBN) as an initiator with different monomer-to-monomer ratios in the feed. The copolymers were characterized by Fourier transform infra red (FTIR) spectroscopy. The copolymer composition was evaluated by ^{1}H-NMR (proton nuclear magnetic resonance) and was further used to determine reactivity ratios. The monomer reactivity ratios for AMC (M_1)-VAc (M_2) pair were determined by the application of conventional linearization methods such as Fineman-Ross ($r_1 = 0.6924$; $r_2 = 0.6431$), Kelen-Tüdős ($r_1 = 0.6776$; $r_2 = 0.6374$) and extended Kelen-Tüdős ($r_1 = 0.6657$; $r_2 = 0.6256$). Thermo gravimetric analysis showed that thermal decomposition of the copolymers occurred in single stage in the temperature range of 263–458°C. The molecular weights of the polymers were determined using gel permeation chromatography. The homo and copolymers were tested for their antimicrobial properties against selected microorganisms.

Keywords: *thermal properties, 7-hydroxy-4-methyl coumarin, ^{1}H-NMR, antimicrobial activity*

1. Introduction

Copolymerization is one of the important techniques adopted in effecting systematic changes in the properties of the commercially important polymers. The copolymers of acrylic/methacrylic esters have been used for various industrial applications [1]. The chemical structure of a copolymer depends not only on the two-monomer units forming the macromolecule, but also on how such units are distributed along macromolecular chains. This distribution is a direct consequence of each monomer's reactivity in the copolymer molecule [2]. In case of radical copolymerization, the reactivity of a free radical depends on the nature of the side group linked to the radical carbon [3].

Many polymers with reactive functional groups are now being synthesized, tested and used not only for their macromolecular properties, but also for the properties of functional group. These groups provide an approach to a subsequent modification of the polymer for specific end application [4]. Czeh and coworkers synthesized acrylic pressure sensitve adhesives with the help of azo-prester radical initiators [5]. Pazhanisamy and coworkers synthesized copolymers of N-cyclohexylacrylamide/n-butyl acrylate. The resulting copolymers were characterized by FT-IR, NMR, DSC (differential scanning calorimetry) and TGA (thermogravimetric analysis). Reactivity ratios of the monomers were also computed [6]. There are several reports on acrylic polymers for use in binding of pigments as well as for antimicrobial coatings in textile industry [7, 8].

---

*Corresponding author, e-mail: rmpatel_28@yahoo.co.in

Coumarin polymers possessing antimicrobial activity have not received considerable attention in the literature. However the reported coumarin polymers possess variety of functions and appear to be interesting. Although there is a huge number of reports on monomeric coumarin derivatives, there are only a few reports on coumarin polymers. Vinylated coumarins are used as polymerizable fluorescent brightening agents and, when copolymerized with acrylonitrile and methyl acrylate, they faded more slowly than copolymers of acrylonitrile and methylacrylate [9].

A novel blue luminescent polymer bearing coumarin pendants was prepared by Lu *et al.* [10]. Its luminescent properties were determined indicating that it had strong blue fluorescent properties and good film formation ability. This novel polymer can be used as a blue organic electroluminescent material (OELM) in organic electroluminescent devices. Chen and co-workers have studied the radical copolymerization behaviour of styrene with coumarin or 7-acetoxy coumarin [11]. Lindsay and co-workers [12] synthesized the copolymer of coumarin methacrylate with isobornylmethacrylate. These polymers showed tremendous non linear optical properties.

Due to various physiological and biochemical properties of coumarin, our interest was to synthesize acrylic copolymers containing coumarin side groups. Present work focuses on synthesis and characterization of 7-acryloyloxy-4-methyl coumarin (AMC) and its copolymers with vinyl acetate (VAc). Reactivity ratio values of the monomers were determined by various linearization techniques. TGA and GPC results are also included. The prepared copolymers were tested for their antimicrobial activity against various bacteria, fungi and yeast.

2. Experimental

2.1. Materials

Vinyl acetate (VAc) was freed of inhibitor by washing with 5% NaOH and then with water several times. After being dried over anhydrous Na_2SO_4, it was distilled under reduced pressure. 2,2′-Azobis (iso butyronitrile) (AIBN) was recrystallized twice from methanol. 7-hydroxy-4-methyl coumarin and acryloyl chloride were synthesized as per reported procedure [13, 14]. Fractionally distilled solvents were used in the reaction.

2.2. Synthesis of 7-acryloyloxy-4-methyl coumarin (AMC)

7-hydroxy-4-methyl coumarin (0.1 mol) dissolved in absolute alcohol (250 ml), was placed along with sodium hydroxide (0.1 mol) in a two necked 500 ml flask. With continuous stirring of the reaction mixture at 0–5°C, freshly distilled acryloyl chloride (0.11 mol) was added slowly from an addition funnel. An hour after the completion of addition, the contents were stirred for 90 minutes and were poured into crushed ice water mixture where a white colored monomer was separated out. It was filtered, washed with cold water and dried. Further the monomer was recrystallized from methanol (yield: 89%, m.p.:122°C). The formation of the monomer was confirmed by FT-IR (Figure 1a) and ^{1}H-NMR spectra (Figure 1b).

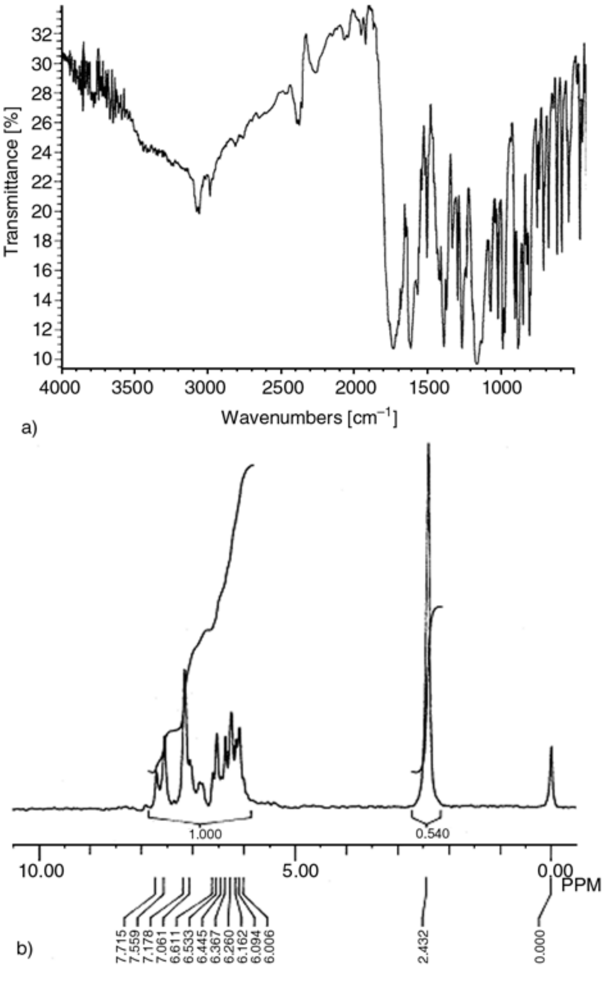

Figure 1. Characterization of AMC (a) FT-IR and (b) ^{1}H-NMR

IR (KBr, cm^{-1}): 3073 (–CH stretching vibration of the aromatic ring), 2986 (–CH_3), 1737 (broad, C=O of acrylate and of coumarin moiety), 1630 (C=C), 1240 (asymmetric C–O–C), 1142 (symmetric C–O–C), 890 (–CH bending mode of vinyl group), 730 (rocking mode of vinyl group).
^{1}H-NMR (δ [ppm]) (60 MHz): 6.26 (1H, –CH=), 2.43 (3H, CH_3), 6.36 (2H, non-equivalent methylene protons), 7.06–7.72 (3H, aromatic protons).

2.3. Homopolymerization of AMC

This was carried out using solution polymerization technique. AIBN (1% wt of monomer) was added to 2 g of AMC dissolved in 10 ml of DMF taken in a polymerization tube. The content was degassed with nitrogen and kept at 70±1°C in a water bath for 5 hours. The polymer was precipitated by pouring the contents of the polymerization tube into excess methanol. The resultant precipitate was filtered and dried in vacuum at 40°C.

2.4. Copolymerization of AMC with VAc

Copolymerization was carried out by solution polymerization technique using DMF as a solvent and AIBN as a free radical initiator at 70±1°C under nitrogen atmosphere. Appropriate amounts of AMC, VAc, AIBN (1 wt% of the monomers) and DMF (Table 1) were mixed in a polymerization tube, degassed with nitrogen and kept in a thermostat (70±1°C) for a definite period of time so as to maintain the conversion below 10%. Then the contents were precipitated by pouring into excess methanol and filtered. The precipitate was purified by dissolving in dimethyl formamide and reprecipitated using methanol, filtered and dried in a vacuum oven at 40°C. Figure 2 shows the copolymerization of AMC with VAc.

2.5. Measurements

IR spectra of the monomer and polymers were recorded on Nicolet 400_D FT-IR spectrometer using KBr pellets. ^{1}H-NMR spectra of the samples were run on a Hitachi-R-1500 permanent magnet 60 MHz spectrophotometer. TGA curves of the homo and copolymers were recorded on TA instrument (USA) 2690 thermogravimetric analyzer in nitrogen atmosphere at a heating rate of 10°C/min. The number average and weight average molecular weight of the polymers were determined by gel permeation chromatography using polystyrene as standard and DMF is used as eluent at 1.0 ml/min flow rate.

2.6. Antimicrobial activity

The homo and copolymers obtained were tested against different bacterial strains (*Bacillus subtilis, Escherichia coli and Staphylococcus citreus*), fungal strains (*Aspergillus niger, Sporotichum pulveruletum and Trichocerma lignorum*) and yeast strains (*Candida utilis, Saccharomyces cerevisiac*

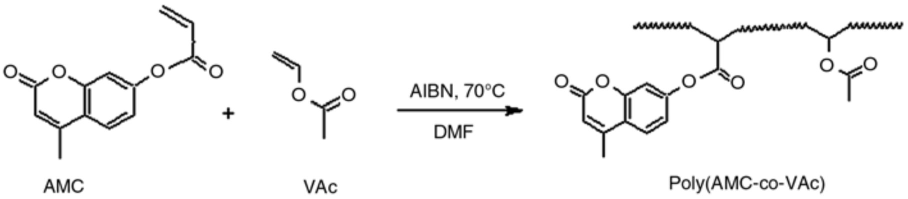

Figure 2. Reaction scheme of P(AMC-co-VAc)

Table 1. Copolymer composition data of AMC and VAc

Polymer No.	Mole fraction in feed		Intensities of protons		C	Mole fraction in copolymer	
	AMC (M_1)	VAc (M_2)	I_{arom}	I_{alip}		AMC (m_1)	VAc (m_2)
1	1.0	–	–	–	–	1.0	–
2	0.5	0.5	34.81	148.76	0.234	0.508	0.492
3	0.4	0.6	27.65	139.64	0.198	0.425	0.575
4	0.3	0.7	21.38	131.97	0.162	0.344	0.656
5	0.2	0.8	17.08	147.24	0.116	0.243	0.757
6	0.1	0.9	13.49	201.34	0.067	0.139	0.861
7	–	1.0	–	–	–	–	1.0

and Pichia stipitis). The details of the experimental procedures have been reported in our earlier publication [15, 16].

3. Results and Discussion

Different homo and copolymers were obtained by the free radical solution polymerization technique. The mole fractions of AMC ranging from 0.5 to 0.1 in the feed were studied in a wide composition interval. The reaction time was selected in trials to give conversions less than 10% in order to satisfy the differential copolymerization equation. The monomeric units of the copolymer are shown in Figure 2. The data on the composition of the feed and copolymers are given in Table 1.

3.1. Characterization of polymers

3.1.1. Solubility

The homo and copolymers synthesized were soluble in chloroform, dimethyl formamide, dimethyl sulfoxide, toluene and tetrahydro furan. It is insoluble in n-hexane, acetone and hydroxyl group containing solvents such as methanol and ethanol.

3.1.2. Infrared spectra

The IR spectra of the homo and copolymers are shown in Figure 3. The two medium bands at 2966 and 2932 cm^{-1} may be attributed to the asymmetric and symmetric C–H stretching vibration of methylene group where as, absorption at 1455 cm^{-1} may be due to bending vibration of $-CH_2$ group. The strong absorptions at 1394 cm^{-1} may be traced due to in-plane bending vibrations of methyl and methylene groups. The broad band at 1736 cm^{-1} is assigned to C=O stretching vibration of ester group (due to presence of three carbonyl group in the monomer AMC and VAc) and sharp band at 1260 cm^{-1} and a broad band at 1148 cm^{-1} are assigned C–O stretching vibration of ester group. Two strong bands at 1502 and 1585 cm^{-1} are observed which the characteristic absorptions of phenyl ring. As the content of AMC in the copolymers decreases the intensities of these peaks also decreases. The absence of 1630 cm^{-1} absorption in the polymers is indicative of the participation of the vinyl group in the polymerization.

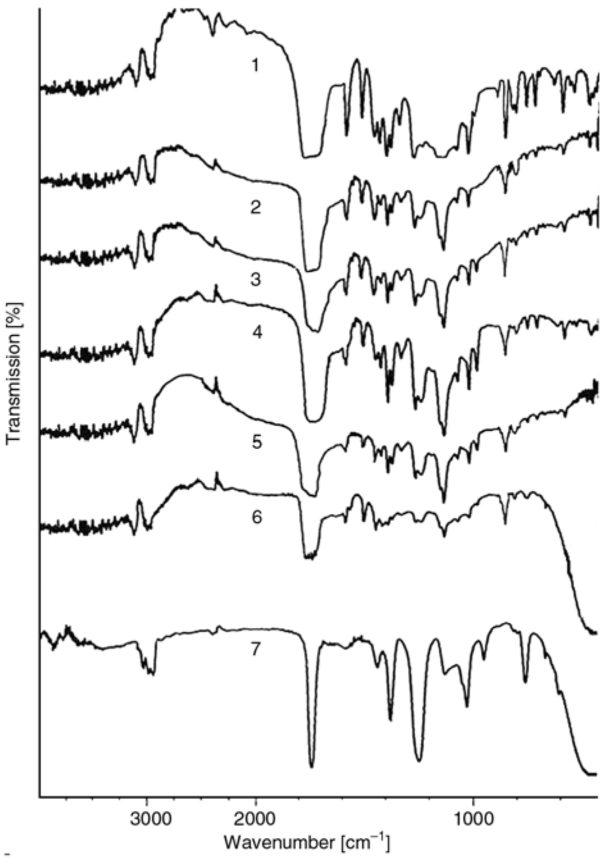

Figure 3. IR spectra of P(AMC), P(VAc) and copolymers

3.2. Copolymer composition and monomer reactivity ratio

The average compositions of the copolymer samples were determined by ^{1}H-NMR spectra. The assignment of the resonance peaks in the in the ^{1}H-NMR spectrum leads to accurate evaluation of each monomeric content incorporated into the copolymer chains. Thus, the mole fraction of AMC in the copolymer was calculated by measuring the integrated peak height of aromatic protons of AMC to that of total aliphatic protons in the copolymer as described in Equation (1):

$$\therefore C = \frac{Intensity\,of\,aromatic\,protons\,(I_{Ar})}{Intensity\,of\,aliphatic\,protons\,(I_{Al})} \qquad (1)$$

The following expression (Equation (2)) is used to determine the composition of the copolymers. Let m_1 be the mole fraction of AMC and $1 - m_1$ be that of VAc. AMC contains three aromatic protons and seven aliphatic protons, and VAc contains six aliphatic protons (Equation (2)).

$$\therefore C = \frac{3m_1}{7m_1 + 6(1 - m_1)} \tag{2}$$

This on simplification gives (Equation (3)):

$$\therefore m_1 = \frac{6C}{3 - C} \tag{3}$$

Based on Equation (3), the mole fractions of AMC in the copolymers were determined by measuring the integral peak height of aromatic proton and aliphatic proton signals. Table 1 gives the values of *C* and the corresponding mole fractions of AMC in the copolymers.

From the monomer feed ratios and the copolymer composition, the reactivity ratios of AMC and VAc were determined by the application of conventional linearization methods, such as Fineman-Ross (F-R) [17], Kelen-Tüdős (K-T) [18] and extended Kelen-Tüdős (Ext. K-T) [19]. The F-R and K-T parameters for the copolymers are presented in Table 2 and those for Ext. K-T are shown in Table 3. The reactivity ratios values obtained from F-R plot, K-T and Ext. K-T plots (Figures 4a, 4b and 4c) are presented in Table 4.

The reactivity ratio values indicate that the AMC radical favors its own monomer rather than VAc. Generally the neutral olefin molecules and those

Table 2. F-R and K-T parameters for copolymers of AMC with VAc

Polymer No.	AMC (M_1) [mole]	VAc (M_2) [mole]	Conversion (w) [%]	x	y	F	G	ξ	η
2	0.5	0.5	9.12	1.00	0.969	1.033	–0.033	0.799	–0.025
3	0.4	0.6	8.83	0.67	0.745	0.597	–0.228	0.697	–0.266
4	0.3	0.7	8.72	0.43	0.548	0.334	–0.353	0.563	–0.595
5	0.2	0.8	9.01	0.25	0.364	0.172	–0.436	0.398	–1.012
6	0.1	0.9	8.98	0.11	0.189	0.065	–0.476	0.20	–1.467

where, $x = M_1/M_2$; $y = m_1/(1 - m_1)$; $F = x^2/y$; $G = x[(y - 1)/y]$; $\alpha = \sqrt{F_M \cdot F_m} = 0.272$; $\xi = F/(\alpha + F)$; $\eta = G/\alpha + F$

Table 3. Extended K-T parameters for copolymers of AMC with VAc

Polymer No.	ζ_2	ζ_1	z	F	G	ξ	η
2	0.090	0.092	1.034	0.965	0.031	0.783	0.025
3	0.079	0.088	1.113	0.595	–0.234	0.690	–0.271
4	0.076	0.093	1.234	0.343	–0.385	0.563	–0.630
5	0.072	0.094	1.298	0.190	–0.523	0.416	–1.143
6	0.071	0.104	1.478	0.073	–0.567	0.216	–1.664

where, $\mu = \mu_2/\mu_1 = 0.374$; $\zeta_2 = w(\mu + x/\mu + y)$; $\zeta_1 = \zeta_2(y/x)$; $z = \log(1 - \zeta_1)/\log(1 - \zeta_2)$; $F = y/z^2$; $G = (y - 1)/z$; $\alpha = \sqrt{F_M \cdot F_m} = 0.2669$; $\xi = F/(\alpha + F)$; $\eta = G/\alpha + F$

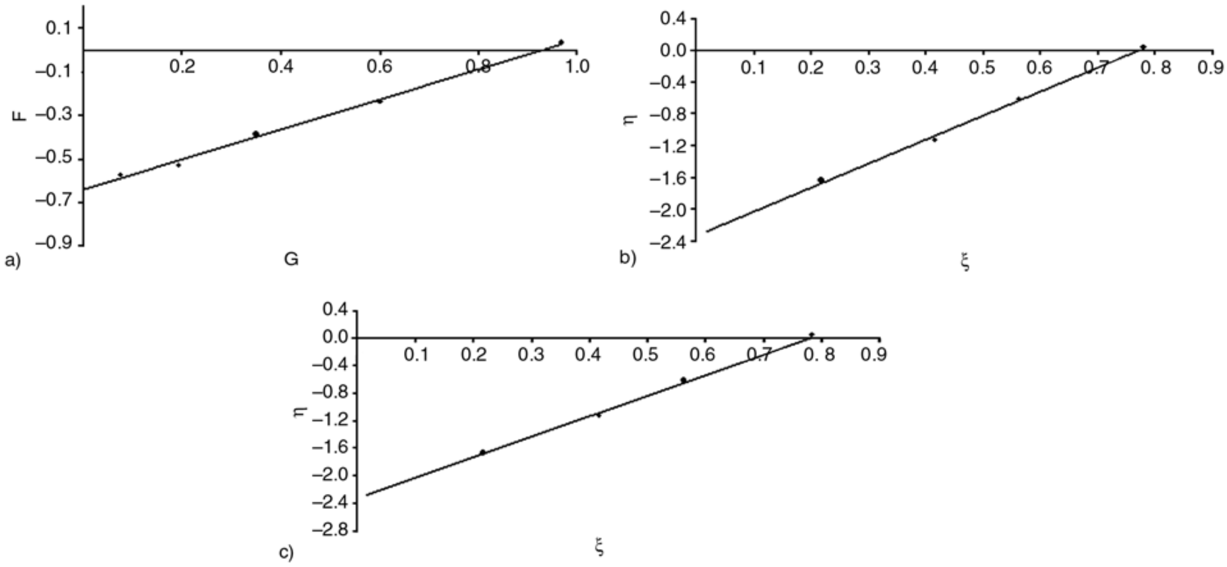

Figure 4. P(AMC-co-VAc) system (a) Finemann-Ross plot, (b) Kelen-Tüdős plot and (c) Extended Kelen-Tüdős plot

Table 4. Monomer reactivity ratio by different linearization methods

Method	r_1	r_2	r_1r_2
Fineman-Ross	0.6924	0.6431	0.6173
Kelen-Tüdős	0.6776	0.6374	0.6690
Extended Kelen-Tüdős	0.6657	0.6256`	0.6530

r_1 and r_2 are the reactivity ratios of AMC and VAc, respectively

olefin molecules containing moderately electron-donating or electron-withdrawing groups favor free radical polymerization. VAc consists of electron withdrawing acetate group attached to olefin molecule while AMC consist of electron withdrawing phenyl group. But the net charge on AMC is less compared to VAc and thus is more reactive. Also stearic effects and overall polarity of molecule plays a key role in relative reactivity of monomers. Since the r_1 and r_2 values are less than one, this system gives rise to azeotropic polymerization at a particular composition of the monomers which is calculated using Equation (4) [20]:

$$N_1 = \frac{(1-r_2)}{(2-r_1-r_2)} = 0.537 \tag{4}$$

When the mole fraction of AMC in the feed is 0.537, the copolymer formed will have the same composition as that of feed. When the mole fraction of the feed is less than 0.537 with respect to AMC, the copolymer is richer in this monomeric unit. When the mole fraction of AMC in the feed is above 0.537, the copolymer is relatively richer in VAc monomeric unit.

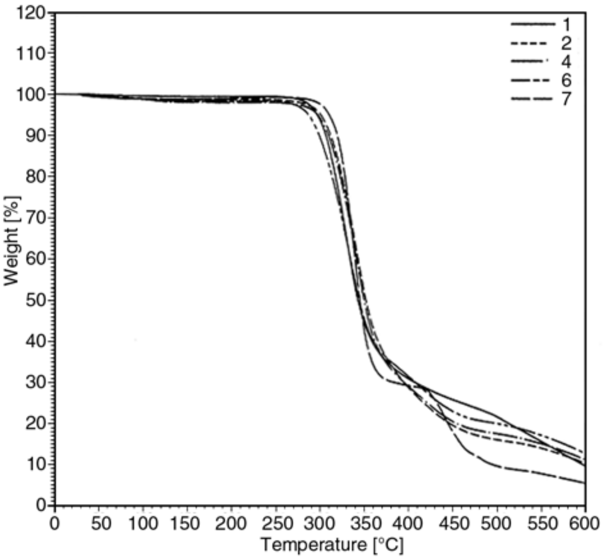

Figure 5. TG curves of P(AMC), P(AMC-co-VAc) and P(VAc)

3.3. Thermogravimetric analysis

TGA curves for P(AMC), P(VAc) and P(AMC-co-VAc) are shown in Figure 5. The thermograms clearly indicate that P(AMC) and P(AMC-co-VAc) undergoes single step degradation where as P(VAc) undergoes double step degradation. The decomposition temperature of different copolymers ranges between to 263–567°C. The activation energy found by Broido's method [21] lies in the range of 38 to 50 kJ·mole^{-1} whereas integral procedural decomposition temperature found by Doyle's method [22] lies in the range of 348–358°C. The detailed result are shown in Table 5 and indicates that value of E_A and IPDT does not depend on AMC content in the copolymers i.e. it may increase or decrease randomly with decrease in AMC content.

Table 5. TGA, GPC and viscosity data for homo and copolymers of AMC with VAc

Polymer No.	Decomposition temperature range [°C]	T$_{50}$[a] [°C]	IPDT[b] [°C]	Activation energy[c] (E_A) [kJ·mole^{-1}]	$\overline{M}_n$	$\overline{M}_w$	$\overline{M}_z$	Poly dispersity index $\overline{M}_w/\overline{M}_n$	Intrinsic viscosity (η) [dl·g^{-1}]
1	280–403	341	348	43	31230	47070	63470	1.507	0.212
2	280–450	351	355	40	30430	44590	59600	1.465	0.196
4	286–455	352	358	38	26060	37990	51250	1.458	0.168
6	263–458	343	348	39	21840	30320	40050	1.388	0.138
7	283–373 419–567	338	358	50	20580	27130	36380	1.318	0.108

[a] temperature for 50% weight loss

[b] integral procedural decomposition temperature by Doyle's method

[c] by Broido's method

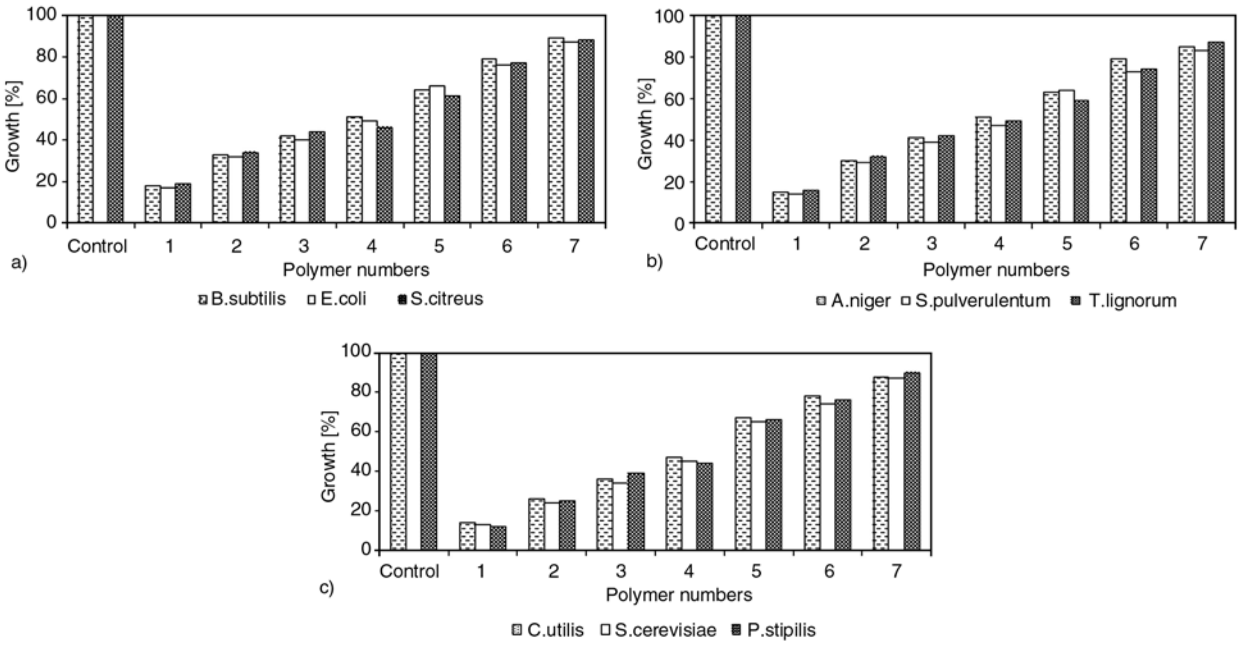

Figure 6. Effect of P(AMC), P(AMC-co-VAc) and P(VAc) on growth of (a) bacteria, (b) fungi and (c) yeast

3.4. Molecular weights

The number and weight average molecular weight of P(AMC) and P(AMC-co-VAc) were determined by gel permeation chromatography and are presented in Table 5. The polydispersity indices of different polymers lies in the ranges 1.318 to 1.507 respectively whereas intrinsic viscosity [η] ranges from 0.108 to 0.196 dl·g^{-1}. The results indicate that with decrease in the AMC content in the copolymers, molecular weights, polydispesity and viscosity decreases to the considerable extent.

3.5. Antimicrobial activity

The results obtained for antimicrobial activity of the P(AMC), P(AMC-co-VAc) and P(VAc) are presented in Figures 6a, 6b and 6c. P(AMC) allows 17–19% growth of bacteria, where as its copolymers favors 24–78% growth. Fungi in presence of P(AMC) register around 14–16% growth, while 29–79% growth for fungi is observed in the copolymers. Yeast in presence of P(AMC) shows 12–14% growth, while 24–78% growth for yeast is observed in copolymers. The P(AMC) is found to be most effective in inhibiting the growth of microorganisms; these may be traced due to heterocyclic moiety of coumarin. As the percentage of monomer AMC increases in the copolymer the antimicrobial activity of the copolymers increases.

4. Conclusions

New acrylate based homo and copolymers were synthesized by free radical solution polymerization technique. The monomers and copolymers were characterized by spectroscopic methods. The reactivity ratio of AMC (r_1) is greater than VAc (r_2) and the product of r_1r_2 is less than one. This shows that the monomers were distributed in the copolymer chain in random fashion. Thermo gravimetric analysis showed that P(AMC) and P(AMC-co-VAc) undergoes single step decomposition where as P(VAc) undergoes double step decomposition. All the polymers showed moderate thermal stability. The number average molecular weight and weight average molecular weight were in the range of 20580 to 31230 and 27130 to 47070 respectively. Molecular weight increases with increase in content of AMC in copolymer. Presence of 4-methylcoumarin group in the polymer chain imparts antimicrobial properties to the polymers. The results of antimicrobial activity shows that the copolymers containing AMC shows excellent growth inhibition against all microorganisms and as AMC content in the copolymers increases the growth inhibition of microorganisms also increases.

References

[1] Mark H. F., Bikales N. M., Overberger C. G., Menges G.: Encyclopedia of polymer science and engineering. Wiley, New York (1986).

[2] Gatica N., Natali F., Alejandra O., Deodato R.: Synthesis and characterization of functionalized vinyl copolymers I: Structure-monomer reactivity relationship in copolymers containing N-vinyl-2-pyrrolidone moieties. Journal of the Chilean Chemical Society, **50**, 581–585 (2005).

[3] Gatica N., Fernandez N., Opazo E., Alegria S., Gargalio L., Radic D.: Synthesis and characterization of functionalized vinyl copolymers: Electronegativity and comonomer reactivity in radical copolymerization. Polymer International, **52**, 1280–1286 (2003).

[4] Vogl O., Albertsson A. C., Janovic Z.: New developments in speciality polymers: Polymeric stabilizers. Polymer, **26**, 1288–1296 (1985).

[5] Czech Z., Butwin A., Herko E., Hefczye B., Zawadiak J.: Novel azo-perester radical initiators used for synthesis of acrylic pressure sensitive adhesives. Express Polymer Letters, **2**, 277–283 (2008).

[6] Pazhanisamy P., Reddy B. S. R.: Copolymers of N-cyclohexylacrylamide and *n*-butyl acrylate: Synthesis, characterization, monomer reactivity ratio and mean sequence length. Express Polymer Letters, **1**, 391–396 (2007).

[7] Nuessle A. C., Kine B. B.: Acrylic resin in textile processing. Industrial and Engineering Chemistry, **35**, 1287–1293 (1953).

[8] Ye W., Leung M. F., Xin J., Kwong T. L., Lee D. K. L., Li P.: Novel core-shell particles with poly(*n*-butyl acrylate) cores and chitosan shells as an antibacteial coating for textiles. Polymer, **46**, 10538–10543 (2005).

[9] Osawa E., Nozawa T., Kurihara O.: Synthesis of polymerizable fluorescent brightening agents and photodecomposition of their copolymers with acrylonitrile and methyl acrylate (in Japanese). Kogyo Kogaku Zasshi, **68**, 519–524 (1965).

[10] Lu Z. Y., Yuan T. S., Chen Y. L., Wei X. Q., Xie M. G., Zhu W. G.: Synthesis of a novel blue light emitting polymer material bearing coumarin pendants. Chinese Chemical Letters, **13**, 674–677 (2002).

[11] Chen Y., Chen Y-H., Wang J. H.: Radical copolymerization behaviors of styrene and coumarin. Journal of Polymer Research, **1**, 295–303 (1994).

[12] Lindsay G. A., Hoover J. M.: Near T_g relaxation behaviour in non-linear optical polymers and views on physical sign. Polymer Preprints, **34**, 771–772 (1993).

[13] Vogel A. I., Tatchell A. R., Furniss A. J., Hannaford P. W., Smith P. W. G.: Vogel's textbook of practical organic chemistry. Pearson Education, Singapore (1989).

[14] Stempel G. H., Cross R. P., Mareioll R. P.: Preparation of acryloyl chloride. Journal of American Chemical Society, **72**, 2299–2300 (1950).

[15] Patel J. N., Patel M. V., Patel R. M.: Copolymers of 2,4-dichlorophenyl methacrylate with styrene: synthesis, thermal properties and antimicrobial activity. Journal of Macromolecular Science Part A: Pure and Applied Chemistry, **42**, 71–83 (2005).

[16] Patel M. G., Patel H. J., Patel J. R., Patel K. H., Patel R. M.: Development and applications of novel acrylic copolymers. International Journal of Polymeric Materials, **57**, 165–176 (2008).

[17] Fineman M., Ross S. D.: Linear method for determining monomer reactivity ratios in copolymerization. Journal of Polymer Science, **5**, 259–265 (1950).

[18] Kelen T., Tüdős F.: Analysis of the linear methods for determining copolymerization reactivity ratios: A new improved linear graphic method. Journal of Macromolecular Science Part A: Pure and Applied Chemistry, **9**, 1–27 (1975).

[19] Kelen T., Tüdős F., Turcsányi B., Kennedy J. P.: Analysis of the linear method for determining and critical re-examination of cabocationic copolymerization data. Journal of Polymer Science: Polymer Chemistry, **15**, 3041–3074 (1977).

[20] Gowariker V. R., Viswanathan N. V., Sreedhar J.: Polymer science. New Age International, New Delhi (1986).

[21] Broido A.: A simple, sensitive graphical method of treating thermogravimetric analysis data. Journal of Polymer Science Part A: Polymer Physics, **27**, 1761–1774 (1969).

[22] Doyle C. D.: Estimating thermal stability of experimental polymers by empirical thermogravimetric analysis. Analytical Chemistry, **33**, 77–79 (1961).

eXPRESS Polymer Letters Vol.2, No.10 (2008) 735–745
Available online at www.expresspolymlett.com
DOI: 10.3144/expresspolymlett.2008.87

Multi-walled carbon nanotube filled polypropylene nanocomposites based on masterbatch route: Improvement of dispersion and mechanical properties through PP-g-MA addition

K. Prashantha[1], J. Soulestin[1], M. F. Lacrampe[1], M. Claes[2], G. Dupin[2], P. Krawczak[1]*

[1]Ecole des Mines de Douai Polymers and Composites Technology & Mechanical Engineering Department,
941 rue Charles Bourseul, BP 10838, 59508 Douai Cedex, France
[2]Nanocyl S.A. Rue de l’Essor, 4 B-5060 Sambreville, Belgium

Received 18 July 2008; accepted in revised form 14 September 2008

Abstract. Multi-wall carbon nanotubes (MWNTs) filled polypropylene (PP) nanocomposites were prepared through diluting a PP/MWNT masterbatch in a PP matrix by melt compounding with a twin screw extruder. Polypropylene grafted maleic anhydride (PP-g-MA) was used to promote the carbon nanotubes dispersion. The effect of PP-g-MA addition on the rheological, mechanical and morphological properties of the nanocomposites was assessed for different MWNTs loadings. Scanning electron microscopy (SEM) has shown that nanotubes are distributed reasonably uniformly. A better dispersion and good adhesion between the nanotubes and the PP matrix is caused by wrapping of PP-g-MA on MWNTs. When PP-g-MA is added, dynamic moduli and viscosity further increases compared to PP/MWNT nanocomposites. The rheological percolation threshold drops significantly. Tensile and flexural moduli and Charpy impact resistance of the nanocomposites also increases by the addition of PP-g-MA. The present study confirms that PP-g-MA is efficient to promote the dispersion of MWNTs in PP matrix and serves as an adhesive to increase their interfacial strength, hence greatly improving the rheological percolation threshold and mechanical properties of PP/MWNT nanocomposites.

***Keywords:** nanocomposites, multi wall carbon nanotubes, polypropylene, masterbatch, PP-g-MA*

1. Introduction

Carbon nanotubes (CNTs) are ideal fillers for polymer composites due to their high Young’s modulus combined with good electrical and thermal conductivity. The very high aspect ratio makes it likely that the addition of a small amount of CNTs strongly improves the electrical [1], thermal [2] and mechanical [3] properties of the polymer matrix. Thus, CNT/polymer composites combine the good processability of the polymers with the excellent mechanical and other functional properties of the CNTs. However, the strong intermolecular van der Waals interactions among the nanotubes, in combination with their high surface area and high aspect ratio, commonly causes significant agglomeration, and prevents transfer of their superior properties to the matrix [4]. Thus, dispersion of CNTs in polymer matrices plays a predominant role in the mechanical and other functional properties of polymer/CNT composites [5].

To disperse CNTs into the polymers homogeneously, the entanglement of CNTs inherited from their synthetic process and van der Waals forces between CNTs should be minimized. Good disper-

---

*Corresponding author, e-mail: prashantha@ensm-douai.fr sion has been reported for polar polymers such as poly(methyl methacrylate) [6], polycarbonate [7], polyacrylonitrile [8] and poly(vinyl alcohol) [9]. However, CNT dispersion in non-polar polymers such as polypropylene during melt processing remains a challenge. Techniques such as end-group functionalization [10–12], use of ionic surfactants [13], shear mixing [14, 15] and plasma coating [16] have been used to improve dispersion and exfoliation of nanotubes in polypropylene matrix. Polypropylene compatibility with fillers has been improved by matrix modification by grafting it with reactive moieties, such as acrylic acid, acrylic esters, and maleic anhydride [17, 18]. In that case, improvement in thermal and electrical properties of polypropylene/nanotube composites has been reported [14, 19–21].

Compatibilizers containing maleic anhydride functionalities are effective in improving physical properties of composites. The interaction between functional groups of the compatibilizer and carboxyl or amine groups of multi wall carbon nanotubes (MWNTs) has stabilized the morphology and improved the interfacial interaction between MWNTs and the polypropylene matrix [22]. Especially maleic anhydride grafted polypropylene (PP-g-MA) is one of the most promising candidates that can improve the PP/MWNT composite properties. In general, the nanoscale dispersion of MWNTs in polypropylene matrix is achieved by strong hydrogen bonding between hydroxyl groups of the MWNTs and maleic anhydride groups of PP-g-MA, depending upon the chemical similarity of polypropylene matrix and the grafted polypropylene [22].

Another key issue is related to handling of CNTs in plastic parts manufacturing workshop. Using commercial masterbatch in the production of CNTs based polymer nanocomposites would be a better choice as it offers a dust free solution, with no health and safety risks in comparison to bulk nanotube dispersion process. Other benefits of using masterbatch include elimination of dispersion difficulties, formulation development and easy handling. Nevertheless, distribution of masterbatch and subsequent dispersion of nanotubes in the polymer matrix after processing needs to be ascertained. Recent studies from our laboratory reported the compounding of masterbatch based PP- multi wall carbon nanotubes (MWNTs) nanocomposites using twin screw extrusion process [23]. The results showed good mechanical properties, similar to those obtained with direct mixing of MWNTs in PP matrix as reported in the literature [24, 25]. However, scanning electron microscopy (SEM) observations revealed a few masterbatch aggregates which were imperfectly mixed during extrusion.

Therefore, in the present work, PP-g-MA is used to enhance the dispersion of MWNTs in masterbatch based PP/MWNT nanocomposites. The mechanism promoting the improved dispersion induced by the PP-g-MA will be discussed through a microscopic study. The influence of the PP-g-MA addition on structural and mechanical properties of PP/MWNT composites will be discussed in conjunction with the microscopic studies.

2. Experimental

2.1. Composites fabrication

Polypropylene (PP)-multi wall carbon nanotubes (MWNTs) nanocomposites were produced by mixing homo PP granules [Polychim polypropylene with a melt flow index of 12 g/10 min. at 190°C] and 2 wt% PP-g-MA [Dupont Fusabond] with the commercial masterbatch containing 20 wt% of MWNT [‘Plasticyl 2001’ supplied by Nanocyl, Belgium] in a co-rotating twin screw extruder [Clextral BC] at barrel temperature of 195–210°C, and a screw speed of 50 rpm. The specifications of MWNTs in the masterbatch are as follows: range of diameter 9–11 nm, mean length of the nanotubes 1.2 μm, and purity higher than 90%. During melt extrusion ventilation was kept on to remove trapped air in blends. After pelletizing, the nanocomposite granules were compression moulded into 4 mm thick plates using a hydraulic press at 180°C during 2 min for rheological experiments. For mechanical testing, nanocomposite granules were injection-moulded [using KraussMaffei KM80-160E injection moulding machine] into standard test specimen for tensile, impact and flexural test. The barrel temperature ranged 205–220°C and the mould temperature was kept at 25°C. The holding pressure and screw rotational speed were 300 bar and 100 rpm, respectively. The nanocomposites of PP/MWNT and 2 wt% PP-g-MA filled PP/MWNT were fabricated by varying nanotube content starting from

1 to 5 wt%. As a reference, neat PP was also similarly processed for rheological and mechanical studies.

2.2. Morphological characterization

Scanning electron microscopic images were taken on the cryofactured surfaces of nanocomposite. A thin layer of carbon was sputter deposited onto the sample. Electron microscopy imaging of the nanocomposite was performed under high vacuum with a Hitachi S-4300SE/N SEM instrument operating at 5 kV.

2.3. Rheological measurements

Oscillatory shear measurements were carried out using an Advanced Rheometrics Expansion System (ARES) equipped with a cone and plate geometry device (25 mm diameter 0.1 rad cone angle and 0.4554 mm gap) at 180°C. Frequency sweeps with an angular velocity between 0.1 and 100 rad/s were performed in the linear viscoelastic regime at strain of 5%. Samples were left to equilibrate for 5 minutes prior to measurement.

2.4. Mechanical characterization

Mechanical performance of all compounded materials was evaluated from injection moulded specimens at 25°C. Tensile properties of the moulded dogbone specimens were measured using an Instron machine at a crosshead rate of 20 mm/min according to the ISO 527 standard. The tensile strength and modulus could be directly obtained from the stress–strain curves. Flexural properties of the nanocomposites were determined on the same tensile machine by three point bending tests as per ISO 178 standard at a thickness to span length ratio of 1:16 and at cross head displacement rate of 2 mm/min. Charpy notched and un-notched impact tests were carried out as per ISO 179-1 standard on a Zwick impact pendulum. All the reported values were calculated as averages over five specimens for each composition.

3. Results and discussion

3.1. Investigation of the optimum PP-g-MA concentration

In order to evaluate the optimum concentration of PP-g-MA in PP/MWNT nanocomposites, tensile behaviour of PP/MWNT nanocomposites was investigated at various PP-g-MA loadings by keeping 2 wt% of MWNTs constant. It is very important to keep in mind that too low PP-g-MA content would not be able to enhance the compatibility enough, while too high maleic anhydride content may lead to deterioration of the nanocomposite properties because of the poor mechanical properties of low molecular weight PP-g-MA. Therefore, it is necessary to investigate the optimum concentration of PP-g-MA. Figure 1 shows the tensile properties of PP/MWNT composites without PP-g-MA and at different weight percentages of PP-g-MA [i.e. 1, 2 and 3 wt%]. It is clear from the results that tensile properties of the composites with PP-g-MA has shown better tensile properties than PP/MWNT alone and the properties tend to increase with increase in PP-g-MA content up to 2 wt% and decrease for 3 wt% PP-g-MA nanocomposites. This is due to the fact that, PP-g-MA of low molecular weight and high MA content led to better interaction with nanotubes and PP matrix promoting the dispersion of nanotubes. However, the addition of lower molecular weight PP-g-MA had a negative effect on mechanical properties of the PP/MWNT nanocomposites. Therefore, there exists an optimum concentration of PP-g-MA for the pro-

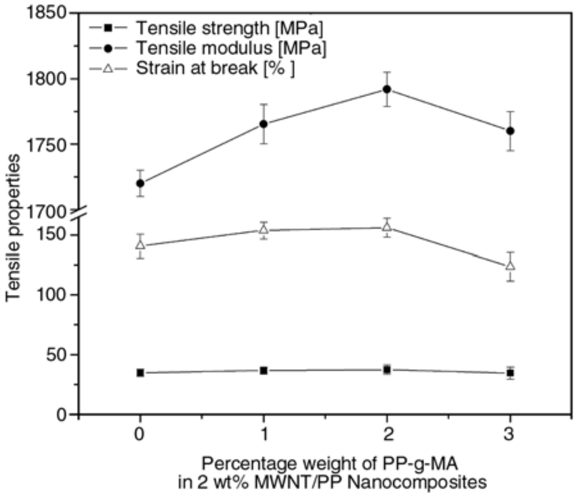

Figure 1. Effect of PP-g-MA content on tensile properties of PP/MWNT nanocomposites

cessing of highly concentrated PP/MWNT masterbatches.

3.2. Morphological characterization

The efficiency of nanofillers in reinforcing the polymer matrix is primarily determined by the degree of its dispersion in the matrix. Therefore, morphological characterization is very important for the evaluation of the dispersion state of carbon nanotubes in the polymer matrix. In this study, dispersion of MWNTs in PP/MWNT and PP/MWNT/PP-g-MA nanocomposites was examined by using SEM. The SEM images of composites containing 3.0 wt% MWNTs with and without PP-g-MA are shown in Figure 2. The selected SEM observations are representative of the dispersion of the carbon nanotubes in the PP matrix. For PP/MWNT nanocomposites (Figures 2a and 2b), a large amount of self-organized MWNTs bundles was observed on the cryofractured surface. This indicates that a significant part of the nanotubes was dispersed as nanotubes aggregates due to the imperfect mixing of the masterbatch. But in the PP/MWNT/PP-g-MA composites (Figures 2c and 2d), reasonably uniform dispersion and good distribution of the MWNTs was observed with a small amount of aggregates. From these observations one can conclude that the added PP-g-MA promotes the dispersion of individual carbon nanotubes and limits the presence of nanotubes aggregates.

Moreover, in the case of the PP/MWNT/PP-g-MA composite (Figures 2c and 2d), the diameter of the MWNT has increased to about 150–200 nm, while in case of PP/MWNT diameter is about 30-40 nm. The diameter of the nanotubes was determined from different SEM observations at different places for each composite so as to be representative of the average diameter. As the nanotube used for the different composites is the same, this increase in the diameter of the nanotubes is assumed to be due to wrapping of nanotubes by PP-g-MA thanks to

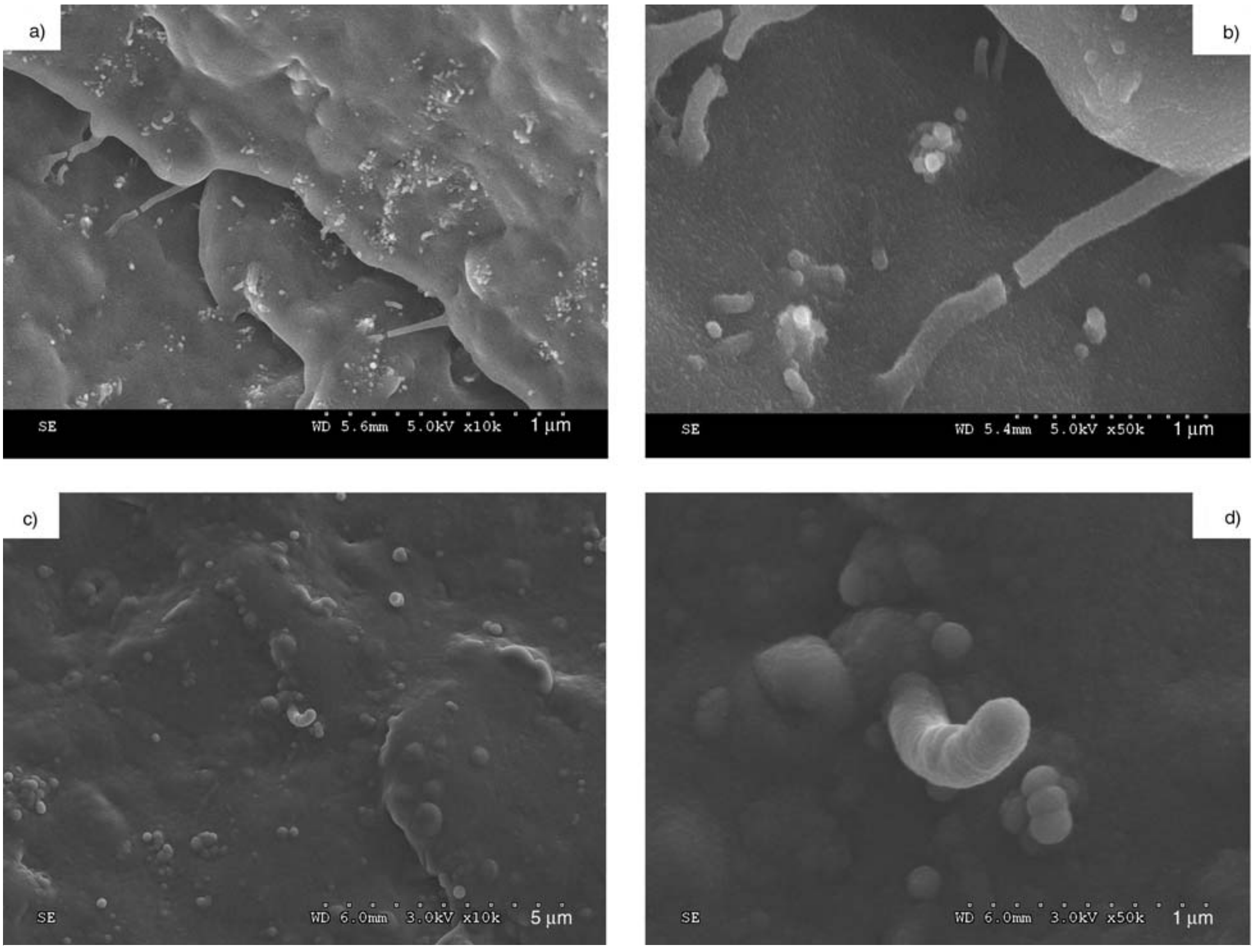

Figure 2. High and low resolution scanning electron micrographs of (a) and (b) PP/MWNT & (c) and (d) PP/MWNT/PP-g-MA melt mixed bulk samples

hydrogen bonding. During extrusion process, due to specific interactions between the chemical groups of the carbon nanotube surface and grafted maleic anhydride groups, the PP-g-MA adsorbs onto the nanotubes giving a coating of a few nanometers thickness. Indeed, as shown by Lee *et al*. [22] hydrogen bonding between maleic anhydride and the surface-bound acid groups of the nanotube is possible, leading to the formation of a PP-g-MA coating onto the surface. After cryofracture, due to the adhesion of PP-g-MA on the nanotubes, this coating remains as observed by SEM (Figure 2d). In contrary, for PP/MWNT composites, no coating is observed and the measured diameter is in the range given by the CNT supplier. This tends to confirm the existence of the coating obtained via the addition of PP-g-MA during extrusion for PP/MWNT/PP-g-MA composites. Further adhesion of PP-g-MA on the nanotube surfaces, modifies the wettability of the nanotubes and promotes the disentanglement in the PP matrix leading to a better dispersion during melt processing.

3.3. Rheological characterization

So as to support the SEM observations rheological measurements were carried out to obtain a qualitative evaluation of the nanotubes dispersion. Indeed, the rheological properties of the melt are sensitive to the structure, particle size, shape and surface properties of the dispersed phase and thus to the dispersion. Finally, it gives an overview of the dispersion of the nanotubes at the macroscopic level that is complementary with SEM observations. Moreover, it is important to evaluate the rheological behavior in order to understand the effect of the nanotubes on internal structures and processing properties of polymer/MWNT composites.

Figure 3 represents the frequency dependence of the storage modulus (G') for the PP/MWNT and PP/MWNT/PP-g-MA nanocomposites measured at 180°C. It is apparent that storage modulus of the nanocomposites increase with increase in MWNT content. In case of PP and 1 wt% PP/MWNT nanocomposites, at low frequencies PP chains are fully relaxed and exhibit typical homopolymer-like terminal behavior. However, when the nanotube loadings reaches 2 wt%, this terminal behavior disappears and the dependence of G' on ω at low frequency is limited.

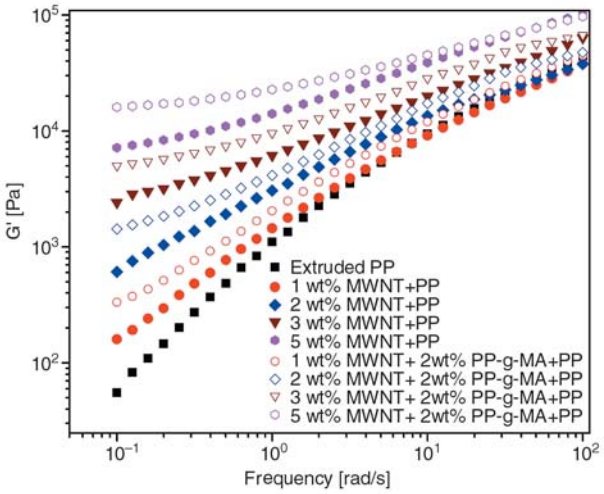

Figure 3. Storage modulus of PP/MWNT (filled symbols) and PP/MWNT/2 wt% PP-g-MA (empty symbols) nanocomposites as a function of frequency at 180°C

As shown in Figure 3, when the nanotube loading reaches 2 wt%, G' becomes less frequency dependent at low frequencies, which indicates a transition from liquid-like to solid-like viscoelastic behavior [26]. This behaviour is characteristic of non-terminal frequency behaviour. This non terminal behaviour can be attributed to the formation of an interconnected nanotube network in the polymer (so-called percolation threshold). Therefore, the solid-like (or pseudo-solid-like) behavior can be attributed to the existence of frictional interactions between the highly anisotropic particles [27, 28]. When 2 wt% of PP-g-MA is added to PP/MWNT nanocomposites, storage modulus of the composites was further increased. The rheological percolation threshold dropped from 2 wt% MWNTs (without PP-g-MA) to 1 wt% MWNTs when PP-g-MA is added to PP/MWNT composites. The results indicate that PP-g-MA would allow developing favourable interaction between PP and MWNTs, and thus, better interconnected and percolated structure of MWNTs was produced in polypropylene matrix.

In order to better identify the rheological percolation threshold, the phase angle (δ) has been plotted against the frequency (Figures 4a and 4b). Indeed, due to the formation of an interconnected network of carbon nanotubes and thus to the transition from liquid-like to solid-like behaviour, tanδ is independent of the frequency above the percolation threshold. Below the percolation threshold due to the liquid-like behaviour, the tanδ increases at low

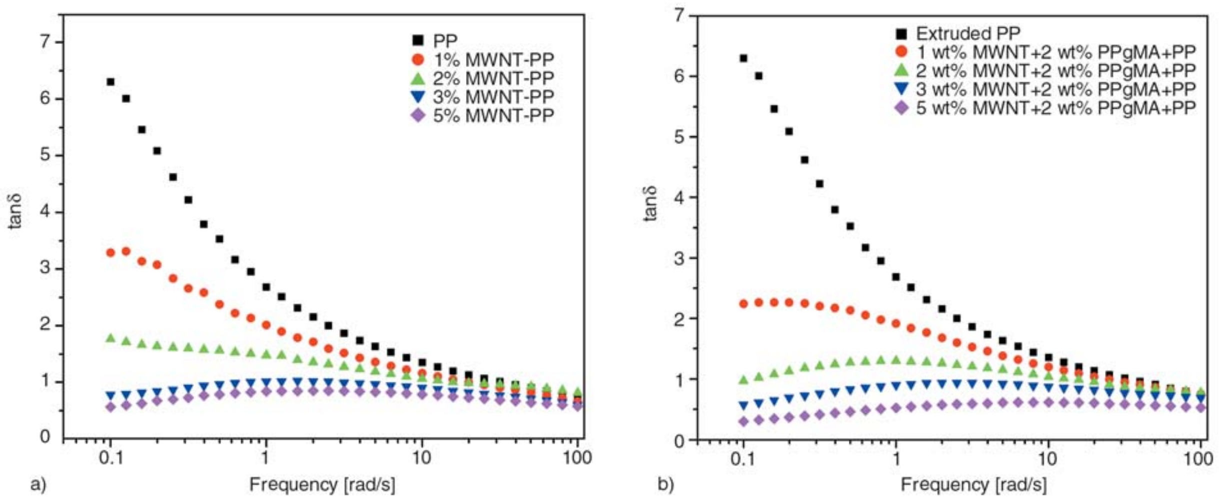

Figure 4. Phase angle (tanδ) of PP/MWNT (a) and PP/MWNT/2 wt% PP-g-MA (b) nanocomposites as a function of frequency at 180°C

frequency. Figures 4a and 4b clearly indicate that the rheological percolation threshold for the PP/MWNT composites is between 2 and 3 wt% nanotubes, whereas it is between 1 and 2 wt% for PP/MWNT/PP-g-MA composites. This decrease in percolation threshold concentration could be due to better dispersion of the nanotubes in the PP matrix thanks to PP-g-MA addition, in agreement with the SEM observations.

Logarithmic plot of G' versus G'' (Cole-Cole plot) is shown in Figure 5. Generally, Cole-Cole plot can be used as an effective method to explain structural changes occurring as a result of filler loading into a polymer matrix at a fixed temperature [29, 30]. In case of PP/MWNT nanocomposites (Figure 5a), this plot deviates from that of the PP matrix when the nanotube content is 2 wt% in PP matrix. However, in case of PP/MWNT/PP-g-MA nanocomposites (Figure 5b), the deviation from PP is already observed at 1 wt% nanotube. These observations indicate a structural change on the addition of nanotubes into polymer matrix. Further, these structural changes are more prominent in PP-g-MA bearing nanocomposites, showing a larger degree of deviation and thus a better dispersion. This is due to the fact that, addition of PP-g-MA into highly concentrated PP/MWNT masterbatches, increases the interfacial interaction between PP and MWNTs. The better wettability of the PP-g-MA coated nanotubes tends to favour the disentanglement of the bundles and promotes the dispersion of individual nanotubes limiting the remaining nanotubes aggregates. The increasing amount of well-dispersed individual nanotubes thus allows to decrease the percolation threshold.

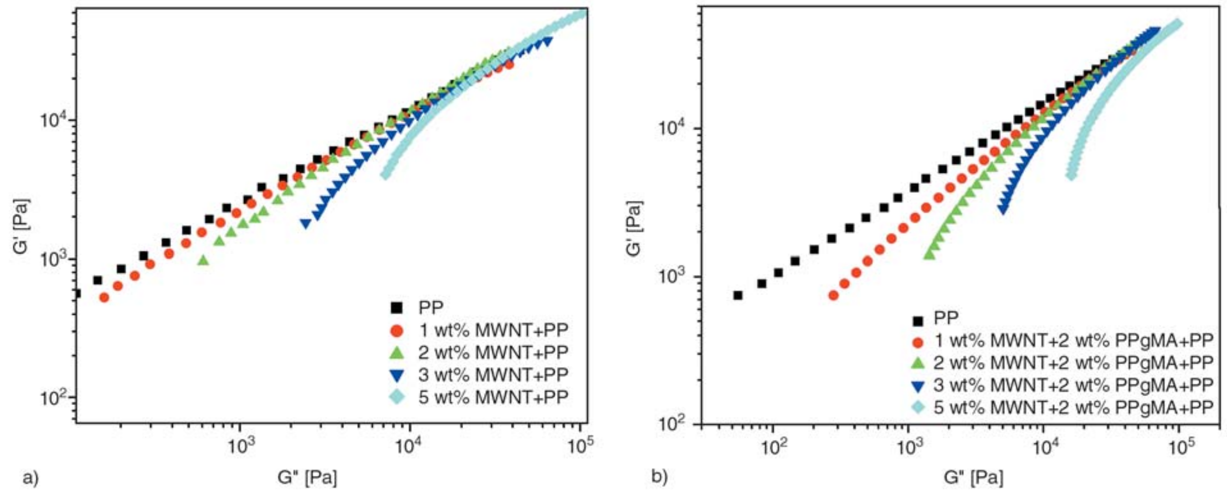

Figure 5. Cole-Cole plot for PP/MWNT (a) and PP/MWNT/2 wt% PP-g-MA (b) nanocomposites

3.4. Mechanical characterization

The variation of tensile strength, modulus and elongation at break with MWNTs content for the PP/MWNT and PP/MWNT/2 wt% PP-g-MA composites are shown in Figure 6. It is obvious that Young's modulus (Figure 6a) and yield stress (Figure 6b) of PP/MWNT/PP-g-MA composites are higher than those of PP/MWNT composites, and tends to increase substantially with the MWNTs content in composites. It is now well-known and commonly admitted that the mechanical properties of polymer nanocomposites, especially the modulus, depend to a great extent on filler dispersion and interfacial interaction, and are increased only when good dispersion of the nanofiller and effective stress transfer at the polymer/filler interface are guaranteed. Indeed increasing the interfacial properties increases the volume of polymer chains influenced. The improvement of the dispersion also increases the average aspect ratio of the nanofillers in the polymer matrix and as a consequence tensile properties are improved as already reported [31] for clay platelets. Here apparently, MWNTs are able to reinforce the PP matrix due to their large aspect ratio combined with high mechanical properties. Incorporation of PP-g-MA into PP/MWNT, further increases the Young's modulus (Figure 6a) and yield stress (Figure 6b) of PP/MWNT/2 wt% PP-g-MA composites when compared to PP/MWNT nanocomposites. When PP-g-MA was added as compatibilizer, the tensile modulus of the composites treated with PP-g-MA increased on average 10% compared with the composite without PP-g-MA. The effect of the PP-g-MA was even more pronounced in tensile yield stress (Figure 6b), where an average improvement of 35% was

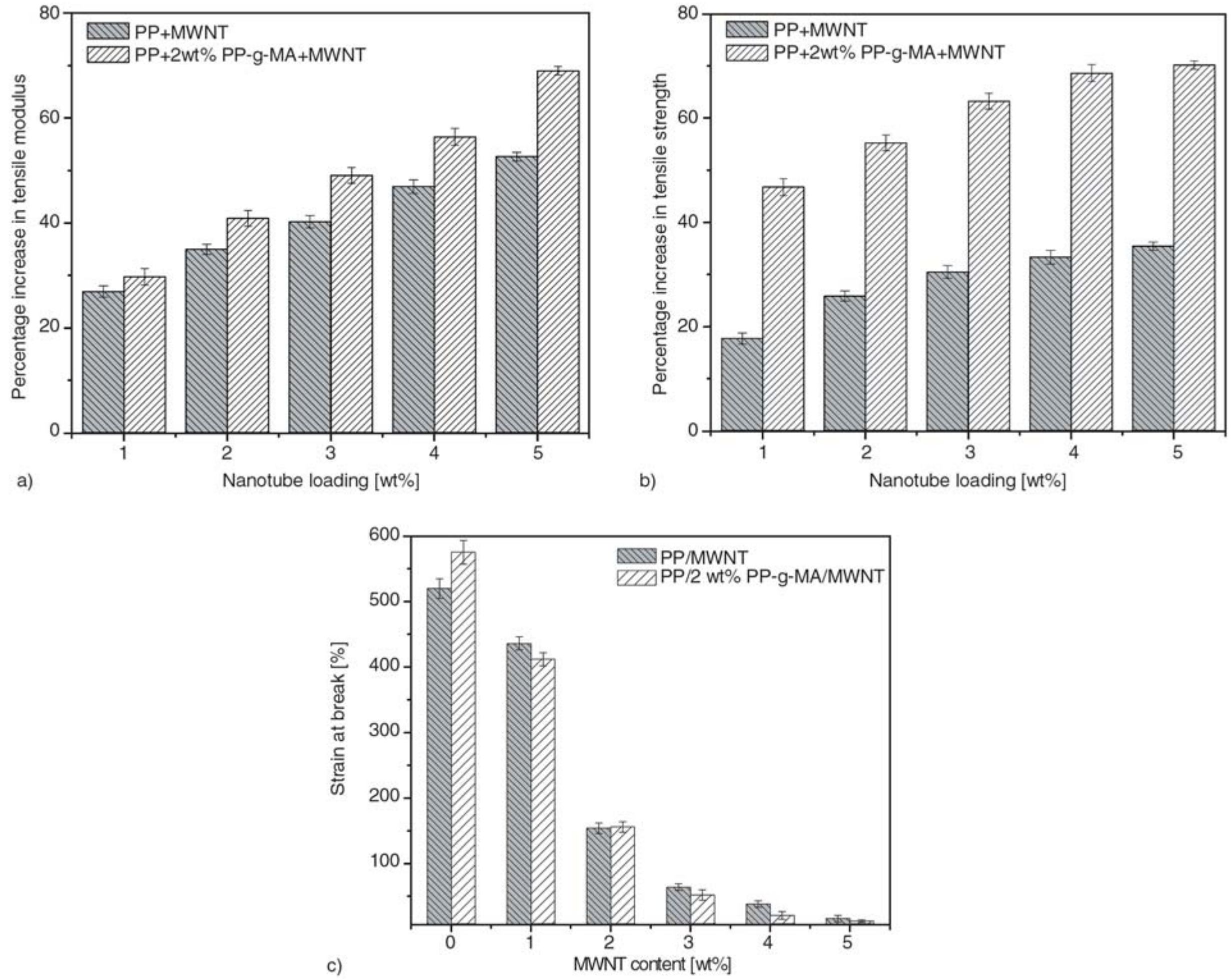

Figure 6. Percentage increase in tensile modulus with respect to PP and PP-g-MA as a function of MWNT content for the PP/MWNT and PP/MWNT/2 wt% PP-g-MA composites (a). Percentage increase in tensile strength with respect to PP and PP-g-MA as a function of MWNT content for the PP/MWNT and PP/MWNT/2 wt% PP-g-MA composites (b). Variation of percentage strain at break with MWNT content for the PP/MWNT and PP/MWNT/2 wt% PP-g-MA composites (c).

observed. The increase of the modulus is due to the fact that PP-g-MA improves the dispersion of MWNTs in PP matrix and thus the aspect ratio and the carbon nanotubes/PP interface. On the other hand, PP-g-MA due to the wrapping of nanotubes modifies drastically the interface leading to the interfacial interaction enhancement and thus promotes a better stress transfer between MWNTs and PP matrix. The number and the size of the nanotubes aggregates is also reduced leading to a better tensile strength. In the case of PP/MWNT composites the aggregates act as stress concentrators easing the plastic deformation thus decreasing the yield stress. Finally, due to few aggregates and better interface, the yield stress is increased when PP-g-MA is added. In spite of the better dispersion of MWNTs to PP matrix thanks to PP-g-MA, elongation at break decreases with increase in MWNT content (Figure 6c). This is probably due to the presence of few masterbatch aggregates.

The flexural strength and modulus of PP/MWNT and PP/MWNT/2 wt% PP-g-MA nanocomposites are shown in Figure 7. It can be seen that the bending properties of PP/MWNT nanocomposites increased with increasing nanotube content up to a content of 2 wt% of MWNT, but decreases after 3 wt%. Such a decrease in flexural properties at higher nanotube loading may probably be due to the fact that, the nanotubes formed a cluster or agglomerate among themselves, resulting in a filler-filler interaction and a poor interface between MWNTs and PP matrix. However, on addition of 2 wt% PP-g-MA to PP/MWNT masterbatch, flexural properties of the composites are increased with increase in nanotube content. This may be related to the more uniform dispersion of nanotubes in the PP matrix, leading to better interfacial properties. These results also indicate an effective usage of PP-g-MA to assist the dispersion of nanotubes as supported by rheological measurements.

Finally, Figure 8 shows the impact properties of notched (Figure 8a) and un-notched (Figure 8b) samples of PP/MWNT and PP/MWNT/2 wt% PP-g-MA composites. Charpy impact strength of the notched specimens (Figure 8a) slightly increased as the MWNTs content increased up to 2 wt% for PP/MWNT nanocomposites and up to 3 wt% in case of PP/MWNT/2 wt% PP-g-MA nanocomposites. This increase is significantly larger for the samples with PP-g-MA. This is due to the fact that notched impact behavior is controlled to a greater extent by factors affecting the propagation of fracture initiated due to stress concentration at the notch tip. Lowering of impact energy at higher nanotube content is due to the presence few master-

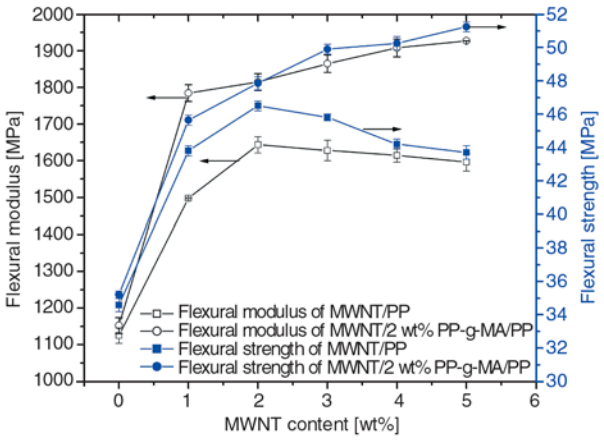

Figure 7. Flexural strength and modulus of PP/MWNT and PP/MWNT/2 wt% PP-g-MA nanocomposites

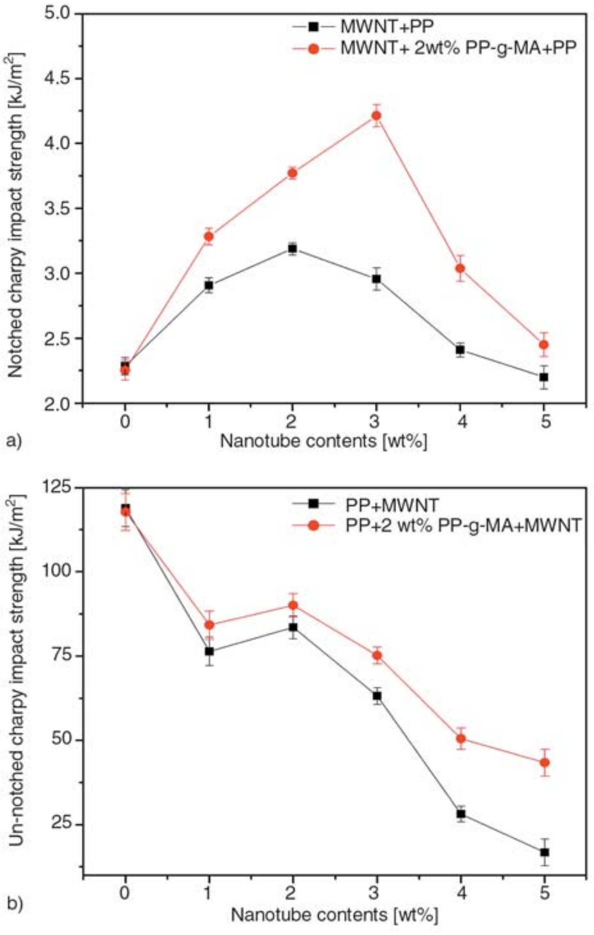

Figure 8. Impact properties PP/MWNT (a) and PP/MWNT/2 wt% PP-g-MA (b) nanocomposites

batch aggregates in the composites. However, impact strength of the un-notched samples decreases with increase in MWNTs content in both the systems (Figure 8b). The decrease of impact energy in PP-g-MA bearing nanocomposites is nevertheless lower when compared to composites without PP-g-MA. This is due to the effect of PP-g-MA during processing, leading to better dispersion of nanotubes in PP matrix. This observation is in contradiction with the results obtained for the elongation at break for which the composites based on PP-g-MA are slightly more brittle. This apparent contradiction between effects of PP-g-MA on the elongation at break and on the impact strength values may be due to the differences in the deformation rate involved in the two types of experiments. Tensile testing involves high deformation, while impact strength is determined by local cracking. The detrimental effects of low molecular PP-g-MA are more pronounced when measuring elongation at break at low rate.

4. Conclusions

Multi-wall carbon nanotubes (MWNTs) filled polypropylene (PP) nanocomposites were prepared by melt compounding via masterbatch dilution technique. Polypropylene grafted maleic anhydride (PP-g-MA) was added to promote the carbon nanotubes dispersion.

The morphological characterization based on scanning electron microscopy has confirmed that nanotubes are distributed uniformly indicating a good dispersion of nanotubes in the PP/PP-g-MA matrix compared to pure PP. Thus, the results indicated that PP-g-MA is an effective dispersing agent for MWNTs based masterbatches in PP/MWNT nanocomposites. It is assumed that PP-g-MA promotes the dispersion thanks the enhanced interaction between MWNTs and PP due to wrapping of PP-g-MA on MWNTs.

The rheological characterization has shown that, when PP-g-MA is added to PP/ MWNT nanocomposites, dynamic moduli and viscosity further increase. Liquid to solid transition takes place at a MWNTs content just above 1 wt%, indicating a percolated network structure in the material, which appears earlier than for PP/MWNT without PP-g-MA (transition at about 2 wt% in that case).

The mechanical characterization has shown that both the tensile and bending moduli and strengths of the nanocomposites increase by the addition of nanotubes, and the addition of PP-g-MA further improves these properties. An issue, which needs to be further investigated, is however that tensile elongation at break decreases with the addition of PP-g-MA. Regarding impact properties, the Charpy impact strength increases, passes through a maximum and then decreases for notched samples, whereas for un-notched samples, a decrease is observed with the addition of MWNTs due to the presence of nanotubes aggregates. Nevertheless, the addition of 2 wt% PP-g-MA to the composites tends to improve these impact properties.

In conclusion, it has been demonstrated that the use of PP-g-MA is a way to promote a better dispersion of carbon nanotubes in a PP matrix, and thus better mechanical properties and lower rheological percolation threshold. Moreover the possibility to coat the nanotubes with PP-g-MA directly in the extruder is a very promising way to promote, in-situ during the extrusion, the disentanglement of the carbon nanotubes. This technique may be extend to other matrices by changing the type of compatibilizer.

Furthermore, these results reveal that diluting thermoplastics/MWNTs masterbatches to manufacture plastic parts is a very promising route. Such a route allows keeping the functional benefits of well-dispersed MWNTs, whereas limiting the handling difficulties in plastics processing industrial workshops.

Acknowledgements

The authors are grateful for the financial support granted by Conseil Regional, Nord-Pas-de-Calais, France. Thanks are also due to Nanocyl SA. (Belgium) for providing the MWNTs masterbatch.

References

[1] Valentino O., Sarno M., Rainone N. G., Nobile M. R., Ciambelli P., Neitzert H. C., Simon G. P.: Influence of the polymer structure and nanotube concentration on the conductivity and rheological properties of polyethylene/CNT composites. Physica E: Low-dimensional Systems and Nanostructures, **40**, 2440–2445 (2008).

[2] Bikiaris D., Vassiliou A., Chrissafis K., Paraskevopoulos K. M., Jannakoudakis A., Docoslis A.: Effect of acid-treated multi wall carbon nanotubes on the mechanical, permeability, thermal properties and thermo-oxidative stability of isotactic polypropylene. Polymer Degradation and Stability, **93**, 952–967 (2008).

[3] Ganß M., Satapathy B. K., Thunga M., Weidisch R., Pötschke P., Jehnichen D.: Structural interpretations of deformation and fracture behavior of polypropylene/multi-walled carbon nanotube composites. Acta Materialia, **56**, 2247–2261 (2008).

[4] Qian D., Dickey E. C., Andrews R., Rantell T.: Load transfer and deformation mechanisms in carbon nanotube-polystyrene composites. Applied Physics Letters, **76**, 2868–2870 (2000).

[5] Jin L., Bower C., Zhou O.: Alignment of carbon nanotubes in a polymer matrix by mechanical stretching. Applied Physics Letters, **73**, 1197–1199 (1998).

[6] Zeng J., Saltysiak B., Johnson W. S., Schiraldi D. A., Kumar S.: Processing and properties of poly(methyl methacrylate)/carbon nano fiber composites. Composites Part B: Engineering, **35**, 173–178 (2004).

[7] Li C., Pang X-J., Yu Z-L.: Study on polycarbonate/multi walled carbon nanotubes composites produced by melt processing. Materials Science and Engineering: A, **457**, 287–291 (2007).

[8] Chae H. G., Sreekumar T. V., Uchida T., Kumar S.: A comparison of reinforcement efficiency of various types of carbon nanotubes in polyacrylonitrile fiber. Polymer, **46**, 10925–10935 (2005).

[9] Zhang X., Liu T., Sreekumar T. V., Kumar S., Hu X., Smith K.: Gel spinning of PVA/SWNT composite fiber. Polymer, **45**, 8801–8807 (2004).

[10] McIntosh D., Khabashesku V. N., Barrera E. V.: Nano-composite fiber systems processed from fluorinated single-walled carbon nanotubes and polypropylene matrix. Chemistry of Materials, **18**, 4561–4569 (2006).

[11] McIntosh D., Khabashesku V. N., Barrera E. V.: Benzoyl peroxide initiated in-situ functionalization, processing and mechanical properties of single-walled carbon nanotube-polypropylene composite fibers. Journal of Physical Chemistry C, **111**, 1592–1600 (2007).

[12] Zhou Z., Wang S., Lu L., Zhang Y., Zhang Y.: Isothermal crystallization kinetics of polypropylene with silane functionalized multi-walled carbon nanotubes. Journal of Polymer Science Part B: Polymer Physics, **45**, 1616–1624 (2007).

[13] Vaisman L., Marom G., Wagner H. D.: Dispersions of surface-modified carbon nanotubes in water-soluble and water-insoluble polymers. Advanced Functional Materials, **16**, 357–363 (2006).

[14] López Manchado M. A., Valentini L., Biagiotti J., Kenny J. M.: Thermal and mechanical properties of single-walled carbon nanotubes-polypropylene composites prepared by melt processing. Carbon, **43**, 1499–1505 (2005).

[15] Xiao Y., Zhang X., Cao W., Wang K., Tan H., Zhang Q.: Dispersion and mechanical properties of polypropylene/multiwall carbon nanotubes composites obtained via dynamic packing injection molding. Journal of Applied Polymer Science, **104**, 1880–1886 (2007).

[16] Shi D., Lian J., He P., Wang L. M., Xiao F., Yang L., Schultz M. J., Mast D. B.: Plasma coating of carbon nanofibers for enhanced dispersion and interfacial bonding in polymer composites. Applied Physics Letters, **83**, 5301–5303 (2003).

[17] Kelarakis A., Yoon K., Sics I., Somani R. H., Chen X., Hsiao B. S.: Shear-induced orientation and structure development in isotactic polypropylene melt containing modified carbon nanofibers. Journal of Macromolecular Science, Part B: Physics, **45**, 247–261 (2006).

[18] Zhou X., Xie X., Zeng F., Li R. K-Y., Mai Y-W.: Properties of polypropylene/carbon nanotube composites compatibilized by maleic anhydride grafted SEBS. Key Engineering Materials, **312**, 223–228 (2006).

[19] Tjong S. C., Liang G. D., Bao S. P.: Electrical behavior of polypropylene/multiwalled carbon nanotube nanocomposites with low percolation threshold. Scripta Materialia, **57**, 461–464 (2007).

[20] Jiang X., Bin Y., Kikyotani N., Matsuo M.: Thermal, electrical and mechanical properties of ultra-high molecular weight polypropylene and carbon filler composites. Polymer Journal, **38**, 419–431 (2006).

[21] Lee S. H., Cho E. N. R., Jeon S. H., Youn J. R.: Rheological and electrical properties of polypropylene composites containing functionalized multi-walled carbon nanotubes and compatibilizers. Carbon, **45**, 2810–2822 (2007).

[22] Lee G-W., Jagannathan S., Chae H. G., Minus M. L., Kumar S.: Carbon nanotube dispersion and exfoliation in polypropylene and structure and properties of the resulting composites. Polymer, **49**, 1831–1840 (2008).

[23] Prashantha K., Soulestin J., Lacrampe M. F., Krawczak P., Dupin G., Claes M.: Compounding of masterbatch-based multi-walled carbon nanotube filled polypropylene nanocomposites: Assessment of rheological and mechanical properties. in 'Proceedings of the 8th International Seminar on Experiment Techniques and Design in Composites Materials. Cagliari, Italy' 38–40 (2007).

[24] Ganß M., Satapathy B. K., Thunga M., Weidisch R., Pötschke P., Jehnichen D.: Structural interpretations of deformation and fracture behaviour of polypropylene/multi-walled carbon nanotube composites. Acta Materialia, **56**, 2247–2261 (2008).

[25] Bao S. P., Tjong S. S.: Mechanical behaviours of polypropylene/carbon nanotube nanocomposites: The effects of loading rate and temperature. Material Science and Engineering A, **485**, 508–516 (2007).

[26] Seo M-K., Park S-J.: Electrical resistivity and rheological behaviors of carbon nanotubes-filled polypropylene composites. Chemical Physics Letters, **395**, 44–48 (2004).

[27] Pötschke P., Fornes T. D., Paul D. R.: Rheological behavior of multiwalled carbon nanotube/polycarbonate composites. Polymer, **43**, 3247–3255 (2002).

[28] Abdel-Goad M., Pötschke P., Zhou D., Mark J. E., Heinrich G. J.: Preparation and rheological characterization of polymer nanocomposites based on expanded graphite. Journal of Macromolecular Science, Part A: Pure and Applied Chemistry, **44**, 591–598 (2007).

[29] Choi J. S., Lim S. T., Choi H. J., Pozsgay A., Százdi L., Pukánszky B.: Viscoelastic properties of exfoliated polyamide-6/layered silicate nanocomposite. Journal of Material Science, **41**, 1843–1846 (2006).

[30] Chae D. W., Lee K. H., Kim B. C.: Rheological properties of ferrite nanocomposites based on nylon-66. Journal of Polymer Science Part B: Polymer Physics, **44**, 371–377 (2006).

[31] Kojima Y., Usuki A., Kawasumi M., Okada A., Kurauchi T., Kamigaito O.: Synthesis of nylon 6-clay hybrid by montmorillonite intercalated with ε-caprolactam. Journal of Polymer Science Part A: Polymer Chemistry, **31**, 983–986 (1993).

eXPRESS Polymer Letters Vol.2, No.10 (2008) 746–756
Available online at www.expresspolymlett.com
DOI: 10.3144/expresspolymlett.2008.88

Nanofilled and/or toughened POM composites produced by water-mediated melt compounding: Structure and mechanical properties

S. Siengchin[1], *J. Karger-Kocsis*[1*], *R. Thomann*[2]

[1]Institute for Composite Materials (Institut für Verbundwerkstoffe GmbH), University of Kaiserslautern, Erwin-Schrödinger-Str. 58, D-67663 Kaiserslautern, Germany
[2]Institut für Makromolekulare Chemie und Freiburger Materialforschungszentrum, Albert-Ludwigs-Universität Freiburg, Stefan-Meier-Str. 31, D-79104 Freiburg, Germany

Received 16 August 2008; accepted in revised form 18 September 2008

Abstract. Binary and ternary composites composed of polyoxymethylene (POM), polyurethane (PU) and synthetic boehmite alumina (AlO(OH)) were produced by water-mediated melt compounding technique. PU latex and/or aqueous alumina suspension were injected into the molten POM in a twin-screw extruder to prepare toughened and/or reinforced polymer composites. The dispersion of the alumina and PU was studied by transmission- and scanning electron microcopy techniques (TEM and SEM, respectively), and discussed. The crystallization of the POM-based systems was inspected by polarized optical microscopy (PLM). The mechanical and thermomechanical properties of the composites were determined in dynamic-mechanical thermal analysis (DMTA), short-time creep tests (performed at various temperatures), uniaxial static tensile and notched Charpy impact tests. Incorporation of alumina increased the stiffness and resistance to creep and reduced the tensile strength, elongation at break and impact toughness. The change in the above parameters was opposite for the POM/PU binary blends. Additional incorporation of alumina in the POM/PU blend enhanced the resistance to creep, elongation at break and maintained the impact toughness compared to the POM/PU blend.

Keywords: *polymer composites, polymer blends and alloys, processing technologies, mechanical properties, polyoxymethylene (POM)*

1. Introduction

Nanotechnology is now recognized as one of the most promising areas for technological development in the 21st century. The development of polymer nanocomposites is rapidly emerging fuelled by potential applications in different industry sectors. Nanocomposites belong to class of composites containing dispersed particles in the nanometer range (at least in one dimension). In the related area thermoplastic polymer-based nanocomposites have attracted considerable interest because they often exhibit remarkable property improvements when compared with those of neat polymers or conventional microcomposites.

To prepare thermoplastic polymer nanocomposites different methods have been followed, such as *in-situ* polymerization, melt blending and solution/dispersion techniques (e.g. [1]). It was early noticed that the preparation technique of the nanocomposites has a strong impact on the dispersion of the nanoparticles. The use of conventional melt compounding techniques to prepare nanocomposites is usually more practical and economical than in situ polymerization. For that purpose common polymer

---

[*]Corresponding author, e-mail: karger@pt.bme.hu

processing equipments, such as extruders and internal mixers are well suited. The shear forces, accommodated in the melt during processing may also be helpful to support the dispersion of the filler. However, melt shearing is not always enough to break up large agglomerates and thus the resulting filler dispersion may remain further on poor. An alternative way to prepare composite materials is the latex polymerization and compounding (e.g. [2–4]). Latex compounding is a promising route compared, for example, to *in-situ* polymerization and solution techniques. It is becoming more and more important because of the following benefits. First, many polymers are available in latex form. Second, latex can be introduced in the polymer melt during compounding on line. Note that in an aqueous polymer latex submicron-sized solid polymer particles are suspended in water. When combined with nanosized fillers, the polymer particles and the filler may create a peculiar segregated network. The corresponding material, after drying and 'hot compaction', may show excellent properties at very low filler concentration [3–6] compared to a melt blended version containing the same polymer and filler. The advantage of this latex compounding process is that the expensive chemical modification of the fillers can be avoided if the filler is itself water swellable or dispersible [7]. Moreover, a polymer latex containing well dispersed nanoparticles can be used as a masterbatch (in both dry and liquid forms) for subsequent melt compounding.

Among the water dispersible commercially available nanofillers, natural and synthetic layered silicates, carbon nanotubes, boehmite alumina (AlO(OH)), should be mentioned [7]. To produce nanocomposites using aqueous dispersions, slurries is not only an affordable method (no organophilic modification is needed for the fillers) but associated also with reduced health hazard. Indeed, the particles when introduced are in micron range and become nano-scaled only in the aqueous media. In the follow-up steps (coagulation, drying etc.) the nanoparticles are already embedded in the polymer which guarantees easy handling and minimized health risk.

Water-mediated melt compounding techniques to disperse various nano- and microfillers were already tried for various thermoplastic systems, such as polypropylene and clay [8], low density polyethylene and cellulose [9]. However, the use of latices to produce nanofiller containing masterbatches for subsequent melt compounding has received far less attention up to now [10, 11].

The present work addresses the toughening and reinforcement of polyoxymethylene (POM) via a water-mediated melt compounding technique which allows producing nanocomposites with additional toughening. It is noteworthy that thermoplastic polymers having low resistance to hygrothermal decomposition, like linear polyesters, are not suited for WM-CT. On the other hand, POM is fairly stable against hydrolysis and at the same time requires relatively low processing temperatures. Polyurethane (PU) was selected as toughening agent for POM according to the state-of-art (e.g. [12, 13]). It was used in its latex form. It is noteworthy that the mean size of rubber latices is closely matched with that of conventional toughening agents, impact modifiers. Synthetic boehmite alumina was used as nanofiller. One of the criteria for selecting this filler was that it is water dispersible and thus its nanoscale dispersion can be achieved also in aqueous polymer latex. On the other hand, it was reported that this boehmite alumina can be well dispersed by melt compounding without water as carrier, as well [14].

2. Experimental

2.1. Materials and preparation of composites

Water dispersible boehmite alumina (AlO(OH)); Dispal®11N7-80 of Sasol GmbH, Hamburg, Germany) served as filler. Its characteristics are as follow: Al_2O_3 content: 80 wt%, specific surface area: 100 m^2/g, mean dispersed particle size in water: 220 nm. PU latex with 50 wt% dry content (Acralen U 550) which has the particles in the size range 100 to 1000 nm (according to suppliers' information), was kindly supplied by Polymer Latex GmbH (Marl, Germany). Granulated POM (Hostaform C 9021, Ticona GmbH, Frankfurt, Germany) was utilized as polymeric matrix for all composite systems. Its volumetric melt flow rate (MVR at 190°C/2.16 kg) was 8 cm^3/10 min.

POM/PU, POM/alumina binary and POM/PU/alumina ternary nanocomposites were prepared by water mediated-continuous technique (WM-CT) in a twin-screw extruder. For the compounding of the composites a special mixing screw of the co-rotating ZSK 25 P8 extruder (Werner & Pfleiderer,

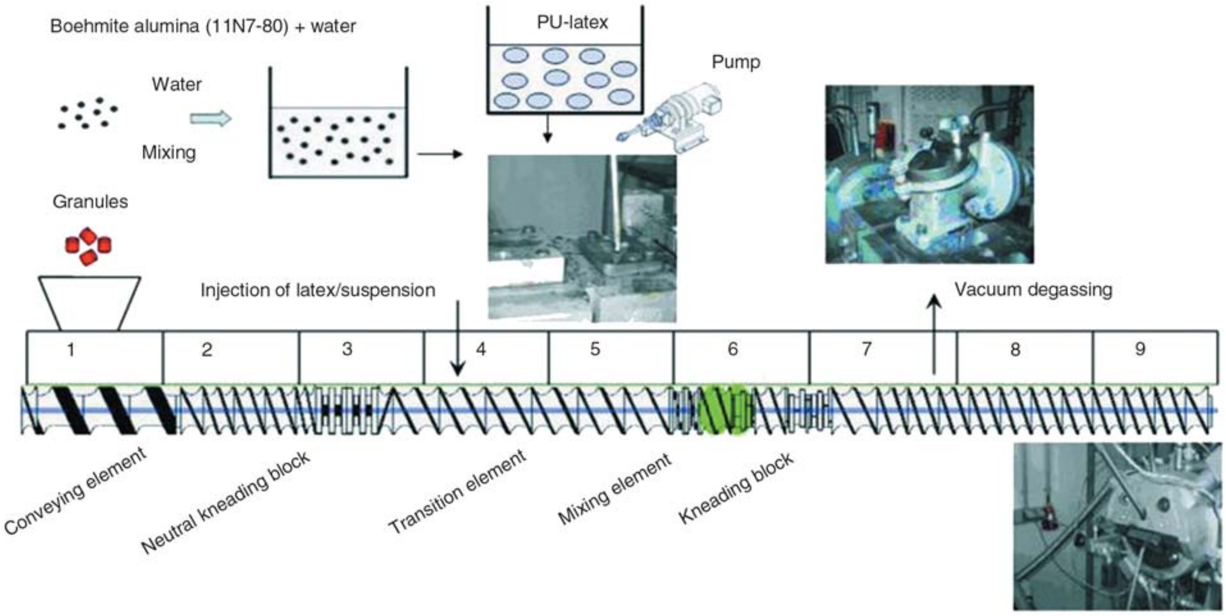

Figure 1. Screw configuration and barrel sections of the corotating twin-screw extruder used

Table 1. Recipe and designation of the POM-based systems

Sample designation	PU content [wt%]	11N7-80 alumina content [wt%]
POM	–	–
POM/PU(10)	10	–
POM/11N7-80(3)	–	3
POM/PU(10)/11N7-80(3)	10	3

Stuttgart, Germany) was used. The design of the screw with a length-to-diameter ratio of 36 is given in Figure 1.

The alumina particles were dispersed in water at ambient temperature under continuous mechanical stirring for 30 minutes to obtain an aqueous alumina slurry, in which the alumina content was 30 wt%. The rubber particle and/or alumina contents in the binary and ternary composites were set for 10 and 3 wt%, respectively. The POM based composites were compounded at an output rate of ca.10 kg/h by setting the barrel temperatures between 150 (section 1) and 190°C (from section 2 to 9 according to Figure 1). PU latex and aqueous alumina slurry were injected into the extruder at a rate of 2 l/h, 1 l/h, respectively, using one (binary composites) or two pumps (ternary composites). Type of the pumps was Nemo® Pumpe (Netzsch, Waldkraiburg, Germany). The composites produced are listed in Table 1.

Injection molding process

The granulated materials were injection molded into standard dumbbell-shaped specimens (160×10×4 mm^3 length × width × thickness, according to the DIN-ISO-527 standard) by an automatic injection molding machine (Alburg Allrounder 320S, Lossburg, Germany). The barrel temperature of the injection molding machine was set at 200°C and that of the mold at 90°C. The injection pressure was kept constant (700 bar) and for the injection speed of 55 cm^3/s was selected. For the cooling time 20 s was chosen.

2.2. Characterization and testing

2.2.1. Morphology detection

The dispersion of alumina in the POM nanocomposites was studied by transmission and scanning electron microscopy techniques (TEM and SEM, respectively). TEM measurements were carried out with a Zeiss LEO 912 Omega transmission electron microscopic (Oberkochen, Germany) applying an acceleration voltage of 120 kV. Thin sections (ca. 50 nm) were cut at room temperature with a Diatome diamond knife (Hatfield, PA, USA) using an Ultracut E microtome (Reichert and Jung, Vienna, Austria).

The fracture surfaces of tensile loaded specimens were subjected to SEM inspection in a Supra™ 40VP SEM (Carl Zeiss GmbH, Oberkochen, Germany). The surface was carbon coated prior to SEM inspection performed at low acceleration voltage (3 kV).

2.2.2. Crystallization and melting properties

The spherulite growth was observed by polarized light microscopy (PLM). Samples were isothermally crystallized in a hot stage (THMS 600/S, Raczek Analysentechnik, Wedemark, Germany). Thin films of the materials with a thickness of 20–30 microns were used. The film was melted at 200°C for 1 min and then cooled to the isothermal crystallization temperature ($T = 148°C$) where it was hold for 60 min.

2.2.3. Thermo-mechanical properties

Dynamic mechanical analysis (DMA) was made in tensile mode at 1 Hz frequency using a DMA Q800 apparatus (TA Instruments, New Castle, NJ, USA). The storage- and loss moduli (E', E'') along with mechanical loss factor (tanδ) were determined as a function of the temperature ($T = –100…+150°C$). The strain applied was 0.1% and the heating rate was set for 3°C/min. The specimen was a dumbbell-shaped type (S3A according to DIN 53504).

2.2.4. Mechanical response

Short time creep tests were made in tensile mode at different temperatures using the above DMA apparatus. The creep compliance were determined as a function of the time (t_{creep} = 60 min). The applied tensile stress was 6 MPa (at 0.35% strain). This was derived from a test series checking the presence of linear isochronous deformation. The creep tests were performed on dumbbell-shaped specimens (5B type according to DIN-EN ISO 527) by considering their rectangular section.

The temperature dependence of the creep response of the POM and its composites was studied in the range from –50 to 80°C. Isothermal tests were run on the same specimen in the above temperature range by increasing the temperature stepwise by 5°C and equilibrating the specimen at each temperature for 5 min. During the isothermal tests the duration of the creep testing was 15 min.

Tensile tests were performed on dumbbell-shaped specimens (DIN-ISO-527) on a Zwick 1474 (Ulm,

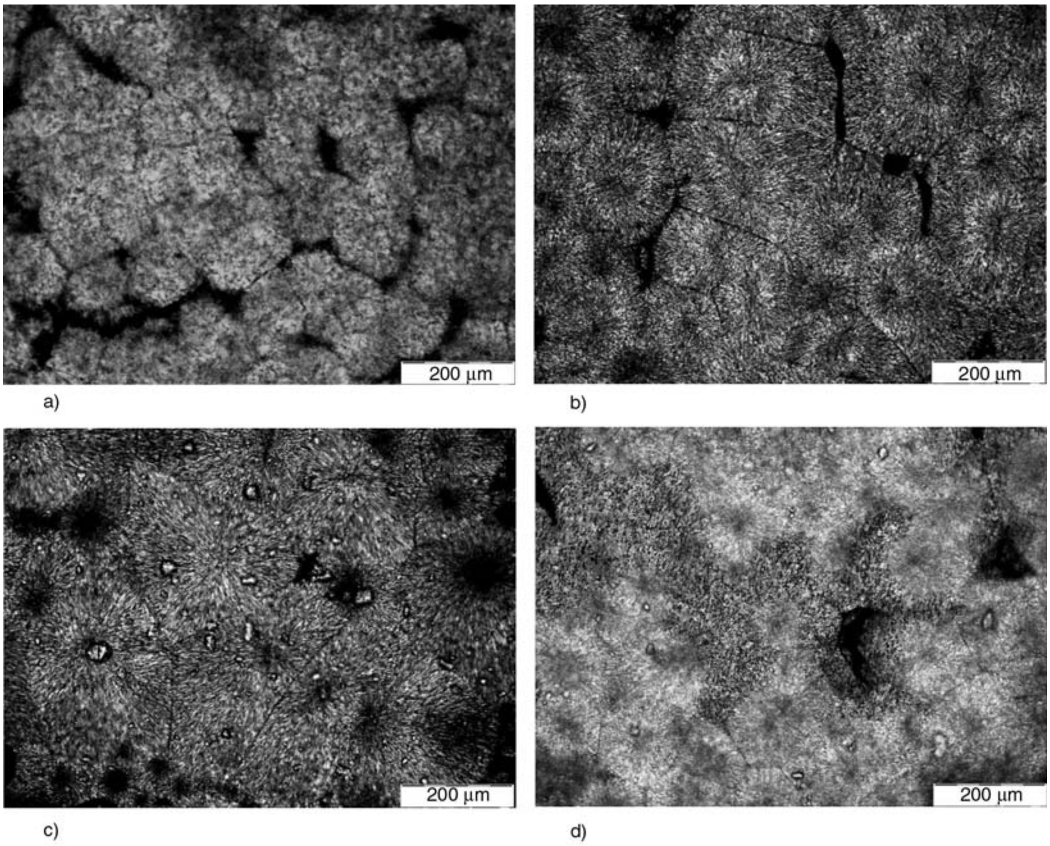

Figure 2. PLM pictures taken of the isothermally crystallized POM (a), POM/PU blend (b), POM/alumina (c) and POM/PU/alumina composites (d)

Germany) universal testing machine. Tests were run at room temperature at v = 2 mm/min crosshead speed and the related stress-strain curves were registered.

Impact tests were performed on an instrumented impact tester (AFS-MK4 fractoscope of Ceast, Torino, Italy) according to the standard ISO 179. Striker energy of 4 J, acquisition time of 4~8 ms, and incident impact velocity of 2.9 m/s were set. The specimens were notched rectangular bars (80×10×4 mm^3, length × width × thickness) with a notch depth of 1 mm (notch tip radius 0.1 mm). Measurements were run at ambient temperature on at least six specimens.

3. Results and discussion

3.1. Morphology detection

Figures 2a–2d compare the spherulitic structures of POM, POM/PU blend, POM/alumina binary and POM/PU/alumina ternary composites produced by WM-CT. The spherulite size of POM does not change much with the composition. On the other hand, the build-up of spherulites becomes disturbed by adding PU. Considering additional differential scanning calorimetric results (not reported here) one can conclude that the crystalline structure of POM was not changed by incorporating the alumina slurry or PU latex via the water-mediated technique used.

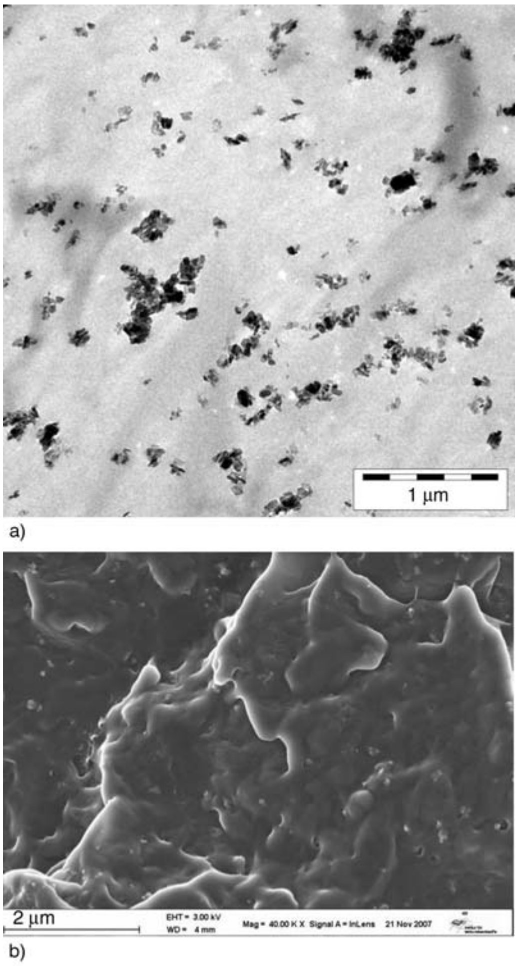

Figure 3. Dispersion of alumina in the POM/alumina composite based on TEM (a) and SEM (b) investigations

TEM and SEM pictures taken of the POM/alumina composites, POM/PU blend and POM/PU/alumina ternary composites are shown in Figures 3, 4 and 5, respectively. SEM pictures taken from the fracture surfaces of tensile loaded specimens give further insight in the dispersion state of the alumina and PU. This is due to the larger view-field in SEM compared to TEM. Figures 3a and 3b show that the alumina particles are nanoscaled and homogeneously dispersed in the matrix, in fact. Figures 4a and 4b demonstrate that the PU rubber particles are

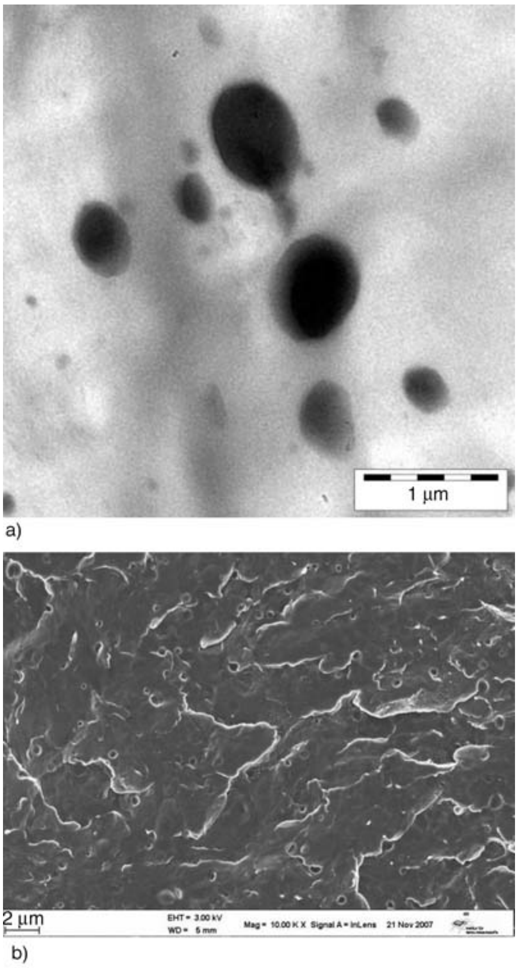

Figure 4. Dispersion of PU in the POM/PU blend based on TEM (a) and SEM (b) investigations

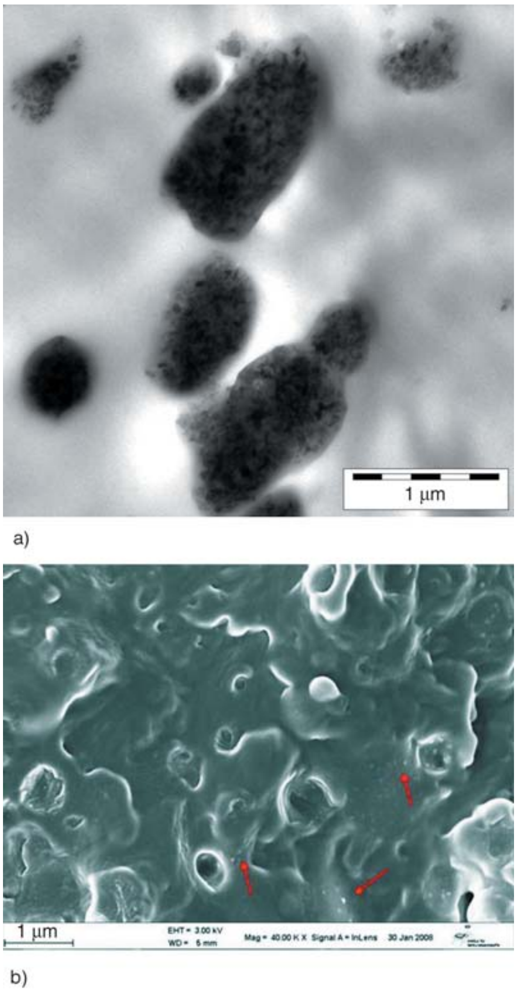

Figure 5. Dispersion of PU and alumina in the POM/PU/alumina system based on TEM (a) and SEM (b) investigations

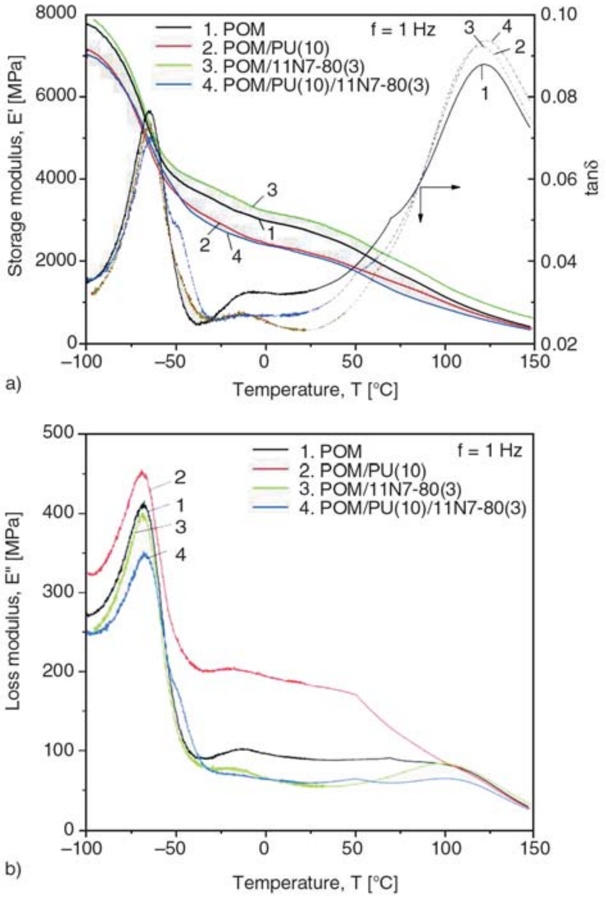

Figure 6. E' and tanδ vs. T (a) and E'' vs. T (b) traces for the POM systems prepared by WM-CT

also well dispersed in the POM matrix. The mean diameter of the PU is between 700 and 900 nm, which is closely matched with the initial size of the PU particles in the corresponding latex. The above mentioned results support the effective dispersion of the alumina and rubber particles in nanoscale range using the WM-CT. Note that the dispersed PU particle size in a POM/PU blend produced discontinuously was clearly larger compared to the present on-line technique [15]. In the POM/PU/alumina ternary composites (cf. Figure 5a) the alumina particles are mainly in the PU phase. On the other hand, dispersed alumina particles can also be found in the POM matrix based on SEM (cf. particles indicted by arrows in Figure 5b).

3.2. DMTA response

The storage modulus (E'), tanδ and loss modulus (E'') as a function of temperature are shown for the systems studied in Figures 6a and 6b, respectively. It can be seen from Figure 6a that the modulus E' of POM systems decreases with increasing temperature and the stiffness of the POM/PU blend was lower than the POM. However, the incorporation of alumina particles resulted in some increase in the storage modulus in the whole temperature range, compared to that of the pure POM. This can be well explained by reinforcing effect of alumina particles leading to an increased stiffness. Figure 6b also shows that the blend containing 10 wt% of PU exhibits markedly higher loss modulus than the other systems. This is due to the rubbery character of the incorporated PU.

3.3. Creep behavior

Short-term creep

Figures 7 displays the traces of the creep compliance and its simulated value using the Burgers model (e.g. [16–18]), as a function of time at T = 30°C for the POM, POM/alumina composite,

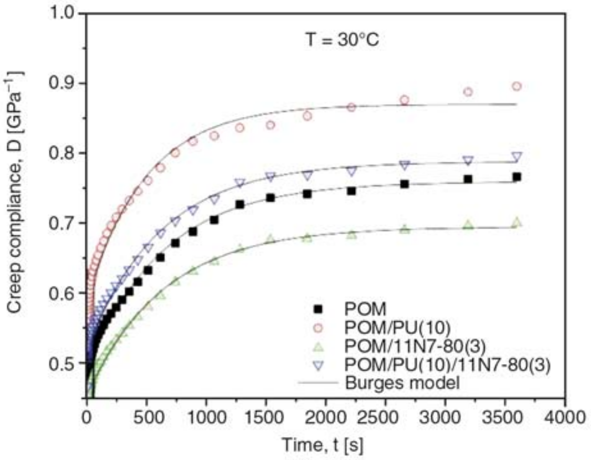

Figure 7. Tensile creep of POM, POM/PU blend, POM/alumina- and POM/PU/alumina composites at $T = 30$°C (6 MPa stress applied for $t = 60$ min). Experimental data were fitted by the Burgers model (see solid lines).

POM/PU blend and the alumina-containing ternary composites produced by WM-CT. The incorporation of alumina particles into POM matrix resulted in a considerable decrease of the creep compliance, as expected owing to their reinforcing effect. Conversely, the addition of PU increased the creep of POM. The compliance values were reduced by approx. 12% compared to the POM/PU blend when alumina was additionally incorporated. This creep response suggests again that alumina particles may be dispersed also in the POM matrix. This was supported by the SEM inspection (cf. Figure 5b). Parameters of the Burgers model were determined for each curve using the related software package of the DMTA device (Rheology Advantage Data Analysis) and listed in Table 2. The Burgers model consists of Maxwell and Voigt-Kelvin units connected in series. This phenomenological model was used to evaluate the effect of rubber and/or alumina particles on the instantaneous (D_0) and equilibrium $\Psi(t)$ parts (that was approximated by six Voigt-Kelvin elements) of the creep compliance ($D(t)$) determined by the Equations (1) and (2) [16]:

$$D(t)=D_0+\Psi(t)+\frac{t}{\mu_0} \tag{1}$$

$$\Psi(t)=\sum_{k=1}^{N} D_k\cdot\left(1-e^{\frac{-t}{\tau_k}}\right) \tag{2}$$

where t is the time, D_0 is the instantaneous compliance, $\Psi(t)$ is equilibrium compliance part of creep compliance, μ_0 is the viscosity and τ_k denotes the retardation time of the Voigt-Kelvin unit D_k.

The highest instantaneous compliance (D_0) was observed when PU was added into the POM. As shown in Table 2, one can see that the instantaneous compliance of the POM/alumina composite is lower than those of the POM and POM/PU blend. The enhancement in the instantaneous part of compliance is caused by the alumina particles and their dispersed state. This resulted in a decrease in the mobility of the amorphous segments.

Figures 8a–8d, demonstrate the effects of increased temperature on the creep response of POM, POM/PU blend, POM/alumina binary- and POM/PU/alumina ternary composites. The creep of all POM systems is sensitive to the temperature. A more interesting observation is the relative change in the transient creep with respect to instantaneous creep as the temperature increases. Unlike to pure POM,

Table 2. Burgers parameters for the creep response of the POM-based systems studied

Temperature	Parameter	POM	POM/PU(10)	POM/11N7-80(3)	POM/PU(10)/11N7-80(3)
30°C	D_0 [Pa^{-1}]	$3.63\cdot10^{-10}$	$3.77\cdot10^{-10}$	$2.58\cdot10^{-10}$	$1.39\cdot10^{-11}$
	D_{k1} [Pa^{-1}]	$2.22\cdot10^{-10}$	$2.15\cdot10^{-10}$	$2.26\cdot10^{-10}$	$2.39\cdot10^{-10}$
	τ_1 [s]	626	451.6	690.3	615.6
	D_{k2} [Pa^{-1}]	$4.01\cdot10^{-11}$	$5.92\cdot10^{-11}$	$5.66\cdot10^{-11}$	$7.41\cdot10^{-11}$
	τ_2 [s]	24.38	17.83	9.52	7.34
	D_{k3} [Pa^{-1}]	$7.61\cdot10^{-12}$	$4.24\cdot10^{-12}$	$1.09\cdot10^{-11}$	$3.72\cdot10^{-10}$
	τ_3 [s]	0.15	4.19	0.22	0.04
	D_{k4} [Pa^{-1}]	$1.29\cdot10^{-15}$	$2.52\cdot10^{-15}$	$2.09\cdot10^{-11}$	$2.56\cdot10^{-15}$
	τ_4 [s]	0.51	5.31	6.33	0.15
	D_{k5} [Pa^{-1}]	$8.63\cdot10^{-11}$	$1.41\cdot10^{-10}$	$3.16\cdot10^{-11}$	$6.98\cdot10^{-11}$
	τ_5 [s]	1.77	1.47	0.07	0.02
	D_{k6} [Pa^{-1}]	$9.09\cdot10^{-12}$	$2.89\cdot10^{-11}$	$8.53\cdot10^{-11}$	$5.42\cdot10^{-15}$
	τ_6 [s]	0.11	0.32	0.28	0.005
	μ_0 [Pa·s]	$8.25\cdot10^{13}$	$5.41\cdot10^{13}$	$3.68\cdot10^{14}$	$1.38\cdot10^{14}$

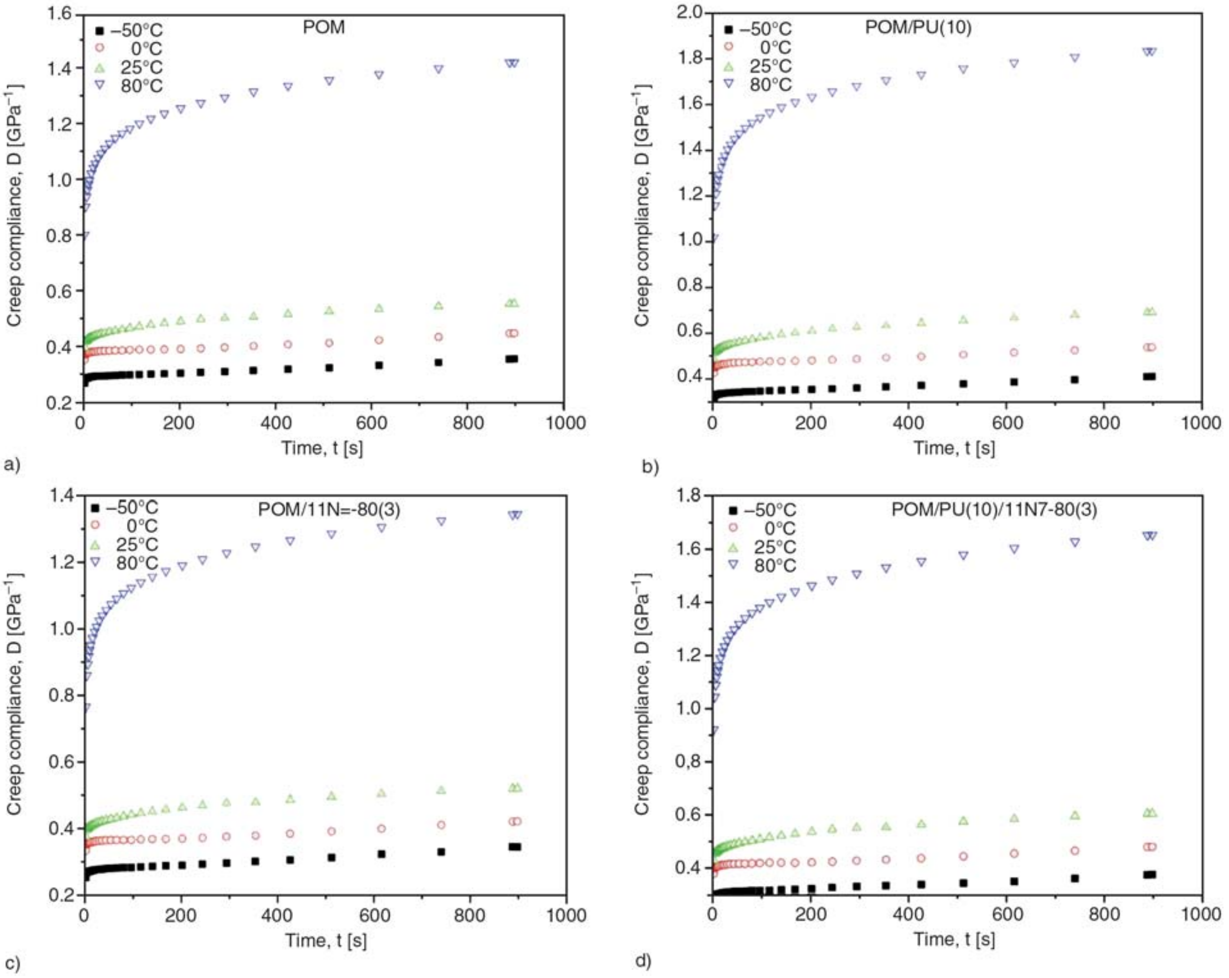

Figure 8. Effect of temperature on the tensile creep of POM (a), POM/PU blend (b) POM/alumina binary composite (c) and POM/PU/alumina ternary composite (d)

the incorporation of 3 wt% alumina particles reduced the creep compliance significantly, even at elevated temperatures. The creep data, measured in function of both time and temperature (T = –50… 80°C), have been considered to create creep master curves by adopting the time-temperature superposition (TTS) principle. The creep at other temperatures as measured can be estimated by considering the shift factor (a_T) along the time scale (t) (Equation (3)) :

$$D(t,T_1)=\frac{D(t,T_2)}{a_T} \tag{3}$$

The shift factors can be also correlated with temperature using the Williams-Landel-Ferry (WLF) (Equation (4)) [17]:

$$\log(a_T)=\frac{-C_1\cdot(T-T_0)}{C_2+(T-T_0)} \tag{4}$$

where C_1 and C_2 are constants and T_0 is the reference temperature (T_0 = 30°C).

Note that the above description has been employed for many polymeric materials to fit the creep compliance vs. time curves. Figure 9 displays the

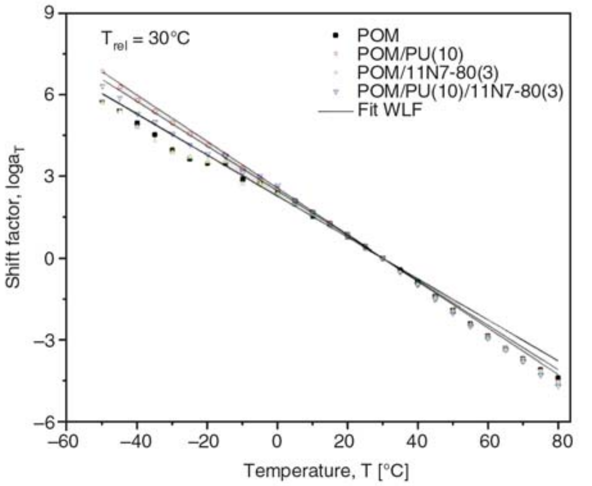

Figure 9. Experimental shift factors of the systems studied along with the related WLF fits

course of the experimentally determined a_T values as a function of the temperature. Master curves were created by using the above mentioned software package of the DMTA device. It has to be mentioned that this software allows only horizontal shifting of the creep curves along the time axis. A reference temperature (T_0 = 30°C) was used for the superposition process.

An empirical description for the creep compliance vs. time is given by Findley power law (Equation (5)) [18]:

$$D_F = D_{F0} + D_{F1} \cdot t^n \tag{5}$$

where n is a constant independent of stress, D_{F0} is the time-independent compliance, and D_{F1} is the coefficient of the time-dependent term.

Figure 10 shows the constructed master curves along with their Findley fits. The parameters of the Findley power law are listed in Table 3. Incorporation of alumina particles decreased the creep. This was expected based on the reinforcing effect of the nanoscale disperse alumina. By contrast, rubber particles markedly increased the creep. The POM systems experienced prominent creep by the incorporation of PU for both in POM/PU blend and POM/PU/alumina ternary composite. Figure 10 also shows that the power law model fits very well to the creep data for all system up to 3000 hours or at least until a given threshold. Similar results were reported for a polyamide 6.6 composite containing TiO_2 nanoparticles [19]. The authors observed that the power law is in good agreement with the experimental results until a given time, while for longer time duration the calculated data may show considerable deviation from the experimental results. It should be noted that the master curves constructed from short-term creep data at high temperature may not follow the expected creep behavior. This is mostly due to the increasing mobility of the polymer chains.

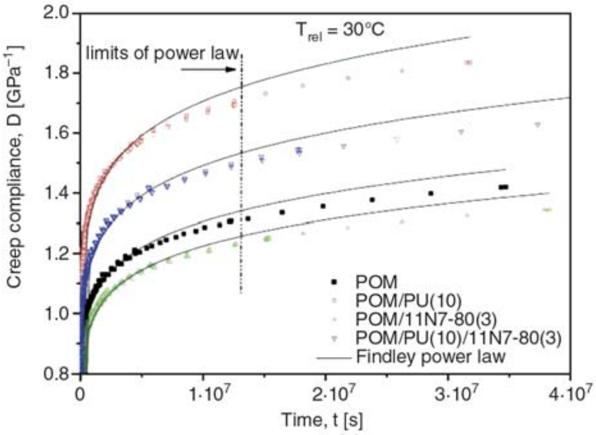

Figure 10. Creep master curves (creep compliance vs. time) constructed by considering $T_{ref.}$ = 30°C for the POM based systems. Note: continuous line represents the Findley fit.

Table 3. Findley parameters for the creep master curves of the POM-based systems studied

Sample designation	D_{F0} [GPa^{-1}]	D_{F1} [$GPa^{-1} \cdot s^{1/n}$]	n
POM	0.26	0.14	0.122
POM/PU(10)	0.32	0.19	0.124
POM/11N7-80(3)	0.25	0.13	0.123
POM/PU(10)/11N7-80(3)	0.28	0.17	0.124

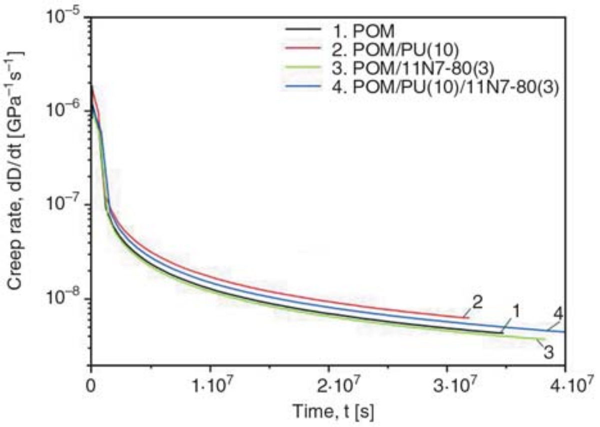

Figure 11. Creep rate as a function of time at T = 30°C for the POM systems studied

A creep rate can be quantified as the time derivative (dD/dt) of the creep compliance vs. time curves. Figure 11 displays the effect of alumina on the creep rate of POM and POM/PU blend. Note that the creep rate decreases with increasing time and marginally also with the addition of alumina particles. It is also clear from this figure that the presence of rubber particles increase the creep rate of POM matrix.

3.4. Tensile tests

Results of the tensile mechanical tests are given in Figure 12. The tensile mechanical and impact data are listed in Table 4. It is clearly seen that the incorporation of alumina and PU particles strongly affected the mechanical behavior of POM. Adding alumina increased the stiffness, slightly reduced the tensile strength, and prominently the elongation at break. Conversely, the ductility of the POM/PU blend increased and the stiffness and strength

Table 4. Tensile mechanical and impact characteristics of the neat POM, POM/PU blend, POM/alumina binary and POM/PU/alumina ternary composites prepared by WM-CT

Sample designation	Tensile strength [MPa]	Tensile modulus [MPa]	Elongation at break [%]	Notched Charpy impact energy [kJ/m²]
POM	63 ± 0.2	2646 ± 71	17.8 ± 2.8	13.5 ± 1.1
POM/PU(10)	55 ± 0.2	2392 ± 101	31.9 ± 4.5	16.3 ± 1.3
POM/11N7-80(3)	61 ± 0.1	2847 ± 143	9.1 ± 2.8	9.8 ± 1.5
POM/PU(10)/11N7-80(3)	47 ± 0.5	2323 ± 62	57.1 ± 8.0	15.6 ± 1.1

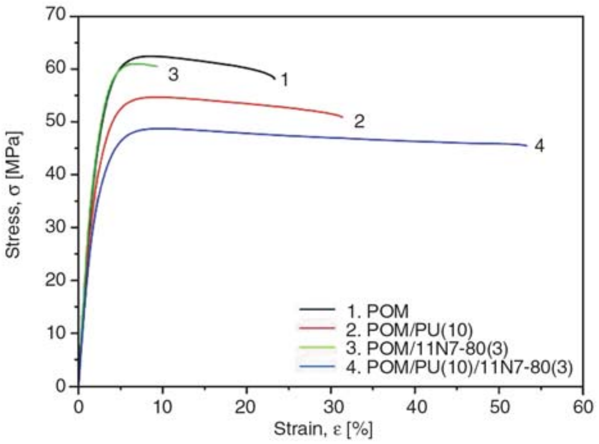

Figure 12. Characteristic tensile stress-strain curves for the POM systems studied

decreased compared to the neat POM. The reduction in the tensile strength may be attributed to the presence of rubber particles acting as stress concentrators and forcing the yielding of POM at lower stresses. The decrease in the tensile modulus in the POM/PU blend may be accounted for the softening effect of PU, since the tensile modulus of rubber is considerably lower than that of the neat POM. The POM/PU/alumina ternary composites exhibited significant decrease in modulus accompanied by much higher elongation at break as compared to the POM, POM/alumina composite and POM/PU blend.

3.5. Impact properties

Although the tensile modulus of POM is increased by the incorporation of alumina particles, the toughness was reduced. However, POM modified with 10 wt% PU exhibited not only higher elongation at break, but simultaneously also higher impact energy (~22%) compared to the neat POM (cf. Table 4). This is due to the submicron dispersion of the rubber particles. Accordingly, the incorporation of rubbery particles in a suitable size range increases the impact resistance of POM, as expected. Furthermore, the impact energy of POM/PU/alumina ternary composites decreased marginally compared to the POM/PU blend but remained still higher than that of POM.

4. Conclusions

Toughened or nanofilled POM composites have been successfully produced by WM-CT. SEM and TEM results have shown that the alumina and rubber dispersions became fine and homogeneous when using the water-mediated extrusion melt compounding. The mechanical properties (stiffness and creep resistance) of the binary POM/alumina and ternary POM/PU/alumina composites were superior to those of the POM and POM/PU blend, respectively. The impact resistance of POM was highly enhanced by the addition of PU rubber, dispersed in submicron range. The size of the dispersed PU agreed fairly with that of the initial PU latex. Incorporation of PU into POM increased the creep compliance, whereas additional modification with boehmite alumina yielded a reverse effect. The creep resistance of the binary POM/alumina composite was higher than the neat POM. Creep master curves in form of compliance vs. time, constructed by considering short-term creep data, could be well described by the Findley power law model, at least until a given threshold value. The proposed water-mediated extrusion melt compounding is a very effective process being simple and cost efficient for producing thermoplastic nanocomposite with and without additional toughening. A further benefit of this method is that the expensive chemical modification of the nanofillers can be avoided.

Acknowledgements

S. Siengchin thanks the DFG (German Research Foundation) for the fellowship in the framework of the graduate school GRK 814. POM and alumina were kindly provided by Dr. N. Papke (Ticona, Frankfurt, Germany) and Dr. O. Torno (Sasol, Hamburg, Germany), respectively.

References

[1] Karger-Kocsis J., Zhang Z.: Carbon nanotube and carbon nanofiber-reinforced polymer composites. in 'Mechanical Properties of Polymers Based on Nanostructure and Morphology' (eds.: Michler G. H., Baltá-Calleja F. J.) CRC Press, Boca Raton, 553–602 (2005).

[2] Park E. J., Heo H., Lim K. T.: Synthesis and characterization of $Al(OH)_3$/polystyrene nanocomposite latex particles by emulsion polymerization. Macromolecular Symposia, **249–250**, 247–250 (2007).

[3] Jia Q-X., Wu Y-P., Xu Y-L., Mao H-H., Zhang L-Q.: Combining in-situ organic modification of montmorillonite and the latex compounding method to prepare high-performance rubber-montmorillonite nanocomposites. Macromolecular Materials and Engineering, **291**, 218–226 (2006).

[4] Miltner H. E., Grossiord N., Lu K., Loos J., Koning C. E., Van Melle B.: Isotactic polypropylene/carbon nanotube composites prepared by latex technology. Thermal analysis of carbon nanotube-induced nucleation. Macromolecules, **41**, 5753–5762 (2008).

[5] Grunlan J. C., Mehrabi A. R., Bannon M. V., Bahr J. L.: Water-based single-walled-nanotube-filled polymer composite with an exceptionally low percolation threshold. Advanced Materials, **16**, 150–153 (2004).

[6] Grunlan J. C., Kim Y-S., Ziaee S., Wei X., Abdel-Magid B., Tao K.: Thermal and mechanical behavior of carbon nanotube-filled latex. Macromolecular Materials and Engineering, **291**, 1035-1043 (2006).

[7] Karger-Kocsis J.: Water-mediated dispersion of 'nanofillers' in thermoplastics: Is it the right way? Express Polymer Letters, **2**, 312 (2008).

[8] Kato M., Matsushita M., Fukumori K.: Development of a new production method for a polypropylene-clay nanocomposites. Polymer Engineering and Science, **44**, 1205–1211 (2004).

[9] Soulestin J., Quiévy N., Sclavons M., Devaux J.: Polyolefins-biofibre composites: A new way for an industrial production. Polymer Engineering and Science, **47**, 467–476 (2007).

[10] Siengchin S., Karger-Kocsis J., Thomann R.: Alumina-filled polystyrene micro- and nanocomposites prepared by melt mixing with and without latex precompounding: Structure and properties. Journal of Applied Polymer Science, **105**, 2963–2972 (2007).

[11] Siengchin S., Karger-Kocsis J., Apostolov A., Thomann R.: Polystyrene-fluorohectorite nanocomposites prepared by melt mixing with and without latex precompounding: Structure and mechanical properties. Journal of Applied Polymer Science, **106**, 248–254 (2007).

[12] Mehrabzadeh M., Rezaie D.: Impact modification of polyacetal by thermoplastic elastomer polyurethane. Journal of Applied Polymer Science, **84**, 2573–2582 (2002).

[13] Gao X., Qu C., Fu Q.: Toughening mechanism in polyoxymethylene/thermoplastic polyurethane blends. Polymer International, **53**, 1666–1671 (2004).

[14] Streller R. C., Thomann R., Torno O., Mülhaupt R.: Isotactic poly(propylene) nanocomposites based upon boehmite nanofillers. Macromolecular Materials and Engineering, **293**, 218–227 (2008).

[15] Siengchin S., Karger-Kocsis J., Psarras G. C., Thomann R.: Polyoxymethylene/polyurethane/alumina ternary composites: Structure, mechanical, thermal and dielectric properties. Journal of Applied Polymer Science, **110**, 1613–1623 (2008).

[16] Kaschta J., Schwarzl F. R.: Calculation of discrete retardation spectra from creep data-I. Method. Rheologica Acta, **33**, 517–529 (1994).

[17] Ferry J. D.: Viscoelastic properties of polymers. Wiley, New York (1980).

[18] Findley W. N., Lai J. S., Onaran K.: Creep and relaxation of nonlinear viscoelastic materials. Dover Publications, New York (1989).

[19] Starkova O., Yang J., Zhang Z.: Application of time-stress superstition to nonlinear creep of polyamide 66 filled with nanoparticles of various sizes. Composites Science and Technology, **67**, 2691–2698 (2007).